



Research on Engineering Structures & Materials

Volume 6 Issue 4 December 2020 P-ISSN: 2148-9807 E-ISSN: 2149-4088

J

R

E

S

M

www.jresm.org



Research Group

The International Journal of **Research on Engineering Structures and Materials (RESM)** is a peer-reviewed open access journal (p-ISSN: 2148-9807; o-ISSN: 2149-4088) published by MIM Research Group. It is published in February, June, September, and December.

The main objective of RESM is to provide an International academic platform for researchers to share scientific results related to all aspects of mechanical, civil and material engineering areas.

RESM aims the publication of original research articles, reviews, short communications technical reports, and letters to the editor on the latest developments in the related fields.

All expenditures for the publication of the manuscripts are most kindly reimbursed by *MIM Research Group*. Thus, authors do not need to pay for publishing their studies in the journal.

The scope of the journal covers (but not limited to) behavior of structures, machines and mechanical systems, vibration, impact loadings and structural dynamics, mechanics of materials (elasticity, plasticity, fracture mechanics), material science (structure and properties of concrete, metals, ceramics, composites, plastics, wood, etc.), nano-materials performances of new and existing buildings and other structural systems, design of buildings and other structural systems, seismic behavior of buildings and other structural systems, repair and strengthening of structural systems, case studies and failure of structural systems, safety and reliability in structural and material engineering, use of new and innovative materials and techniques in energy systems and mechanical aspects of biological systems (biomechanics and biomimetics).

The topics covered in RESM include:

- Structural Engineering
- Mechanical Engineering
- Material Engineering
- Earthquake Engineering
- Nano-technology
- Energy Systems
- Biomechanics and Biomimetics

Abstracting and Indexing

Please visit <http://www.jresm.org> for more information.

Graphics and Design

H. Ersen Balcioglu

ersen.balcioglu@usak.edu.tr

Yunus Demirtas

yunus.demirtas@usak.edu.tr



**RESEARCH on
ENGINEERING STRUCTURES &
MATERIALS**



Published by MIM Research Group

RESEARCH on ENGINEERING STRUCTURES & MATERIALS

Editorial Board

Editor in Chief		
Hayri Baytan Özmen	Usak University	Turkey

Editor (Energy, Thermodynamics)		
Canan Kandilli	Usak University	Turkey

Editor (Mechanics, Materials)		
H. Ersen Balcioğlu	Usak University	Turkey

Editor (Earthquake Eng., Structural Eng.)		
Michele Barbato	University of California Davis	USA

Editor (Mechanics, Biosystems, Meta-materials)		
Alp Karakoç	Aalto University	Finland

Editor (Applied Mechanics, Manufacturing, Design)		
Faris Tarlochan	Qatar University	Qatar

Editorial Office

Publishing Manager & Copyeditor		
H. Ersen Balcioğlu	Usak University	Turkey

Publishing Assistant		
Yunus Demirtaş	Usak University	Turkey

Editorial Board Members

Farid Abed-Meraim	Arts et Metiers ParisTech	France
P. Anbazhagan	Indian Institute of Science	India
Raffaele Barretta	University of Naples Federico II	Italy
R.S. Beniwal	Council of Scientific and Industrial Research	India
Antonio Caggiano	University of Buenos Aires	Argentina
Noel Challamel	University of South Brittany	France
Abdulkadir Çevik	Gaziantep University	Turkey
J. Paulo Davim	University of Aveiro	Portugal
Hom Nath Dhakal	University of Portsmouth	UK
S. Amir M. Ghannadpour	Shahid Beheshti University	Iran
Ali Goodarzi	Harvard University	USA
Jian Jiang	National Institute of Standards and Technology	USA
Ramazan Karakuzu	Dokuz Eylül University	Turkey
Arkadiusz Kwiecien	Cracow University of Technology	Poland
Stefano Lenci	Universita Politecnica delle Marche	Italy
Yuan Meini	North University of China	China
Stergios A. Mitoulis	University of Surrey	UK
Alaa M. Rashad	Shaqra University	Saudi Arabia
Mohammad Mehdi Rashidi	University of Tongji	China
Pier Paolo Rossi	University of Catania	Italy
Neritan Shkodrani	Polythecnic University of Tirana	Albania
Faris Tarlochan	Qatar University	Qatar
Y.B. Yang	National Taiwan University	Taiwan

Advisory Board Members

Yinusa Amoo Ahmed	University of Lagos	Nigeria
Erkin Akdoğan	Karamanoğlu Mehmetbey University	Turkey
Mustafa Akpolat	Munzur University	Turkey
Sevim Alışır	Ondokuz Mayıs University	Turkey
Saber Alizadeh	Bu-Ali-Sina University	Iran
Danar Altalabani	University of Applied Sciences Karlsruhe	Germany
Mustafa Yasin Aslan	Usak University	Turkey
Huseyin Ersen Balcioglu	Usak University	Turkey
Beyhan Bayhan	Bursa Technical University	Turkey
Emin Bayraktar	Supméca Institute of Mechanics of Paris	France
Mehmet Bulut	Hakkari University	Turkey
Hektor Cullufi	Polytechnic University of Tirana	Albania
Preeta Datta	North Carolina State University	USA
J. Paulo Davim	University of Aveiro	Portugal
Hakan Demir	Iskenderun Technic University	Turkey
Cengiz Görkem Dengiz	Ondokuz Mayıs University	Turkey
Akar Dogan	Munzur University	Turkey
Hany El-Hamshary	Tanta University	Egypt
Engin Emsen	Akdeniz University	Turkey
H. Murat Enginsoy	Usak University	Turkey
Ali Faghidian	Islamic Azad University	Iran
Mohamed Guenfoud	University Larbi Tébéssi	Algeria
Mükrimin Şevket Güney	Giresun University	Turkey
Dulce Franco Henriques	Instituto Politécnico de Lisboa	Portugal
Halit Levent Hosgun	Bursa Technical University	Turkey
Mahdi Hosseini	Jawaharlal Nehru Technological University	India

Advisory Board Members

Ercan Isik	Bitlis Eren University	Turkey
Zafer Kaya	Dumlupınar University	Turkey
Ali Koçak	Yildiz Technical University	Turkey
Sedat Kömürcü	İstanbul Technical University	Turkey
Güven Kurtuldu	ETH Zurich	Switzerland
Charles Langston	University of Memphis	USA
Ahmet Meram	KTO Karatay University	Turkey
Süha Orçun Mert	İskenderun Technical University	Turkey
Masoomah Mirrashid	Semnan University	Iran
Jinxu Mo	Yangtze University	China
Kim Hung Mo	University of Malaya	Malaysia
Arunima Nayak	Graphic Era University	India
Mehmet Palanci	Istanbul Arel University	Turkey
Amin Moslami Petrucci	University Amirkabir	Iran
Majid Pouraminian	Islamic Azad University	Iran
Alaa M. Rashad	Building Materials Research and Quality Control Institute	Egypt
Fabio Rizzo	University of Chieti-Pescara	Italy
Behnam Rosti	Shiraz University of Technology	Iran
Tamer Saracyakupoglu	Istanbul Gelisim University	Turkey
Rudimylla Septimio Azeredo	Federal University of Southern and Southeastern Pará	Brazil
Neritan Shkodrani	Polytechnic University of Tirana	Albania
Ramachandran Seshadri	Stony Brook University	USA
Adnan Sozen	Gazi University	Turkey
Brijesh Singh	National Council for Cement & Building Material	India
Hossein Taghipoor	Semnan University	Iran

Advisory Board Members

Anand B. Tapase	Karmaveer Bhaurao Patil College of Engineering	India
Faris Tarlochan	Qatar University	Qatar
Hamide Tekeli	Süleyman Demirel University	Turkey
Dilay Uncu	Manisa Celal Bayar University	Turkey
Abid Ustaoglu	Bartın University	Turkey
Ümit Ünver	Yalova University	Turkey
Gustavo Bosel Wally	Federal University of Rio Grande do Sul	Brazil
Jhair Yacila	Pontificia Universidad Católica del Perú	Peru
Onder Yesil	Usak University	Turkey
Salih Hakan Yetgin	Dumlupınar University	Turkey
Ferhat Yıldırım	Çanakkale Onsekiz Mart University	Turkey
Recep Yurtseven	Pamukkale University	Turkey

In This Issue

Review Article

293 **Ahmet Meram, Betül Sözen**

Investigation on the manufacturing variants influential on the strength of 3D printed products

Research Article

315 **Halil Murat Enginsoy**

Investigation of recycled aluminum matrix composites reinforced with copper and γ -alumina manufactured by sinter and sinter + forging methods

Review Article

327 **Aykut Elmas, Güliz Akyüz, Ayhan Bergal, Müberra Andaç, Ömer Andaç**

Mathematical Modelling of Drug Release

Research Article

351 **M. Govindaraju, M. Selvaraj**

Boundary layer flow of gold –thorium water based nanofluids over a moving semi-infinite plat

Research Article

363 **Canan Kandilli, Mert Uzel**

Evaluation of annual performance of a photovoltaic thermal system integrated with natural zeolites

Research Article

375 **Büşranur Duman, Berker Fıçıcılar**

Acid modified graphite felt cathode electrode for low temperature H_2/Br_2 redox flow battery

Research Article

385 **Abdullah Fettahoglu, Mehmet Cemal Genes**

Design charts for linear elastic pavements

Research Article

411 **Elton Hala**

Wind performance for a stadium geometry

Research Article

425 **Marjo Hysenliu, Altin Bidaj, Huseyin Bilgin**

Influence of material properties on the seismic response of masonry buildings

Free access to tables of content, abstracts and full text of papers for web visitors.

Copyright © 2020

Research on Engineering Structures & Materials

MIM Research Group Publications

P-ISSN: 2148-9807

E-ISSN: 2149-4088

<http://www.iresm.org>



ABSTRACTING / INDEXING

The international journal of Research on Engineering Structures and Materials (RESM) is currently Abstracted/Indexed by Asos Indeks, CiteFactor, Cosmos, CrossRef, Directory of Research Journal Indexing, Engineering Journals (ProQuest), EZB Electronic Journal Library, Global Impact Factor, Google Scholar, International Institute of Organized Research (I2OR), International Scientific Indexing (ISI), Materials Science & Engineering Database (ProQuest), Open Academic Journals Index, Publication Forum, Research Bible/Scientific Indexing Service, Root Indexing, Scopus, Ulakbim TR Index (Tubitak), Universal Impact Factor and under evaluation by many other respected indexes.

Check web site for current indexing info.

Scopus®



Publication
Forum



Review Article

Investigation on the manufacturing variants influential on the strength of 3D printed products

Ahmet Meram^{1,a,*}, Betül Sözen^{2,b}

¹ Department of Mechatronics Engineering, KTO Karatay University, Konya/Turkey

² Department of Mechanical Engineering, Selçuk University, Akşehir/Konya, Turkey

Article Info

Article history:

Received 31 Dec 2019

Revised 13 Mar 2020

Accepted 8 Apr 2020

Keywords:

3D Printer;

Manufacturing

Variants;

Tensile Strength;

Additive Manufacturing

Abstract

This paper investigates the manufacturing variants influential on the strength of 3D printed products. In contrast to the traditional manufacturing methods which produce the final product via removing materials from parts, in 3D printing technology the products are provided with adding layer by layer directly from a digital file. 3D printing technology due to overcoming the many difficulties and limitations of conventional fabrication approaches is a rapidly progressing technology which takes attention in many industries such as aerospace, automotive, medical and building industries. This paper aims to research the variants affecting the mechanical properties of components produced by 3D printing technologies. To reach this aim a comprehensive review was conducted to determine the various process and geometric parameters in 3D printing technologies. The conducted literature survey results indicate that besides the filament material, the nozzle speed and diameter, layer thickness, filament diameter, printing raster angle, printing pattern, temperature and infill density are parameters which influence the final product quality and mechanical properties in term of ultimate tensile strength, yield stress and elasticity modulus. It is concluded that 3D printing filament materials strength has direct affect on the strength of final product. By providing the adequate thermal behavior of the system, the cohesion between layers can be improved. Extrusion speed affects surface roughness and quality of the produced components. Nozzle diameter has a significant influence on interlayer cohesion. The honeycomb pattern due to facilitating the load transfer between layers provides higher mechanical strength. Findings of this study will guide the researchers and manufacturers to select appropriate printing parameters to produce component with optimum mechanical properties.

© 2020 MIM Research Group. All rights reserved.

1. Introduction

Additive manufacturing (AM), commonly known as 3D printing or rapid manufacturing (RM) [1] is a rapidly progressing technology in recent years. AM is different from traditional or subtractive manufacturing. The product is provided with adding layers until the last layer is completed while in traditional manufacturing desired product can be obtained via removing materials from parts [2-5]. 3D printing technology due to overcoming the many difficulties and limitations of conventional fabrication approaches takes attention in many industries such as aerospace, automotive, medical, building industries, fashion and fashion accessories [6-8]. This technology allows fabricating complex structures in a controllable manner with desired architecture and porosity, enables designers and engineers to create unique products that can be manufactured at

*Corresponding author: ahmet.meram@karatay.edu.tr

^a orcid.org/0000-0002-8440-8462; ^b orcid.org/0000-0002-7011-0948

DOI: <http://dx.doi.org/10.17515/resm2019.171me3112>

Res. Eng. Struct. Mat. Vol. 6 Iss. 4 (2020) 293-313

low volumes in an economical way [9-11] and provides advantages such as less waste, freedom of design and automation, saving of material and energy, environmental/ecological advantages [12-15]. For instance, CFM International's LEAP aircraft engine can be given an example as the first step of the additive manufacturing journey in the aviation industry [16-18].

For the first time, this engine features an additively manufactured fuel nozzle. This part used to be made up of 20 different parts. Thanks to additive manufacturing, it is now manufactured in one single piece [19-20]. In the aviation industry, materials are manufactured with highly engineered techniques, therefore these materials are generally expensive. For example, in 1 LEAP engine, there are 19 nozzles. Thanks to AM, lighter parts with lower cost and lower operational time can be produced. So via additive manufacturing, cost effectiveness in manufacturing can be provided [21].



Fig. 1 3D-printed fuel nozzle for the LEAP engine [7]

Due to the evolution of traditional manufacturing technologies, nowadays, small scale 3D printing devices can be found in local production workshops. The additive manufacturing method is performed through various technologies, which each one requires a special 3D printing device. The most open source 3D printers are operating based on the fused deposition modeling (FDM) technology [22-25]. The 3D printing device that use FDM technology build objects layer by layer from the very bottom up by heating and extruding thermoplastic filament. Firstly, special software “cuts” CAD model into layers and calculates the way printer’s extruder would build each layer. Along to thermoplastic a printer can extrude support materials as well. Then the printer heats thermoplastic till its melting point and extrudes it throughout nozzle onto base, which can also be called a build platform or a table, along the calculated path [26-28]. A computer of the 3d printer translates the dimensions of an object into X, Y and Z coordinates and controls that the nozzle and the base follow calculated path during printing. To support upper layer the printer may place underneath special material that can be dissolved after printing is completed [29-30]. The most common of those are acrylonitrile butadiene styrene (ABS) and poly(lactic acid)(PLA) filaments. The FDM is widely useful to produce end-use products, particularly small, detailed parts and specialized manufacturing tools [31].

The main component of a FDM machine are: extrusion head, building platform and material spool (or filament). The main parts of extrusion head are: drive wheels, heating element and extrusion nozzle. Usually, the FDM extrusion head is operating in the x-y plane, while the building platform moves down in the z-plane to accommodate the deposit layers until the whole 3D part is finished [32]. In this technology as shown in Fig. 2 the raw material in the filament form feed the printing device by a mechanical mechanism and the

raw material heated up to the to 1°C above its melting point, so it solidifies right after extrusion and then welds to previous layers. The desired component is fabricated by adding a raw material layer by layer in 3D printing device from three-dimensional model data. Recent FDM system heads include two nozzles; one for the part material and one for the support material. Between different additive manufacturing methods, FDM has an advantage over the others as the use of material in filament form offers flexibility and reduces the resident time in the melting chamber. In general, the FDM process is quite simple since the filament will push by the roller to the melting chamber. Print quality and sensitivity have increased with the development of 3D printing technologies. In AM technologies, environmental factors such as temperature, internal flow, and structural factors such as vibration response are critical parameters that affect as physical and thermal effects on printing hardware [32-35].

To fabricate a product using FDM technology, it is required to define a certain number of printing parameters. Since the mechanical performance and geometrical accuracy of the final product are highly affected by these parameters, the researchers conducted studies to determine the influential parameters. Kim et al. [36] experimentally investigated the effect of infill rate, orientation angle, and type of materials on the mechanical properties of specimens made ABS and PLA. Kuznetsov et al. [37] by conducting experimental tests concluded that in addition to the strength of the filament material, the strength and stability of the bonds between the layers of the specimens are highly influenced by the printing parameters. Sagias et al. [38] proposed a new approach to evaluate how the printing parameters affect the mechanical properties of the printed part to obtain a product with improved mechanical properties. The reasonable choice of printing parameters on 3D printers results in products with high strength and quality [39].

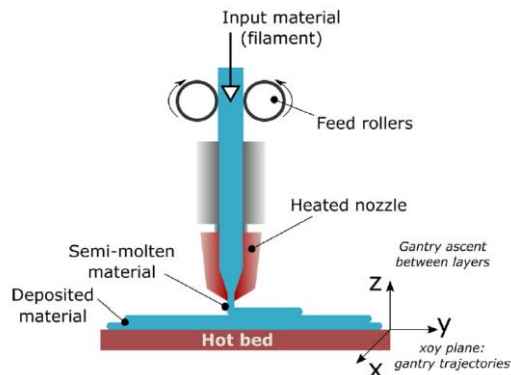


Fig.2 Schematic representation of a fused deposition modeling system [30]

The strength of the products fabricated by the 3D print device is lower than the ones made of the same polymer by injection molding [40]. Since the printing parameters are defined before producing the physical models, by understanding the role of each parameter, the mechanical performance of the final product can be improved. Motivated by this fact, this paper aims to research the parameters affecting the mechanical properties of components produced by 3D printing technologies. To reach this aim a comprehensive review was conducted to determine the various process and geometric parameters in 3D printing technologies. The conducted literature survey results indicate that besides the filament material, the nozzle speed and diameter, layer thickness, filament diameter, printing raster angle, printing pattern, temperature and infill density are parameters which influence the final product quality and mechanical properties in terms of tensile strength, yield stress

and elasticity modulus. In addition to these parameters, road width and air gap also play a significant role in mechanical performance of FDM parts.

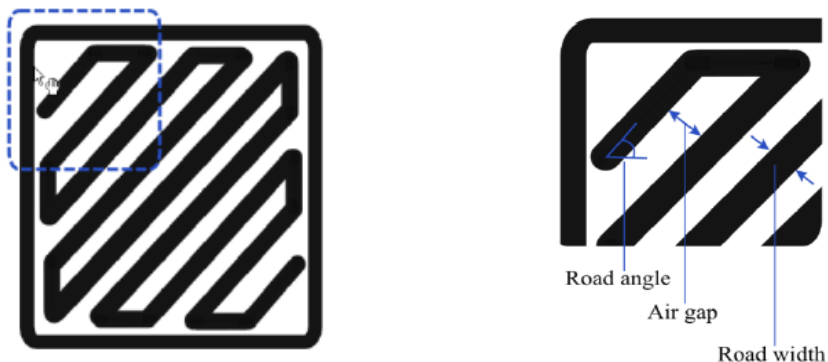


Fig. 3 Representation of the main process parameters [29]

2. 3D printer manufacturing variants

2.1. 3D Printing Filament Materials

The filament material is one of the major parameters for determining the mechanical properties of final product. Metals, polymers, ceramics, concrete and composites are currently used in 3D printing. A wide range of polymeric materials given in Table 1 are used in 3D printers. Despite this variety, ABS and PLA are the main polymers used in the majority of applications. The main advantages of PLA to other polymers used in 3D printers are the low level of shrinkage and relatively low melting temperature. The products made of PLA due to less internal stresses have better mechanical characteristics. Tymrak et al. [39] experimentally measured the mean tensile strength values of 56.6MPa and 28.5 MPa and mean elasticity modulus of 3.37 GPa and 1.81 GPa in specimens made of PLA and ABS, respectively. The mechanical properties of some common polymeric filament material for 3D printing given by the manufacturers are shown in Table 1. Generally, the specifications listed in Table 1 are higher than the measured values [41]. One of the main reasons of this mismatch can be explained by unparalleled testing force vector with the filament printed direction. Advanced metals are used in the aerospace and automotive industries. The ceramics and concrete are mainly employed in the manufacturing of scaffolds and building by 3D printing technology, respectively.

Table 1. Material abbreviations and specifications as provided by the manufacturers [41]

Abbreviation	Full Name	Young's Modulus [GPa]	Yield Stress [MPa]	Strain at Break [%]
PLA	Poly lactide	3.5	60	-
ABS	Acrylnitril-Butadien-Styrol-Copolymer	2	44	-
PLA-H	Poly lactide-Holz	3.3	46	-
PET-C	Polyethylenterephthalat-Carbon	3.8	52.5	8
PET	Polyethylenterephthalat	3.8	50	20
PA-C	Polyamide-Carbon	2.15	100	-
PA	Polyamide (Nylon (r))	-	45.6	34

In addition to above-mentioned materials, carbon-fiber and glass-fiber reinforced composite filament materials are used in 3D printing devices. Justo et al. [42] experimentally tested specimens printed from the reinforced endless carbon-fiber reinforced filaments with a high ratio of carbon and measured the ultimate stress values of 700 MPa. In another reported study, the processability of glass fiber-reinforced ABS composites with three different glass fiber proportions was examined. The results proved that glass fiber could significantly advance the tensile strength and surface rigidity of the specimens made of ABS filament [43]. Also, the experimental investigation on the mechanical properties of thermoplastic matrix Carbon Fiber Reinforced Polymer (CFRP) composites Fused Deposition Modelling (FDM)-printed specimens proved that the carbon fiber with various ratio and length is effective in improving the mechanical properties of specimens [44]. So, besides various and geometric parameters which will be explained in detail in below, adding reinforcement material can be a method to improve mechanical properties of material which is produced using FDM technology.

2.2. Temperature

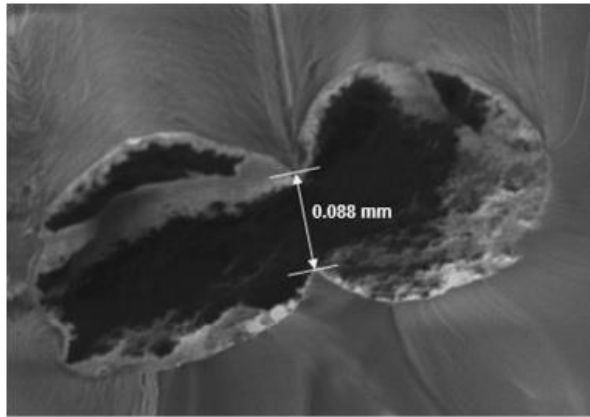
The extrusion temperature and bed temperature are parameters affecting the quality of finished product in 3D printing technologies due to changing the adhesion process between layers. The appropriate printing conditions in terms of temperature, depending on the used filament are provided by manufacturers.

Table 2. Thermal specification of PLA and ABS which is given by manufacturer [45]

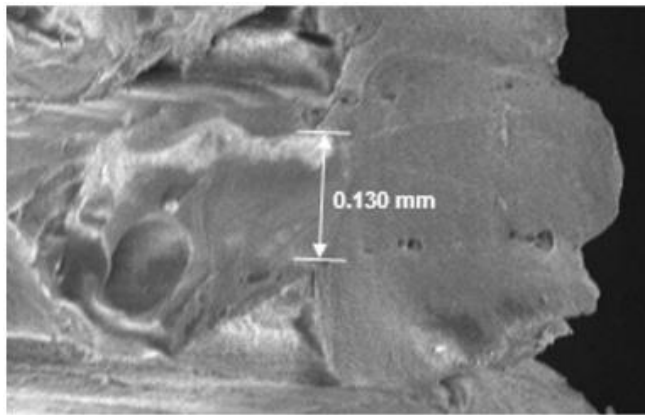
Thermal Properties	PLA	ABS
Melt Flow Index	10.3 cm ³ /10 min.	9.7 cm ³ /10 min.
Glass Transition Temperature	60-65°C	105°C
Slumping Temperature	70-80°C	110-125°C
Melting Temperature	160-190°C	210-240°C
Printing Temperature	190-220°C	230-250°C
Printbed Temperature	50-70°C	80-120°C

The type of printer is also determining in the optimum temperature of nozzle. The nozzle temperature affects the tensile strength of the specimen [46]. The experimental investigation conducted in [47] and [48] regarding extrusion temperature, proved as the temperature increases the bonding between layers improves. Fernandes et al [35] examined the mechanical properties of standard specimens made of PLA filaments in 200°C and 220°C extrusion temperatures. They obtained higher ultimate tensile stress, yield stress and elastic modulus in 220 °C in comparison to 200°C extrusion temperature. They explained that by increasing the temperature the material viscosity decreased and the circular section of extruded material became oval. So, the contact area between the layers extended. By providing the adequate thermal behavior of the system, the cohesion between layers can be improved. Therefore, the freshly extruded material is able to combine chemically to the already deposited material [49].

On the other hand, when relationship between fusion temperature and dimensional accuracy is analyzed, low temperature means minimum dimensional error. According to Demircioglu et al.'s study, samples which have same printing parameters were manufactured with five different extruder temperatures (185, 195, 205, 215 and 220°C). The results showed that the minimum dimensional error was obtained from the fusion temperature of 185°C with the value of 0.290797 mm and percentage of 3% and maximum dimensional error was obtained from the fusion temperature of 220°C with the value of 0.487134 mm and percentage of 4.8% [32].



(a)



(b)

Fig. 4 SEM images of the neck formed (a) at 245 °C extrusion temperature (b) at 260 °C extrusion temperature [50]

2.3. Extrusion Speed

Extrusion speed affects surface roughness and quality of the produced components with AM technique. In Demircioglu et. al.'s study, effect of extrusion speed and surface roughness and product quality were investigated. According to study, some printing parameters were selected like below:

Layer height was selected 200 microns for all samples. The heated bed temperature was selected as 60° to increase the bonding and surface quality. Extruder temperature was set to 195°C. The samples were produced with extrusion speeds of 20, 40 and 60 mm/s to determine the surface roughness and quality. During printing, temperature, infill density, heated bed temperature, number of shell and layer thickness was set to fixed values in order to observe the effect of extrusion speed on surface roughness. As a result of study, it is observed that increasing in extrusion speed causes increasing in surface roughness [32].

2.4. Nozzle

The nozzle which has controllable diameter and speed influences the quality of the printed part and the productivity of the process [51]. Generally, raw materials are produced in

1.75-mm and 3-mm diameter filaments, and nozzle diameters are varying from 0.1 to 1 mm [30].

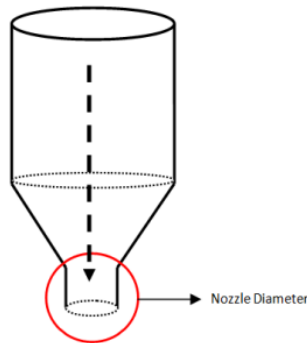


Fig. 5 Image of nozzle diameter [33]

Kuznetsov et al. 2018 [37] showed that an increase in the nozzle diameter not only reduces printing time, but also increases sample strength. Nozzle diameter has a significant influence on interlayer cohesion. Given constant layer height, printing with a larger nozzle resulted in increased strength. The advantages of larger nozzles became even more evident with greater layer thickness.

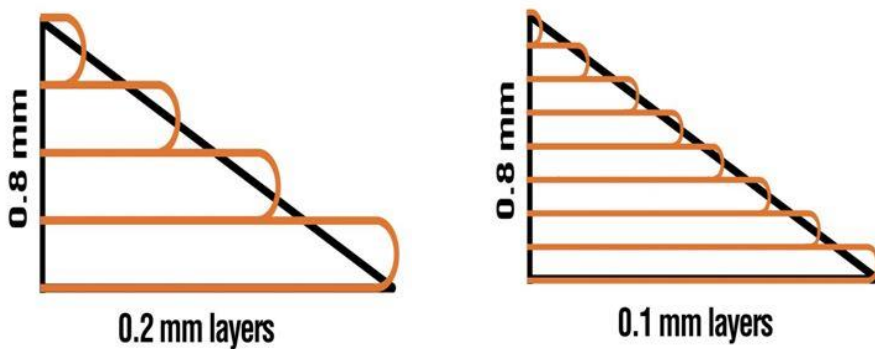


Fig. 6 Products which have different layer thickness can be printed by same nozzle diameter [52]

To determine effect of nozzle diameter, Sukındar [33] conducted a study. In this study 0.2 mm and 0.3 mm nozzle diameters were used and samples were printed. The difference of finished products can be observed by referring to Figure 8 and Figure 9 below. It is observed that the 0.3 mm nozzle diameter is more consistent in providing than the 0.2 mm nozzle diameter. It is estimated that finished product of 0.2 mm nozzle diameter should have better mechanical properties because of thin layers but it is inconsistent, which can also be seen from the side of the parts. Main reason of this matter can be explained as pressure drop caused by different nozzle diameters does affect the road width which in turn affects the accuracy of the finished parts.

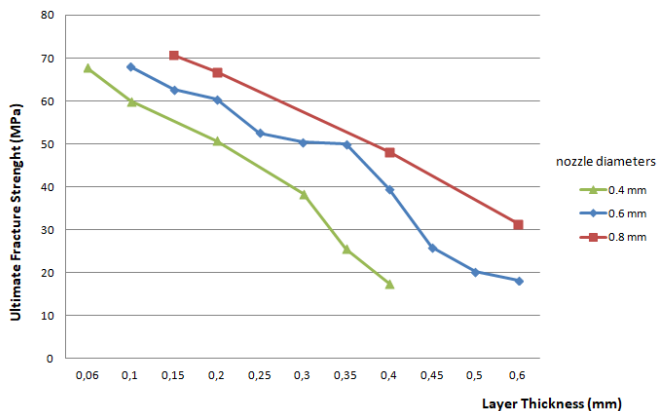


Fig. 7 Experimental data on the influence of geometrical parameters of 3D printing (nozzle diameter and layer thickness) on fabricated components' strength [37]

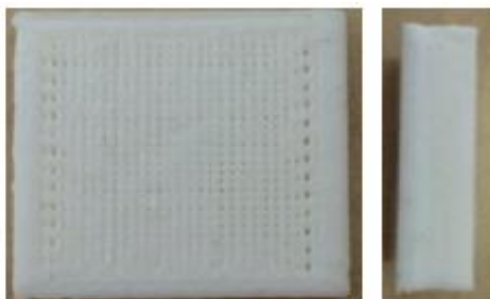


Fig. 8 Consistent road width printed by the 0.3 mm nozzle diameter [33]

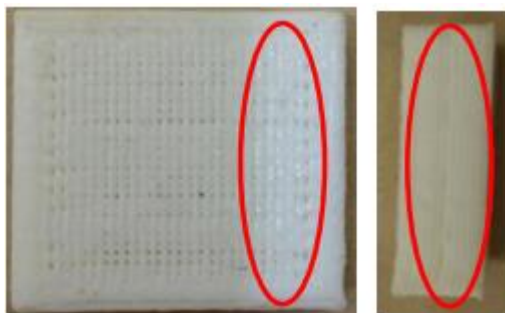


Fig. 9 Inconsistent road width printed by the 0.2 mm nozzle diameter [33]

2.5. Raster Angle

The angle between the path of the nozzle and the X-axis of the printing platform is known as raster angle which can be selected 0° to 90° [53].

Raster angle is one of the major parameters affecting the mechanical strength and geometric accuracy of components fabricated by 3D printed technologies. Depending on the angle of the filaments relative to the direction of the force applied, the distribution of stress in the filaments will be different. When the filaments are in parallel by applied force, a pure tensile stress state appears. In other orientation a mix of tensile stress and shear stress are happened. That is because the best results of the ultimate tensile stress, yield

stress and elasticity modulus were observed for a raster angle of $0^\circ/90^\circ$ [35]. In the most of studies investigating the effect of different parameters on the strength of FDM technologies the mechanical properties are tested on flat samples oriented horizontally during the printing process [37]. Letcher and Waytashek [55] showed that the mechanical properties such as the ultimate tensile strength can be improved by exchanging the raster angle of specimens made of PLA

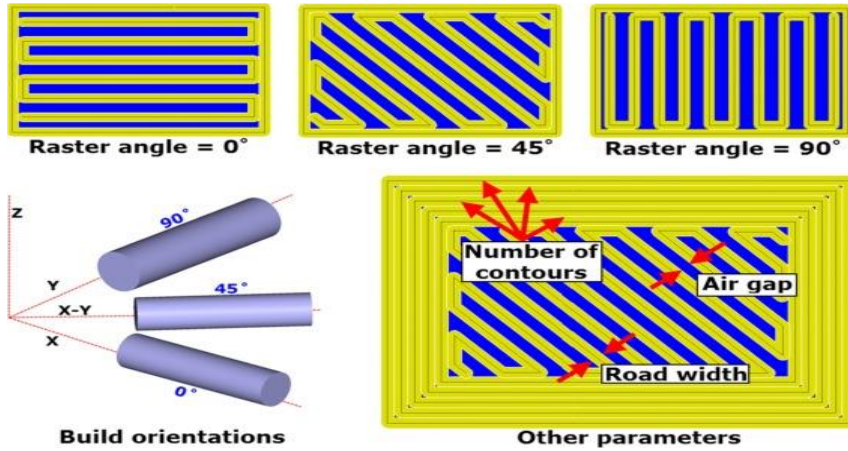


Fig.10 Raster angles [54]

According to Montero et al.'s [56] results of study, strength values of producing of material with various raster angles via fused deposition modeling and injection molded material is given in Fig.11 and Fig.12.

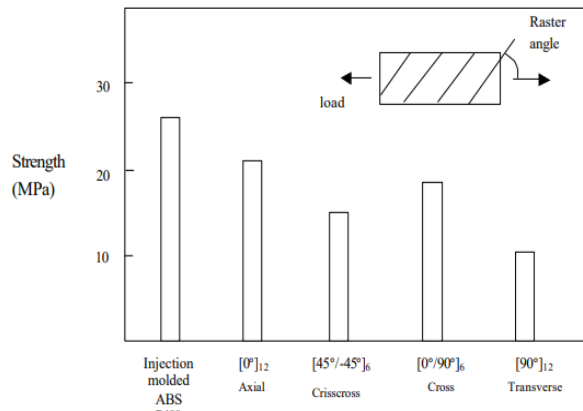


Fig. 11 Strength of specimens with various raster (-0.003 air gap) compared with injection molded ABS P400 [56]

According to another experimental study Sood et al. [47] small raster angles are not preferable because they will cause long raster. Because of this stress accumulation will increase the along the direction of deposition resulting in more distortion and hence weak bonding. But there is also an advantage of small raster angle. It means that raster is inclined along the direction of loading and will offer more resistance thus strength will improve.

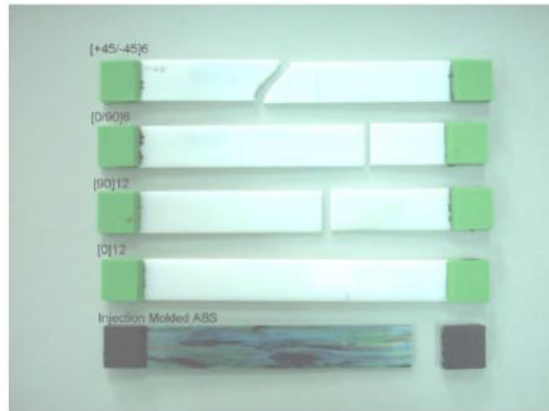


Fig. 12 Failure modes of the specimens with various raster orientations [56]

2.6. Layer Thickness

The most important parameter that affects surface roughness is layer thickness. Low layer thickness ensures better adhesion between layers. In Fernandes et al. reported study, in the specimens with low layer thickness (0.1 mm) the highest ultimate strength and yield stress values were obtained [35]. To explain this matter, the interfaces between the layers must be analyzed. Earlier studies on these interfaces prove that they are morphologically very similar to weld or knit lines in injection-molded parts. In spite of this, the mechanical strength of 3D printed components is lower than that of homogeneous products made of the same material [37-57]. The diameter of the nozzle is a major determining parameter in the minimum layer thickness. For instance, for the Ultimaker 2 machine with 0.4-mm nozzle the minimum layer thickness proposed by the printer manufacturer was 0.06 mm. The thicker layers are used to complete the image and practically are achievable up to the 80% of nozzle diameter [37]. SEM images of specimens with different layer thickness; relatively small and relatively large layer thickness is shown in Fig. 13.

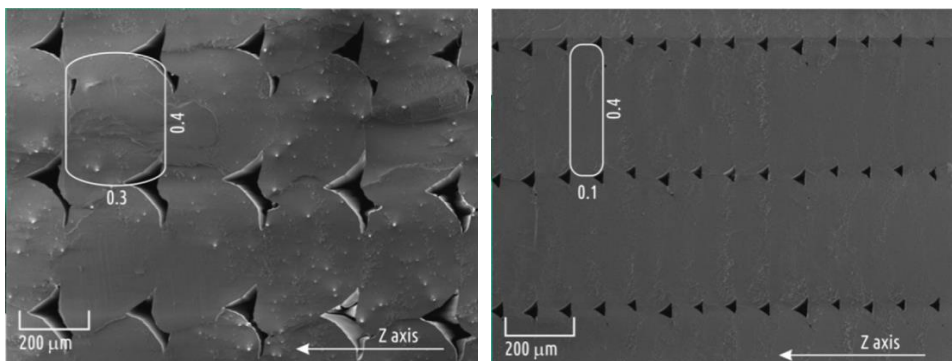


Fig. 13 The SEM images of specimens with different layer thickness: relatively large (top) and relatively small (bottom) layer thickness [37]

Once again Kuznetsov et al [37], to explain the relationship between layer height and part strength conducted experimental study. According to study layer height had the greatest influence on intra-layer cohesion. When layer height was increased for all type of nozzle (0.4, 0.6, and 0.8 mm), part strength decreased. For the samples under study, the decrease of strength when changing layer height from minimum to maximum was about 3.5 times.

In addition, layer thickness is directly related to manufacturing cost, as layer thickness increases printing time decreases.

2.7. Printing pattern and infill density

3D printers utilize various infill patterns as shown in Fig. 14 and infill patterns known as, line, grid, concentric, cubic, triangles, octagram spiral, hecilinear, archimedeanchord, tetrahedral, honeycomb and zigzag, hilburt curve, etc. The most important parameter that affects material strength is infill density. The conducted studies findings proved that the infill density percentage influences the mechanical properties printing accuracy of the finished [58]. Yah et al. [59] showed that the line pattern, especially in tensile properties performed better than rectilinear. The printing pattern in addition to mechanical properties affects the printing time and material usage. The results of Patel's study proved that the concentric infill pattern in comparison to the line and grid infill patterns had the fastest printing time. The tensile strength of specimens produced by the line infill pattern was higher than the ones produced by grid and the concentric infill pattern [60]. The results obtained in Fernandez-Vicente et al. [61] showed that the effect of the various printing pattern in maximum tensile strength is less than 5%. The honeycomb pattern due to facilitating the load transfer between layers provides higher mechanical strength [62].

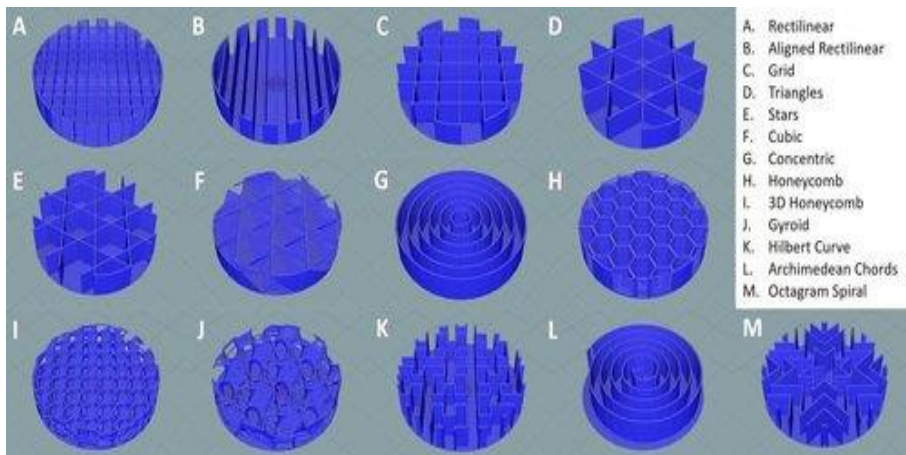


Fig. 14 Different types of printing pattern [63]

Printing parameter such as the internal infill density and pattern affect the mechanical behavior of porous products [64-65]. The increase in infill density causes an increase in tensile and compressive strength. In the improvement of mechanical strength of 3D printed products, the infill density is more effective than the printing pattern [66]. Roohani et al. investigated fatigue resistance of scaffolds that have different patterns and according to study, scaffolds with hexagonal design showed highest fatigue resistance [62].

Small filling rate setting can provide reducing filament consumption, shorting printing time, increasing forming efficiency further in actual manufacturing practice. Nevertheless, too small filling rate causes adhesive strength and support insufficient. The adhesive strength of interlayers increases rapidly with filling rate. More specifically, it increases slowly before the filling rate up to 40% and after that, increases faster. Experiments show that filling rate which smaller than 20% can save filament consumption and shorten processing cycle when nonfunctional prototypes or small tensile functional prototypes are deposited [67].

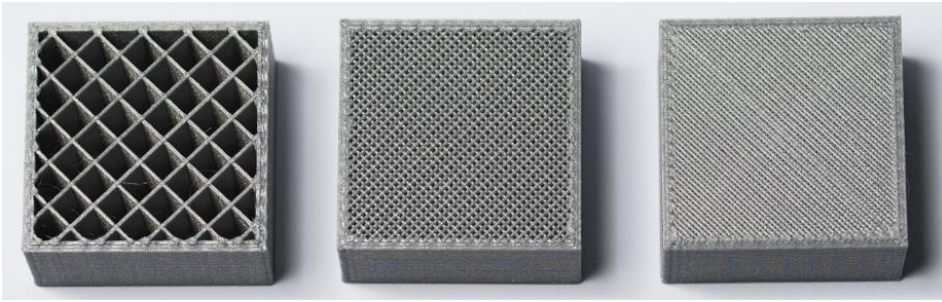


Fig.15 Various infill density used in 3D printers [66]

In addition of this, according to Kaya et. al.'s study [34], relationship between densities, infill structures and vibration are investigated. Study is carried out at three different filling rate (25%, 50%, 75%) for five different manufacturing methods (Diagonal 45°/-45° (D1, D2, D3), Diagonal 60°/-60° (D4, D5, D6) , Triangular 60°/-60° (D7, D8, D9), Wiggle (D10, D11, D12), Honeycomb 0°/120°/-120° (D13, D14, D15)).

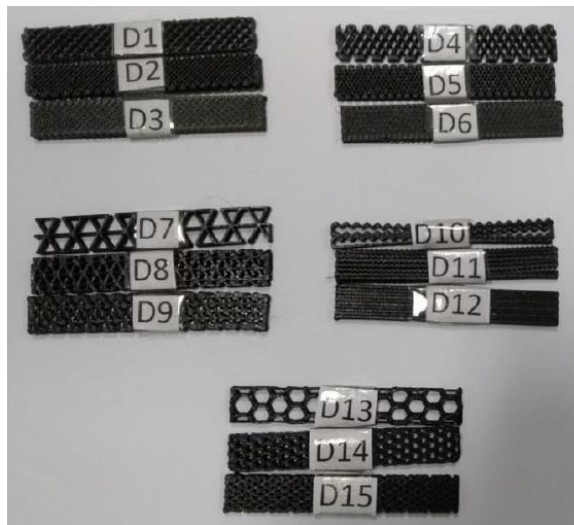


Fig.16. 3D printed samples for five different manufacturing methods [34]

As a result of Kaya et. al.'s study [34], all manufacturing methods with 50% infill ratio except honeycomb manufacturing method were determined to have the most number of vibration fluctuations. Number of vibration fluctuations occurring in manufacturing methods are interpreted according to calculated variance values. Unlike the aforementioned situation in hone honeycomb method, the increment of infilling rate causes the increase of vibration fluctuations.

When the vibrations acting on the 3D printer body are considered, the method with minimum fluctuation is observed in honeycomb structure with %25 infill ratio (D13). Besides that, maximum fluctuation is found in wiggle structure with %75 infill ratio (D12). Furthermore, minimum mean vibration amplitude is seen to be occurred that in honeycomb structure with %25 infill ratio (D13). In addition, test results are revealed that

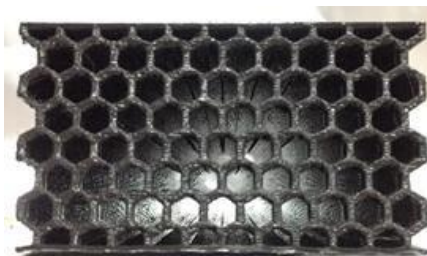
maximum mean vibration amplitude is wiggly structure with %75 infill ratio (D12). The triangular method is the second most suitable method to choose when considering the fluctuations in the vibration amplitudes and the maximum amplitude.

In a different study that conducted by Akbaş et al. [68], the effect of knitting parameters on product strength was investigated experimentally in three-dimensional printer used in thermoplastic filament production. Different production parameters such as construction angle, section grid width and construction width were analyzed experimentally. Parameters for construction angle 30° and 60°, for construction width 0,016, 0,024 and 0,032mm and finally for section grid width 0,016, 0,024 and 0,032 were used. As a result, the most important parameter that affects the material strength was determined as section grid width. Second important parameter was determined as construction width and the last one was determined as construction angle. As section on grid width decreases and as construction width increases (these two parameters can be defined as infill rate), strength of material increases.

Table 3. Results of tensile test [68]

30° Construction (raster) angle					60° Construction (raster) angle				
Exp. No	Construction Width (mm)	Section Grid Width (mm)	Yield Strength (MPa)	Tensile Strength (MPa)	Exp. No	Construction Width (mm)	Section Grid Width (mm)	Yield Strength (MPa)	Tensile Strength (MPa)
D1		0.016	23.9	25	D10		0.016	23.2	28.6
D2	0.016	0.024	14.5	15.3	D11	0.016	0.024	14.8	17.2
D3		0.032	9.4	10	D12		0.032	9.5	10.1
D4		0.016	11	11.4	D13		0.016	10.9	11.5
D5	0.024	0.024	19.3	20.2	D14	0.024	0.024	19.4	20.1
D6		0.032	30.5	31.9	D15		0.032	30.4	31.7
D7		0.016	31.4	32.3	D16		0.016	30.8	31.9
D8	0.032	0.024	23.8	24.6	D17	0.032	0.024	23.6	24.7
D9		0.032	12.6	12.9	D18		0.032	12.6	13.5

In another study, Ercan et al. , investigated compression properties of sandwich panels produced by FDM. In this study, horizontal honeycomb, vertical honeycomb, horizontal truss, vertical truss, cubic and gyroid unit cell topologies were used as core of sandwich panels [69]. The unit cell sizes of these different cell topologies were 5mm × 5mm. All cellular structures were designed at 40% relative density by changing only the cell thickness. The designed cellular structures were produced by Ultimaker 3 Extended device with the same parameters and PLA material. Produced samples were tested in Shimadzu 250kN test device in accordance with ASTM C365. Based on the pressure tests, the maximum compressive stresses and the elastic modulus of the sandwich panels with different cores were examined and the effect of the cell topology on the compression properties was investigated.



(a)



(b)

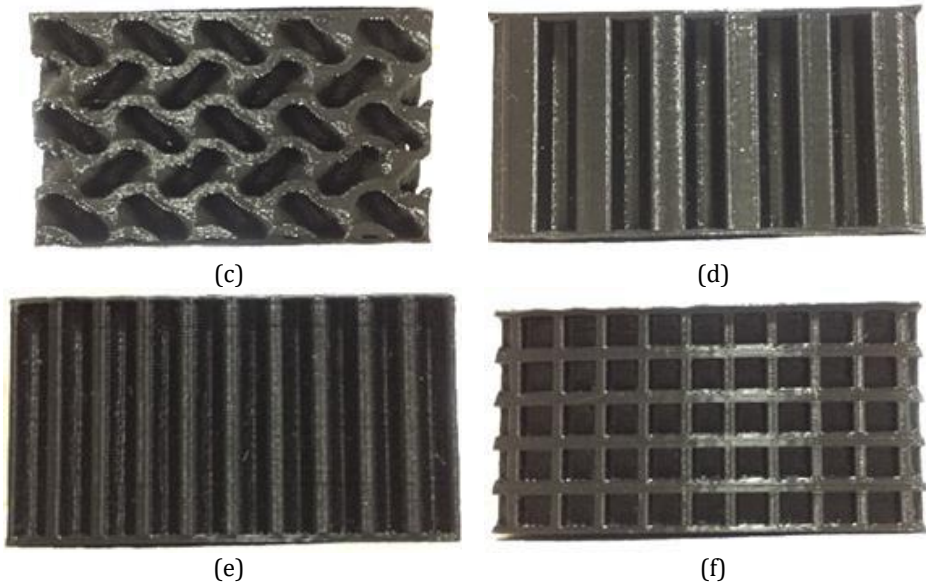
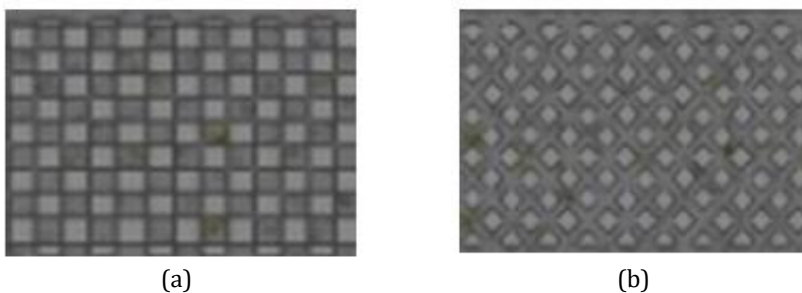


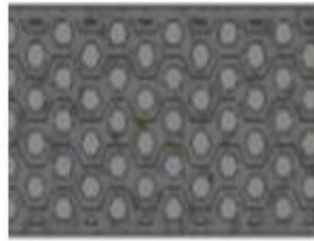
Fig. 17: Types of unit cells [69] (a) horizontal honeycomb (b) horizontal truss (c) gyroid (d) vertical honeycomb (e) vertical truss, and (f) cubic

According to experimental result of compression test, the best mechanical strength belongs to cubic unit cell with 571 MPa value. Other unit cells that have highest strength respectively are: vertical truss, vertical honeycomb, gyroid, horizontal honeycomb and horizontal truss unit cell.

Infill types and infill density also affect hardness of manufactured components with rapid prototyping technique. In Bögrekci et al.'s study [70], some infill types like rectilinear (linear), grid (diamond) and honeycomb (hexagonal) were chosen and for each infill types; specimens were produced with the infill density values of 15, 25, 50, 75 and 100%.

Hardness of produced specimens were measured with Emco-test DuraScan micro hardness machine. As a result hexagonal infill with density of 100% showed the highest hardness and also the hardness patterns could be presented from high to low as Hexagonal > Linear > Diamond.





(c)

Fig. 18 Specimens with (a) Linear (b) Diamond (c) Hexagonal infill types [70]

Table 4. The obtained results from micro hardness measurements in unit of N/mm² [68].

Infill Rate	Hexagonal (HV)	Linear (HV)	Diamond (HV)
15%	17.8	16.3	16.1
25%	18.9	16.8	16.4
50%	21.6	17.3	17.1
75%	22	17.9	17.5
100%	22.8	19.2	18

As a result of Bögrekci et. al's study high level density resulted in a low amount voids and high hardness values [70].

2.8. Air Gap

Air gap parameter is defined as the space between the beads of deposited FDM material. Schematic representation of positive and negative gap between the deposited beads is seen Figure 19. According to Alhubail et. al's study, setting layer thickness and raster width at low level could minimize the surface roughness in addition to the air gap at -0.01 mm and adjusting layer thickness and raster width at low level and the air gap at -0.01 mm can provide higher tensile strength. As a result of this study, surface roughness and tensile strength of processed parts are greatly influenced by air gap parameter [71].

Falck et al. reported that the fundamental factors affecting the mechanical strength of the final part are air gap and road angle. Voids that is found in the product are source of mechanical performance reduction in FDM [29].

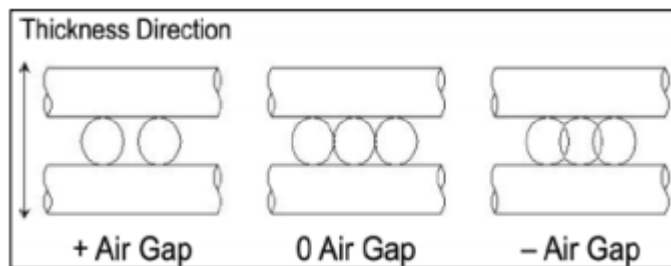


Fig. 19 Schematic representation of air gaps [71]

Air gaps and infills determine the dimension of the contact zone between filament roads and layers, so they affect bond strength and mechanical properties of part. According to studies which have about relationship between air gap and mechanical properties, when air gap is set as negative, mechanical properties are improved [72].

3. Conclusion

In the present paper, a review of all effective variants on the 3D printing technology has been conducted. It is observed that the mechanical performance and geometrical accuracy of the products fabricated by 3D printing technologies are highly affected by printing parameters. Metals, polymers, ceramics, concrete and composites are currently used in 3D printing. Despite existing a wide range of polymeric materials, ABS and PLA are the main polymers used in the majority of applications. The products made of PLA due to less internal stresses and better mechanical characteristics are preferred to the products made of ABS. The high extrusion temperature decreases the material viscosity and improves the bonding between the layers. Also, by increasing the temperature the circular section of extruded material became oval. So, the contact area between the layers extended. By providing the adequate thermal behavior of the system, the cohesion between layers can be improved. Extrusion speed affects surface roughness and quality of the produced components. Nozzle diameter has a significant influence on interlayer cohesion. Given constant layer height, printing with a larger nozzle resulted in increased strength. The advantages of larger nozzles became even more evident with greater layer thickness. Depending on the angle of the filaments relative to the direction of the force applied, the distribution of stress in the filaments will be different. The maximum ultimate tensile or compression strength value is achieved when the raster angle is 0°. In this case, the filaments become parallel by the applied force. The printing pattern in addition to mechanical properties affects the printing time and material usage. The tensile strength of specimens produced by the line infill pattern is high in comparison to other infill patterns. The increase in infill density causes an increase in tensile and compressive strength. Air gaps and infills determine the dimension of the contact zone between filament roads and layers, so they affect bond strength and mechanical properties of part. The diameter of the nozzle is determining in the minimum layer thickness. The low layer thickness ensures better adhesion between layers and provides the high ultimate strength and yield stress values. In addition, layer thickness is directly related to manufacturing cost, as layer thickness increases printing time decreases.

References

- [1] Additive Manufacturing ASTM52900 - 15.
- [2] Xu T, Zhao W, Zhu J, Albanna, M, Yoo J. and Atala, A. Complex heterogeneous tissue constructs containing multiple cell types prepared by inkjet printing technology. *Biomaterials*, 2013; 34(1), pp.130-139.
<https://doi.org/10.1016/j.biomaterials.2012.09.035>
- [3] Kruth J. Material Incess Manufacturing by Rapid Prototyping Techniques. *CIRP Annals*. 1991;40(2):603-614.
[https://doi.org/10.1016/S0007-8506\(07\)61136-6](https://doi.org/10.1016/S0007-8506(07)61136-6)
- [4] Wohlers T. Tracking Global Growth in Industrial-Scale Additive Manufacturing. *3D Printing and Additive Manufacturing*. 2014;1(1):2-3.
- [5] Kruth J, Levy G, Klocke F, Childs T. Consolidation phenomena in laser and powder-bed based layered manufacturing. *CIRP Annals*. 2007;56(2):730-759.
<https://doi.org/10.1016/j.cirp.2007.10.004>

- [6] Peres F, Martin C. Design methods applied to the selection of a rapid prototyping resource. 1999 7th IEEE International Conference on Emerging Technologies and Factory Automation Proceedings ETFA '99 (Cat No99TH8467). <https://doi.org/10.1109/ETFA.1999.815386>
- [7] New manufacturing milestone: 30,000 additive fuel nozzles | GE Additive [Internet]. Ge.com. 2020 [cited 9 April 2020]. Available from: <https://www.ge.com/additive/blog/new-manufacturing-milestone-30000-additive-fuel-nozzles>
- [8] Bhushan B, Caspers M. An overview of additive manufacturing (3D printing) for microfabrication. *Microsystem Technologies*. 2017; 23(4): 1117-1124.
- [9] Woesz A. Rapid Prototyping to Produce Porous Scaffolds with Controlled Architecture for Possible use in Bone Tissue Engineering. *Virtual Prototyping & Bio Manufacturing in Medical Applications*. 2010:171-206. https://doi.org/10.1007/978-0-387-68831-2_9
- [10] Salonitis K, Tsoukantas G, Stavropoulos P, Stournaras A. A critical review of stereolithography process modeling. 3rd International Conference on Advanced Research in Virtual and Rapid Prototyping, Leiria, 377-384, 2003.
- [11] Pham DT., Dimov SS. *Rapid Prototyping Process*. Rapid Manufacturing, 1st edition, Springer, London, 2001: 19-40, 978-1-4471-0703-3. <https://doi.org/10.1007/978-1-4471-0703-3>
- [12] Sood A, Ohdar R, Mahapatra S. Experimental investigation and empirical modelling of FDM process for compressive strength improvement. *Journal of Advanced Research*. 2012;3(1):81-90. <https://doi.org/10.1016/j.jare.2011.05.001>
- [13] Nikzad M, Masood S, Sbarski I. Thermo-mechanical properties of a highly filled polymeric composites for Fused Deposition Modeling. *Materials & Design*. 2011;32(6):3448-3456. <https://doi.org/10.1016/j.matdes.2011.01.056>
- [14] Shen N, Chou K. Numerical thermal analysis in electron beam additive manufacturing with preheating effects. *Proceedings of the 23rd annual international solid freeform fabrication symposium, Austin, 774-784, 2012*. <https://doi.org/10.1115/MSEC2012-7253>
- [15] Rochus P, Plessier J.Y., Elsen, M.V., Kruth J.P., Carrus R, Dormal T. New applications of rapid prototyping and rapid manufacturing (RP/RM). *Acta Astronautica*, 2007; 61(1-6), 352-359. <https://doi.org/10.1016/j.actaastro.2007.01.004>
- [16] Rooks B. Rapid tooling for casting prototypes. *Assembly Automation*. 2002;22(1):40-45. <https://doi.org/10.1108/01445150210416664>
- [17] Patel JP, Patel CP, Patel UJ. A review on various approach for process parameter optimization of fused deposition modeling (FDM) process and Taguchi approach for optimization. *International Journal of Engineering Research and Applications*. 2012; 2(2):361-365.
- [18] Masood SH, Rattanawong W, Iovenitti P. A generic algorithm for a best part orientation system for complex parts in rapid prototyping. *Journal of Materials Processing Technology*. 2003;139(1-3):110-116. [https://doi.org/10.1016/S0924-0136\(03\)00190-0](https://doi.org/10.1016/S0924-0136(03)00190-0)
- [19] Negi S, Dhiman S, Sharma RK. Basics and applications of rapid prototyping medical models. *Rapid Prototyping Journal* 2014; 20(3), 256-267. <https://doi.org/10.1108/RPJ-07-2012-0065>
- [20] Sugavaneswaran M, Arumaikkannu G. Modelling for randomly oriented multimaterial additive manufacturing component and its fabrication. *Materials and Design*, 2014; 54: 779-785. <https://doi.org/10.1016/j.matdes.2013.08.102>
- [21] Saraçyakupoğlu T. The Qualification of the Additively Manufactured Parts in the Aviation Industry. *American Journal of Aerospace Engineering*, 2019; 6(1): 1-10. [doi: 10.11648/j.ajae.20190601.11](https://doi.org/10.11648/j.ajae.20190601.11)

- [22] Winder J, Cooke RS, Gray J, Fannin T, Fegan T. Medical rapid prototyping and 3D CT in the manufacture of custom cranial titanium plates. *Journal of Medical Engineering & Technology*, 1999; 23:26-28. <https://doi.org/10.1080/030919099294401>
- [23] Bikas H, Stavropoulos P, Chryssolouris G. Additive manufacturing methods and modelling approaches: a critical review. *The International Journal of Advanced Manufacturing Technology*, 2016; 83(1-4), 389-405. <https://doi.org/10.1007/s00170-015-7576-2>
- [24] Kalita, SJ, Bose S, Hosick HL, Bandyopadhyay A. Development of controlled porosity polymer-ceramic composite scaffolds via fused deposition modeling. *Materials Science and Engineering*, 2003; C, 23(5): 611-620. [https://doi.org/10.1016/S0928-4931\(03\)00052-3](https://doi.org/10.1016/S0928-4931(03)00052-3)
- [25] Ngo TD, Kashani A, Imbalzano G, Nguyen KT, Hui D. Additive manufacturing (3D printing): A review of materials, methods, applications and challenges. *Composites Part B: Engineering*, 2018; 143: 172-196. <https://doi.org/10.1016/j.compositesb.2018.02.012>
- [26] Singh R, Garg HK, Singh N, Hui D, Singh R, Ahuja IPS, Feo L, & Fraternali F. Recycling of plastic solid waste: A state of art review and future applications. *Composites Part B: Engineering*, 2017;115: 409-422.
- [27] Onder O. GE Aviation Turkey Additive Manufacturing Technologies R&D Lab. 4th international congress on 3d printing technologies and digital industry, Antalya, XXXVIII, 2019.
- [28] Tasdelen MA, Bingöl M, Yılmaz Y, Kahramaner H. Performances of recycled thermoplastics in 3D printer. 4th international congress on 3d printing technologies and digital industry, Antalya, 182-191, 2019.
- [29] Falck R, Dos Santos JF, Amancio-Filho ST. An overview on the materials and mechanical behavior used in fused deposition modeling. In 75th Annual Technical Conference and Exhibition of the Society of Plastics Engineers, SPE ANTEC Anaheim 1689-1695, 2017.
- [30] Jerez-Mesa R, Gomez-Gras G, Travieso-Rodriguez JA, Garcia-Plana V. A comparative study of the thermal behavior of three different 3D printer liquefiers. *Mechatronics*, 2018; 56: 297-305. <https://doi.org/10.1016/j.mechatronics.2017.06.008>
- [31] Kulkarni P, Marsan A, Dutta D. A review of process planning techniques in layered manufacturing. *Rapid prototyping journal*, 2000; 6(1): 18-35. <https://doi.org/10.1108/13552540010309859>
- [32] Demircioğlu P, Böğrekcı İ, Sucuoğlu HS, Demir N. The effect of extrusion speed on surface roughness for 3D printed parts. 4th international congress on 3d printing technologies and digital industry, Antalya, 269-275, 2019.
- [33] Sukindar NA, Ariffin MKA, Baharuddin, BHT, Jaafar CNA, Ismail MIS. Analyzing the effect of nozzle diameter in fused deposition modeling for extruding polylactic acid using open source 3D printing. *Jurnal Teknologi*, 2016; 78(10): 7-15. <https://doi.org/10.11113/jt.v78.6265>
- [34] Kaya KD, Yılmaz S, Bayramoğlu K, Göksu B. Determination of working parameters of 3D printers on various operation modes with different sensing systems. 4th international congress on 3d printing technologies and digital industry, Antalya, 79-92, 2019.
- [35] Fernandes J, Deus AM, Reis L, Vaz MF, Leite M. Study of the influence of 3D printing parameters on the mechanical properties of PLA. *Proceedings of the 3rd International Conference on Progress in Additive Manufacturing (Pro-AM 2018)*, Singapore, 547-552 2018.
- [36] Kim H, Park E, Kim S, Park B, Kim N, Lee S. Experimental study on mechanical properties of single-and dual-material 3D printed products. *Procedia Manufacturing*, 2017; 10: 887-897. <https://doi.org/10.1016/j.promfg.2017.07.076>

- [37] Kuznetsov VE, Solonin AN, Urzhumtsev OD, Schilling R, Tavitov AG. Strength of PLA components fabricated with fused deposition technology using a desktop 3D printer as a function of geometrical parameters of the process. *Polymers*, 2018; 10(3), 313. <https://doi.org/10.3390/polym10030313>
- [38] Sagias VD, Giannakopoulos, KI, Stergiou C. Mechanical properties of 3D printed polymer specimens. *Procedia Structural Integrity*, 2018; 10: 85-90. <https://doi.org/10.1016/j.prostr.2018.09.013>
- [39] Tymrak BM, Kreiger M, Pearce JM. Mechanical properties of components fabricated with open-source 3-D printers under realistic environmental conditions. *Materials & Design*, 2014; 58: 242-246. <https://doi.org/10.1016/j.matdes.2014.02.038>
- [40] Lee CS, Kim SG, Kim HJ, Ahn SH. Measurement of anisotropic compressive strength of rapid prototyping parts. *Journal of materials processing technology*, 2007; 187, 627-630. <https://doi.org/10.1016/j.jmatprotec.2006.11.095>
- [41] Warnung L, Estermann SJ, Reisinger A. Mechanical Properties of Fused Deposition Modeling (FDM) 3D Printing Materials. *RTEjournal-Fachforum für Rapid Technologien*, 2018; 2018(1).
- [42] Justo J, Távara L, García-Guzmán L, París F. Characterization of 3D printed long fibre reinforced composites. *Composite Structures*, 2018; 185: 537-548. <https://doi.org/10.1016/j.compstruct.2017.11.052>
- [43] Zhong Li F, Zhang Z, Song L, Li Z. Short fiber reinforced composites for fused deposition modeling. *Materials Science and Engineering: A*, 2001; 301(2), 125-130. [https://doi.org/10.1016/S0921-5093\(00\)01810-4](https://doi.org/10.1016/S0921-5093(00)01810-4)
- [44] Ning F, Cong W, Qiu J, Wei J, Wang S. Additive manufacturing of carbon fiber reinforced thermoplastic composites using fused deposition modeling. *Composites Part B: Engineering*, 2015; 80: 369-378. <https://doi.org/10.1016/j.compositesb.2015.06.013>
- [45] (<https://www.artiboyut.com/index.php/tr/bilgi-bankasi/39-3d-yazici-filament-ozellikleri>) Accessed 1 October 2019.
- [46] Fodran E, Koch M, Menon U. Mechanical and dimensional characteristics of fused deposition modeling build styles. *International Solid Freeform Fabrication Symposium*, California, 419-442, 1996.
- [47] Sood AK, Ohdar RK, Mahapatra SS. Parametric appraisal of mechanical property of fused deposition modelling processed parts. *Materials & Design*, 2010; 31(1), 287-295. <https://doi.org/10.1016/j.matdes.2009.06.016>
- [48] Sun Q, Rizvi GM, Bellehumeur CT, Gu P. Effect of processing conditions on the bonding quality of FDM polymer filaments. *Rapid Prototyping Journal*, 2008; 14(2), 72-80. <https://doi.org/10.1108/13552540810862028>
- [49] Bellehumeur C, Li L, Sun Q, Gu P. Modeling of bond formation between polymer filaments in the fused deposition modeling process. *Journal of Manufacturing Processes*, 2004; 6(2), 170-178. [https://doi.org/10.1016/S1526-6125\(04\)70071-7](https://doi.org/10.1016/S1526-6125(04)70071-7)
- [50] Bhalodi D, Zalavadiya K, Gurralla PK. Influence of temperature on polymer parts manufactured by fused deposition modeling process. *Journal of the Brazilian Society of Mechanical Sciences and Engineering*, 2019; 41(3), 113. <https://doi.org/10.1007/s40430-019-1616-z>
- [51] Lanzotti A, Del Giudice DM, Lepore A, Staiano G, Martorelli M. On the geometric accuracy of RepRap open-source three-dimensional printer. *Journal of Mechanical Design*, 2015; 137(10), 101703. <https://doi.org/10.1115/1.4031298>
- [52] <https://blog.prusaprinters.org/everything-about-nozzles-with-a-different-diameter> Accessed 2 August 2019.
- [53] Wu W, Ye W, Wu Z, Geng P, Wang Y, Zhao, J. Influence of layer thickness, raster angle, deformation temperature and recovery temperature on the shape-memory effect of

- 3D-printed polylactic acid samples. *Materials*, 2017; 10(8), 970. <https://doi.org/10.3390/ma10080970>
- [54] Mohamed OA, Masood SH, Bhowmik JL, Somers AE. Investigation on the tribological behavior and wear mechanism of parts processed by fused deposition additive manufacturing process. *Journal of Manufacturing Processes*, 2017; 29: 149-159. <https://doi.org/10.1016/j.jmapro.2017.07.019>
- [55] Letcher T, Waytashek M. Material property testing of 3D-printed specimen in PLA on an entry-level 3D printer. In ASME 2014 international mechanical engineering congress and exposition, Quebec, V02AT02A014-V02AT02A014, 2014. <https://doi.org/10.1115/IMECE2014-39379>
- [56] Montero M, Roundy S, Odell D, Ahn SH, Wright PK. Material characterization of fused deposition modeling (FDM) ABS by designed experiments. *Society of Manufacturing Engineers*, 2001; 10(13552540210441166): 1-21.
- [57] Kühnert I, Spörer Y, Brüning H, Tran NHA, Rudolph N. Processing of poly (lactic acid), In *Industrial Applications of Poly (lactic acid)*, 2017: 1-33, 978-3-319-75458-1. https://doi.org/10.1007/12_2017_30
- [58] Pei E, Melenka GW, Schofield JS, Dawson MR, Carey JP. Evaluation of dimensional accuracy and material properties of the MakerBot 3D desktop printer. *Rapid Prototyping Journal*, 2015; 21(5), 618-627. <https://doi.org/10.1108/RPJ-09-2013-0093>
- [59] Aw Y, Yeoh C, Idris M, Teh P, Hamzah K, Sazali S. Effect of printing parameters on tensile, dynamic mechanical, and thermoelectric properties of FDM 3D printed CABS/ZnO composites. *Materials*, 2018; 11(4), 466. <https://doi.org/10.3390/ma11040466>
- [60] Patel DM. Effects of infill patterns on time, surface roughness and tensile strength in 3D printing. *Int. J. Eng. Dev. Res*, 2017; 5: 566-569.
- [61] Fernandez-Vicente M, Calle W, Ferrandiz S, Conejero A. Effect of infill parameters on tensile mechanical behavior in desktop 3d printing. *3d printing and additive manufacturing*, 2016, 3.3: 183-192. <https://doi.org/10.1089/3dp.2015.0036>
- [62] Roohani-Esfahani SI, Newman P, Zreiqat H. Design and fabrication of 3D printed scaffolds with a mechanical strength comparable to cortical bone to repair large bone defects. *Scientific reports*, 2016; 6: 19468. <https://doi.org/10.1038/srep19468>
- [63] <https://allevi3d.com/build-with-life/infill-slic3r> Accessed 5 June 2019.
- [64] Sharma R, Singh R, Penna R, Fraternali F. Investigations for mechanical properties of Hap, PVC and PP based 3D porous structures obtained through biocompatible FDM filaments. *Composites Part B: Engineering*, 2018; 132: 237-243. <https://doi.org/10.1016/j.compositesb.2017.08.021>
- [65] Tanikella NG, Wittbrodt B, Pearce JM. Tensile strength of commercial polymer materials for fused filament fabrication 3D printing. *Additive Manufacturing*, 2017, 15, 40-47. <https://doi.org/10.1016/j.addma.2017.03.005>
- [66] Al CM, Yaman U. Improving the strength of additively manufactured objects via modified interior structure. *AIP conference proceedings AIP publishing*, 2017;1896 (1): 040003. <https://doi.org/10.1063/1.5008029>
- [67] Pan AQ, Huang ZF, Guo RJ, Liu J. Effect of FDM process on adhesive strength of polylactic acid (PLA) filament. In *Key Engineering Materials*, 2016; 667: 181-186, Trans Tech Publications. <https://doi.org/10.4028/www.scientific.net/KEM.667.181>
- [68] Akbas OA, Yıldız T, Sur G. Effect of construction parameters on product strength in 3D printers. 4th international congress on 3d printing technologies and digital industry, Antalya, 99-105, 2019.
- [69] Ercan N, Yunus DE. Investigation compression properties of sandwich panels produced by FDM. 4th international congress on 3d printing technologies and digital industry, Antalya, 221-229, 2019.

- [70] Böğrekci İ, Demircioğlu P, Sucuoğlu HS, Turhanlar O. The effect of the infill type and density on hardness of 3D printed parts. 4th international congress on 3d printing technologies and digital industry, Antalya, 276-283, 2019.
- [71] Alhubail M, Alenezi D, Aldousiri B. Taguchi-based optimisation of process parameters of fused deposition modelling for improved part quality. *International Journal of Engineering Research and Technology*, 2013; 2.12 : 2519.
- [72] Popescu D, Zapciu A, Amza C, Baci F, Marinescu R. FDM process parameters influence over the mechanical properties of polymer specimens: A review. *Polymer Testing*, 2018; 69: 157-166. <https://doi.org/10.1016/j.polymertesting.2018.05.020>

Blank Page



Research Article

Investigation of recycled aluminum matrix composites reinforced with copper and γ -alumina manufactured by sinter and sinter + forging methods

Halil Murat Enginsoy

Department of Mechanical Engineering, Uşak University, Uşak, Turkey
School of Mechanical and Manufacturing Engineering, SUPMECA/PARIS, France

Article Info

Article history:

Received 22 Aug 2020

Revised 28 Sep 2020

Accepted 30 Sep 2020

Keywords:

Hybrid Composites;

Static Compression;

3P-Bending;

Impact test;

Wear-Creep;

SEM analysis

Abstract

The present work reviews the toughening mechanisms and microstructural analyses of recycled hybrid metal matrix composites (aluminium based) reinforced with γ -alumina and pure recycled copper. This composite was manufactured by sintering and sinter + forging called the combined process. To analyze the mechanical / physical behavior of hybrid metal matrix composite materials; quasi-static compression, three-point bending (3PB), low velocity impact (dynamic compression) experiments were carried out. Additionally, wear and creep tests were conducted with a nanoindenter to evaluate the wear and time dependent behaviour of this composite. Evaluation of the microstructure of hybrid metal matrix composites were performed with Scanning Electron Microscope (SEM) supported by Energy Dispersive Spectrometer (EDS) analysis. The results showed that the composites have homogeneous structure without porosity and very homogeneous distribution of fine γ -alumina (Al_2O_3) and copper particles. Sinter + forging process yielded a material that had higher strength, hardness and better resistance to wear. This composite will be targeted for linkage applications where high toughness and high surface damage resistance is required.

© 2020 MIM Research Group. All rights reserved.

1. Introduction

A new family of aluminium-based composites is extensively being used in the different industrial areas (aerospace, automotive etc.) doped with different metal and ceramic reinforcements to improve their mechanical and tribological properties [1-8]. When the γ -alumina ceramic reinforcement is added to the aluminum matrix, it can significantly increase the wear resistance along with the mechanical / physical properties of such hybrid metal matrix composite materials. The addition of copper reinforcement together with γ -alumina can give a good combination of high ductility and high strength [5, 9, 13-18].

The manufacturing operation that we determine the combined sinter+forging process used to manufacture the aluminium-based composites can offer simplicity in processing and lower the manufacturing costs as these composites are produced from recycled constituents known as fresh scrap materials. In this current research, novel composite reinforced with γ -alumina and copper was designed for possible use in linkage/connector parts in aeronautical applications [7, 11, 16].

Corresponding author: murat.enginsoy@usak.edu.tr

orcid.org/0000-0002-8080-3238

DOI: <http://dx.doi.org/10.17515/resm2020.211me0822>

Res. Eng. Struct. Mat. Vol. 6 Iss. 4 (2020) 315-326

The composite design process from fresh scrap recycled components can be applied very well to optimally economical industrial parts for a minimized cost and fast production. As can be seen in the researches in the literature, the sinter+forging process is a manufacturing process that is defined as a process of forming close to high accuracy for the manufacturing of parts processed from fresh scrap materials [6-14]. Basically, this manufacturing method is the preferred method for bulk materials in different industrial areas. With a low-cost sintering accession for processing fine particle reinforced composites, it is ensured that industrial products always show a high performance under different service conditions. An economically minimized sintering approach for the manufacturing of fine particle reinforced composites provides high efficiency of mechanical behaviors of parts used in different industrial applications such as static compression, impact loading, 3-point bending, creep and fatigue. This principle set forth in our study can be applied to many other composite-based materials in many different industrial areas and at different scales. It reveals that very hard and strong parts can be attainable with this combined manufacturing method, but the fact that it can be performed at a lower cost than other processes suggested in the literature can be considered as one of the most important property of this method.

This material developed in this study based on the results of quasi-static compression, impact and wear tests can be recommended for use in areas where wear and high impact forces are expected.

2. Experimental Conditions

Within the scope of this study, an alternative hybrid metal matrix composite (aluminium based) with optimum economy was manufactured using fresh scrap recycled chips of two aluminum series Alumix-431 (50% wt) and AA1050 (50% wt) supplied by a French aerospace company. The two aluminum series (after atomization) were mixed by planetary ball mill for 1 hour by high energy milling and doped with copper γ - Alumina (Al_2O_3). The final composition was homogenized for 4 hours by ball milling. Pure nano-aluminum (<3-5 wt %) powder was added to the mixture to obtain a homogeneous mixture with good wettability of the reinforcements with the matrix. The final composition is given in Table 1 and the chemical composition of Alumix-431 supplied by the aerospace company in Table 2 (Analyses were carried out by the relevant aerospace company).

Table 1. Compositions of the designed composite (wt. %)

Specimen Name	Alumix-431+AA1050 (Matrix,1:1)	Cu	γ - Al_2O_3	Zn-St
MENG	Balance	25	15	2

Table 2. Scrap Alumix-431 (wt. %) chemical composition

Element	Al	Cu	Mg	Zn
wt. %	91.45	0.55	2.5	5.5

Microstructural analysis was carried out with SEM (JEOL USA, Inc., Peabody, MA, USA). The dispersion of reinforcement particles in the matrix and the interface in the matrix / reinforcements were also analysed. Microhardness tests ($HV_{0.1}$) were conducted on polished and etched specimens. The measured microhardness values are given in Table 3 with an accuracy of ± 15 -20% for the two manufacturing operation techniques, alternately.

Table 3. Measurements of the microhardness values of the composites

Composition Name	Micro Hardness Values, HV _{0.1} (at interface only)
MENG (Sintering)	245± 20
MENG (Sinter+Forging)	290± 15

The density measurements of composite specimens using Archimedes method were performed. These density values changeable between 2.95 and 3.45 g/cm³ with ± 5% accuracy, respectively. Quasi-static compression tests (DIN 50106) were conducted using Zwick (Z250) mechanical test system at 1 mm/min strain rate. An average of 3-4 cylindrical specimens (Height/Diameter ≥ 1.5) were used for the test specimens produced by each manufacturing method. 3PB tests (ASTM D790) were also performed using the same mechanical test system. Low velocity impact (drop weight) tests were carried out with a drop tower (developed in SUPMECA/Paris Quartz Laboratories) to analyse the response of these composites designed with metal matrix to dynamic loading (Total weight 2.2 kg; Punch height 150 mm; Impact velocity~2.8 m/s).

Subsequently sintering and/or sinter + forging manufacturing processes, whole cylindrical specimens were tested for machinability at high cutting speed with low cutting force [6, 9, 16]. The purpose of this process is to remove damages on the surface of cylindrical specimens in cases such as work hardening or damage to the cutting tool.

Wear tests were performed by applying a normal load of 50 mN on a linear wear track of 500 µm and 1000 µm for 50 cycles and using the scratch ability of a nanoindenter. A cycle used during the tests was defined as the departure and the return on the same path. The wear tests were repeated a total of 10 times for each specimen, using a conical tip with a cone angle of 90° and at a speed of 50 µm/s (tip speed).

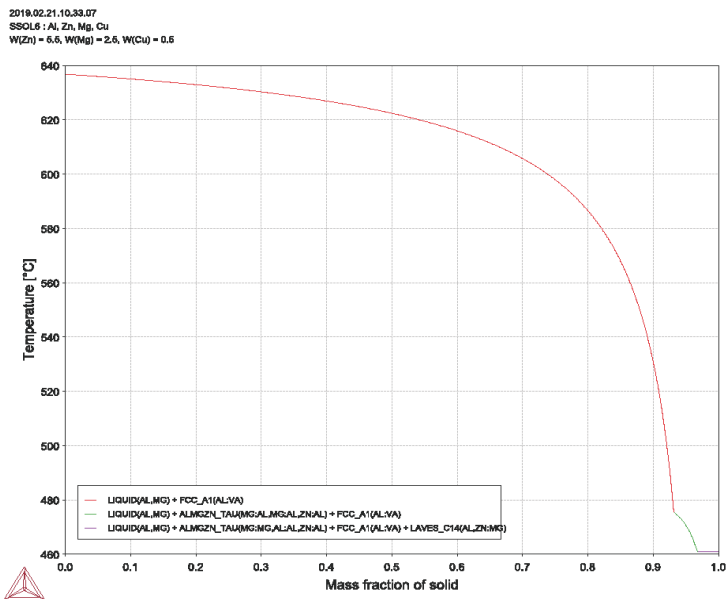
Creep tests were also conducted with a nano-indenter to analyze the time-dependent responses of the metal matrix composites prepared within the scope of the study. These tests with a Berkovich indenter used and 25 indents were created on a 5x5 grid in each test specimen. These formed indents were placed along the edges of the grid at intervals of 50 µm and 75 µm, and the load applied during the test was increased to a maximum load of 50 mN at a speed of 5 mN/s, keeping this load value for 500 s, and then unloaded. Immediately after this test process, the modulus and nano hardness values were calculated during the unloading phase of the creep test.

3. Results and Discussion

3.1. Comprehensive Microstructural Analysis

The result of Differential (Dynamic) Scanning Calorimetry (DSC) for Alumix-431, which is used as a component of the matrix to identify critical conversion points in the heating and cooling phase (in order to observe the relevant phases clearly, the heating and cooling rates were as low as possible, ~2°C/min, under inert N₂ atmosphere) within the scope of the study, is given in Figure 1. Furthermore, a general microstructural view for the sintered specimen is presented, however.

A relatively homogeneous dispersion of reinforcement elements in the matrix was observed, it was determined that a very tough structural relationship was formed between these interfaces due to a good chemical bond diffusion at the interfaces of the matrix-reinforcement elements.



(a)



(b)

Fig.1 (a) DSC diagram measured for AlumiX-431 and (b) SEM general microstructure for the sintered specimen

Figure 2 shows a microstructure taken from a sinter + forging specimen with “EDS” chemical analysis obtained on the “SEM” with BSE (Back Scattered) option. The reinforcement effect on the microstructure seems well and some of the areas show eutectic reaction due to chemical diffusion bonding. This is basically due to the easy diffusion of

copper in the matrix. It seems that the reinforcements added to the composite were effectively improving its toughening mechanism. It is advantageous to add copper and γ -alumina for these types of composites, mainly because it provides a good combination of ductility and strength, which is useful properties for industrial applications during the manufacture of complex components. Therefore, the combined process (Sinter + Forging) always gives hybrid composites a very stable and robust microstructure.

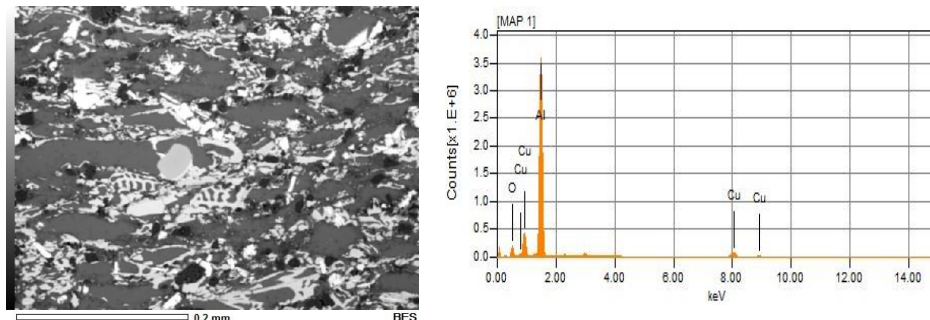


Fig. 2 Microstructure taken from a sinter + forging specimen with “EDS” chemical analysis obtained on the SEM with Back Scattered option

The distribution of the reinforcement elements in micro-sized very fine particles can be observed by "Mapping" analysis. As mentioned earlier on mapping analysis, it gives a safety observation of the homogeneity of the hybrid composite structure. The dispersion of reinforcement particles in the microstructure of the hybrid metal matrix composite for "MENG" produced with Sinter + Forging is given in Figure 3. Although the recycled chips used in the hybrid composite were atomized before the composite was prepared as a whole, the size of the chips varied between 10 and 200 μm . For this reason, the combined process called "sinter + forging" improves the dispersion of reinforcement particles within the final structure and increases the formation of a homogeneity and inner structure.

That is the reason we suggest this process especially for the recycled constituents as a low cost, alternative and more advantageous manufacturing process to design the composite [16-18].

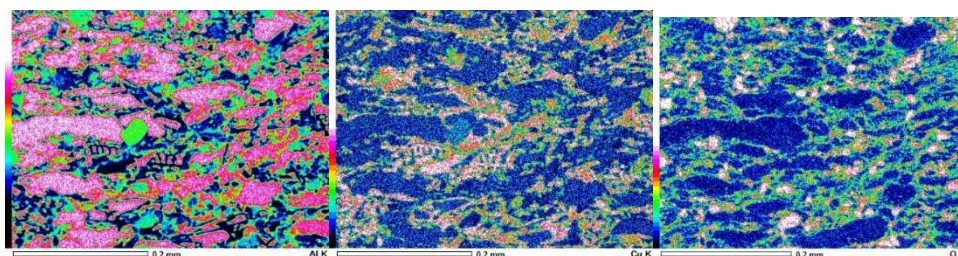


Fig. 3 Mapping elementary analyses of the hybrid metal matrix composite specimen (MENG, Sinter + Forging)

3.2. Quasi-Static Compression Test Results

In this research, quasi-static compression (DIN 50106) tests were performed under laboratory scales to evaluate the mechanical behaviour of these new hybrid metal matrix composites manufactured by sintering and sinter + forging manufacturing methods.

Quasi static compression test results of composite specimens obtained by sintering and sinter + forging manufacturing methods are shown in Figure 4. All quasi-static compression test results acquired for the combined method sinter + forging, were compared with the same type of test results obtained by the sintering process. These values obtained from the tests are demonstrated by taking the average values obtained from a minimum of 3 to 4 tests for each composite specimen. The standard deviation value in these experiments was determined to be at a variable value around ± 30 -45 MPa. When the values given in Figure 4 are examined, it is observed that the sinter + forging process provides higher resistance compared to a simple sintering process.

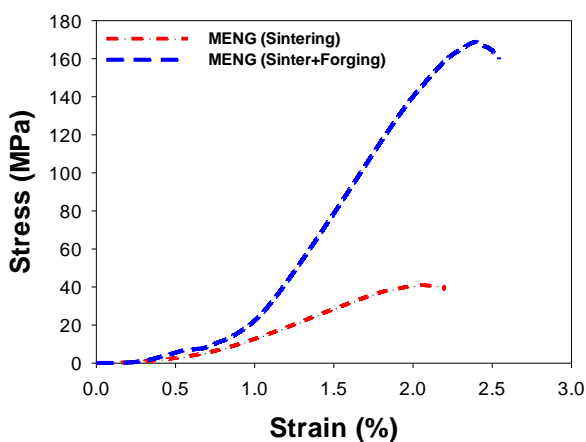


Fig. 4 Quasi-static compression test results for the sintered specimens and sinter + forging specimens

3.3. Three Point Bending (3PB) Test Results

As mentioned in the previous section of the study, these hybrid metal matrix composite parts were designed for connection / connector implementations in aerospace engineering, and for this reason, they were mainly studied in terms of bending forces under 3PB loading conditions. Figure 5 shows the 3PB (ASTM D 790) test results obtained for the sintered and sinter + forging specimens. All the other 3PB test results that were not presented here have indicated similar results with a variation of ± 20 - 30 MPa. All the tests have been realized under laboratory conditions and they are mean values obtained from the repeat of 3-4 tests for each composition. According to the data in Figure 5, the yield strength values of the test specimens were determined as 55.8205 MPa for the MENG (Sintering) specimen and 89.9069 MPa for the MENG (Sinter + Forging) specimen. Again, the sinter + forging composite showed high toughness behaviour.

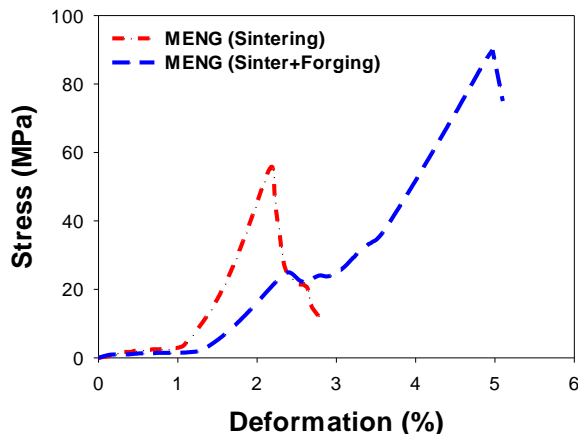


Fig. 5 “3PB” test results for the sintered specimens and sinter + forging specimens

3.4. Wear and Creep Test Results

For these tests, the creep compliance and the stress exponent were calculated by using data collection defined in Eq.1 [18]:

$$\varepsilon(t) = \sigma_0 J(t) \tag{1}$$

Where σ_0 is the constant stress applied and $J(t)$ is calculated using Eq.2

$$J(t) = A(t)/(1 - \nu)P_0 \tan \theta \tag{2}$$

Where; A(t) contact area; P_0 constant applied load; is expressed in Equation 2 where the effective cone angle is 70.3° for a Berkovich indentation and the Poisson ratio (ν) is 0.3.

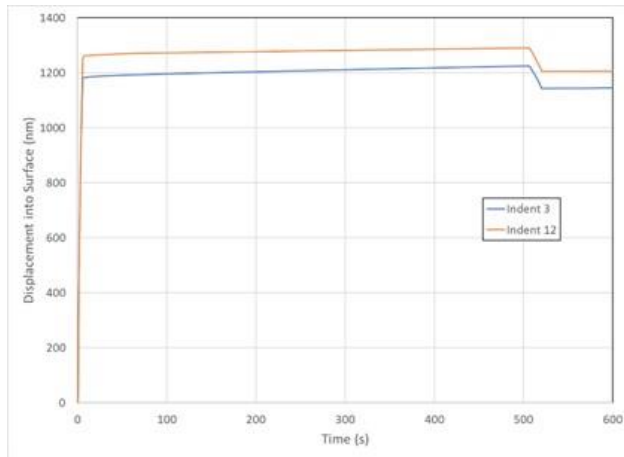
Thanks to this approach, it takes into account the change in the contact area under the Berkovich tip caused by displacement towards the surface.

The strain versus time behavior during creep is characterized by a high strain rate in the primary phase of creep. The secondary stage has a constant creep state given the strain rate given in Equation 3.

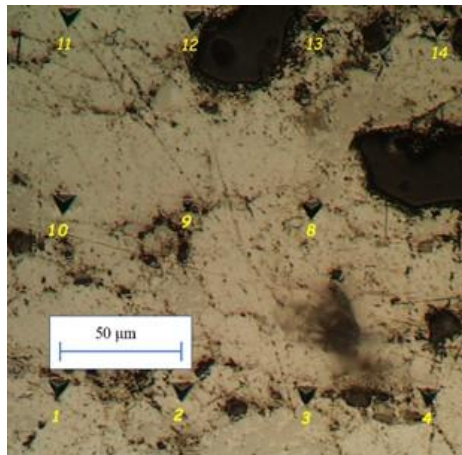
$$\dot{\varepsilon} = K \sigma^n \tag{3}$$

Where, K is constant and n is the stress exponent. The strain rate is calculated using software and n is obtained from a log-log plot of strain rate versus stress in the secondary phase of creep.

Although the materials investigated within the scope of the study were tried to be created in a homogeneous structure as much as possible, the microstructure was heterogeneous. It was observed that the nano-indentation test was performed on a small area / volume, causing a large scattering in the test result data. In order to come through this situation, the specimen number was taken as much as possible. Figure 6 shows the displacement time plots for indents 3 and 12 on the sinter + forging specimen. A picture of the indents was also presented in Fig 6. These curves are typical for the other indents on both sinter and sinter + forging specimens in which no significant creep was observed, and hence the creep exponents were not calculated.



(a)



(b)

Fig. 6 (a) Typical displacement into surface vs time curves during creep tests and (b) Micrograph of the indents

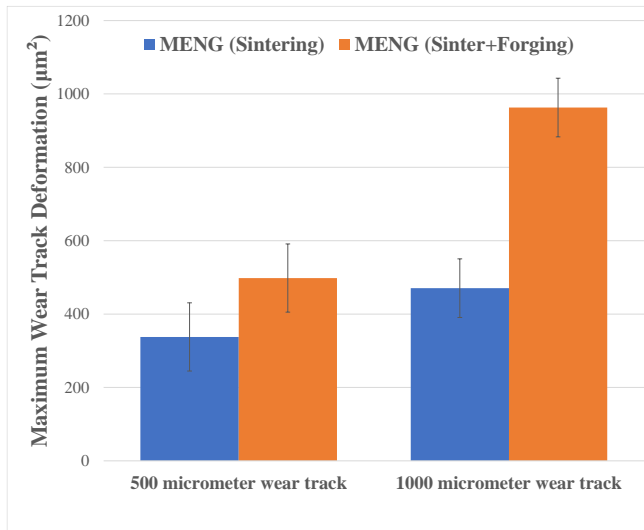
The modulus and hardness of the composites as measured during the unloading phase of the creep tests and their standard deviations are presented in Table 4.

Table 4. Modulus and hardness from unload data

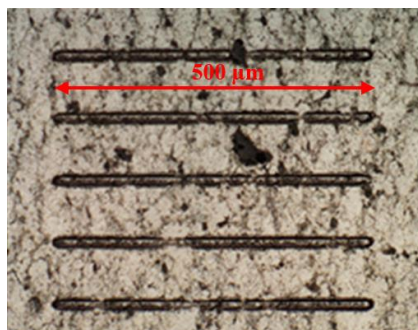
Composition Name	Modulus (GPa)	Hardness (GPa)
MENG (Sintering)	77.15 ± 14.69	1.81 ± 0.63
MENG (Sinter+Forging)	91.78 ± 11.79	1.81 ± 0.86

Figure 7 depicts the maximum wear track deformation measured as the area between the initial profile and the final (residual) profile of the wear track (using Berkovich TB10157). These are the means of the 10 wear tests for each type of manufacturing. The sinter +

forging specimens resulted to be more resistant to wear. Also shown in this figure are 5 of the wear tracks for a 500 μm long wear path for the sinter + forging specimens.



(a)



(b)

Fig. 7 (a) Maximum wear track deformation values obtained for the sintered and sinter + forging specimens and (b) Micrograph of 5 of the residual wear tracks for 500 μm wear tracks for the sinter + forging specimen

3.5. Low Velocity Impact Test Results

The results of the low velocity impact test for specimens manufactured by sintered and sinter + forging combined methods are shown in Figure 8. During the test, the reactive maximum forces on the hybrid metal matrix composite specimens were analyzed using the values obtained from both support data points. In this context, as circumstantiated in the section 2, a series of impact tests were performed by using a low velocity impact test (dynamic compression or instrumented drop weight test) device and applying instant force from the center (under room temperature) to the prepared cylindrical composite specimens through the impactor tip. The tests were repeated on three or four different specimens to determine the average values of the results obtained from the tests

performed to determine the low velocity impact behavior of the hybrid metal matrix composite composition.

First of all, the results obtained from the tests, the integrated effect of the sinter + forging process on the impact resistance of hybrid metal matrix composite specimens were evaluated (Fig. 8). These graphs given in Figure 8 express the higher impact force damping and / or absorption capacity of sinter+forging specimens than specimens manufactured by simple sintering process. This indicates that the impact resistance of the composite specimen is directly related to how much of the energy produced during the test can be absorbed. All specimens tested with the low velocity impact test under laboratory conditions show that most of the impact force is used to balance with the inertial force. Also, only an undersize fraction of the impact force is used to damage through deformation and / or cause the specimen to break. The energy absorbed by the composite specimen must be correlated with the production process used during the manufacturing of the specimens. In this respect, when the specimens were examined, the energy absorbed increases significantly in the specimens manufactured by the sinter + forging method. Since these results obtained from the tests are reached at laboratory scales, they need to be developed and improved with detailed analyzes for industrial applications [8, 16, 18].

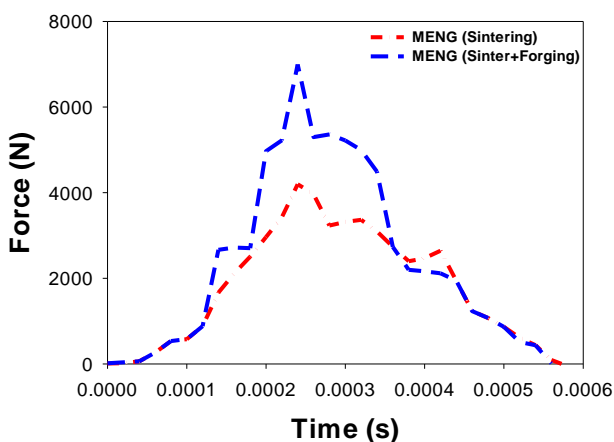


Fig. 8 Force (N)-Time (s) for the sintered specimens and for the sinter + forging specimens: Low velocity impact test results

4. Conclusions

A new hybrid metal matrix composite material (aluminum based) has been improved using fresh scrap aluminum with recycled Alumix-431 (50% wt) and AA1050 (50% wt) chips for aerospace / automotive connection components. These new hybrid composites have been successfully manufactured by both sintering and combined sinter + forging methods as low-cost manufacturing and necessary mechanical tests have been carried out. The addition of copper reinforcement together with γ -alumina can give a good combination of high ductility and high strength [5, 9, 13-18]. The sinter+forging process is a manufacturing process that is defined as a process of forming close to high accuracy for the manufacturing of parts processed from fresh scrap materials in the literature [6-14].

In the microstructural analysis, it was determined that the hybrid composite specimens manufactured by the sinter + forging combined process had a better chemical bonding diffusion at the matrix-reinforcement interface. In the microstructure of these composites, they showed a tough and complete microstructure feature that does not contain porosity.

The doping process and good powder mixture preparation conditions must definitely be improved in order to further improve the microstructure and further increase the wear resistance and ductility values. That is, a longer time of ball milling is required to contribute to a finer and more homogeneous dispersion of particles in the matrix.

In this current research, novel composite reinforced with γ -alumina and copper was designed for possible use in linkage/connector parts in such an aeronautical application [7, 11, 16]. This combined manufacturing process (Sinter + Forging) is considered to be a very safe approach for future studies of manufacturing alternative parts used in mechanical / electronic-like fastening components used in the aeronautical / automotive industry, as well as in other tribological applications. Optimization of operational parameters of production methods requires much more experimental research to make industrial scale real parts.

Acknowledgement

This work has been carried out at Supmeca/Paris-FRANCE Aeronautics Research Laboratory. Author acknowledge and appreciate so much Prof. Dr. E. BAYRAKTAR from Supmeca/Paris-FRANCE for valuable contributions and Dr. G. ZAMBELIS from Airbus-Helicopter-Paris/FR for supplying materials and for technical help.

References

- [1] Zhanga P, Zhanga L, Weib D, Wub P, Caob J, Shijiab C, Qua X. A high-performance copper-based brake pad for high-speed railway trains and its surface substance evolution and wear mechanism at high temperature. *Wear*, 2020; 444-445: 203182. <https://doi.org/10.1016/j.wear.2019.203182>
- [2] Enginsoy HM, Bayraktar E, Katundi D, Gatamorta F, Miskioglu I. Comprehensive analysis and manufacture of recycled aluminum based hybrid metal matrix composites through the combined method; sintering and sintering + forging, *Composites Part B: Engineering*, 2020; 194: 108040. <https://doi.org/10.1016/j.compositesb.2020.108040>
- [3] Rajkovic V, Bozic D, Stasic J, Wang H, Jovanovic MT. Processing, characterization and properties of copper-based composites strengthened by low amount of alumina particles. *Powder Technol.*, 2014; 268: 392-400. <https://doi.org/10.1016/j.powtec.2014.08.051>
- [4] Ferreira LFP, Bayraktar E, Robert MH, Miskioglu I. Particles reinforced scrap aluminum based composites by combined processing; sintering + thixoforming. *SEM, Mech. Composite Multi-funct. Mater.*, 2016; 7: 145-152. https://doi.org/10.1007/978-3-319-41766-0_17
- [5] Akdogan E, Tarakcilar AR, Topcu M, Yurtseven R. The effects of aluminium hydroxide and magnesium hydroxide on the mechanical properties of thermoplastic polyurethane materials. *Pamukkale University Journal of Eng. Sci.*, 2015; 21(8): 376-380. <https://doi.org/10.5505/pajes.2015.24572>
- [6] Kurşun A, Bayraktar E, Enginsoy HM. Experimental and numerical study of alumina reinforced aluminium matrix composites: Processing, microstructural aspects and properties. *Composites Part B: Engineering*, 2016; 90: 302-314. <https://doi.org/10.1016/j.compositesb.2016.01.006>
- [7] Zhang P, Zhang L, Wei DB, Wu PF, Cao JW, Shijia CR, Qu XH, Fu KX. Effect of graphite type on the contact plateaus and friction properties of copper-based friction material for high-speed railway train. *Wear*, 2019; 432-433: 202927. <https://doi.org/10.1016/j.wear.2019.202927>

- [8] Enginsoy HM, Gatamorta F, Bayraktar E, Robert MH, Miskioglu I. Numerical study of Al-Nb₂Al composites via associated procedure of powder metallurgy and thixoforming Composites Part B: Engineering, 2019; 162: 397-410. <https://doi.org/10.1016/j.compositesb.2018.12.138>
- [9] Ferreira LFP, Bayraktar E, Miskioglu I, Katundi D. Design of hybrid composites from scrap aluminium bronze chips. SEM, Mech. Composite Multi-funct. Mater., 2016; 15: 131-138. https://doi.org/10.1007/978-3-319-41766-0_15
- [10] Wagih A, Fathy A. Experimental investigation and FE simulation of nano-indentation on Al-Al₂O₃ nanocomposites. Adv. Powder Technolgy, 2016; 27 (2): 403-410. <https://doi.org/10.1016/j.appt.2016.01.021>
- [11] Ferreira LMP, Bayraktar E, Robert MH. Magnetic and electrical properties of aluminium matrix composite reinforced with magnetic nano iron oxide. Journal of Advances in Materials and Processing Technologies, 2016; 2 (1): 165-173. <https://doi.org/10.1080/2374068X.2016.1164529>
- [12] Fathy A, Shaker A, Hamid MA, Megahed AA. The effects of nano-silica/nanoalumina on fatigue behavior of glass fiber-reinforced epoxy composites. J. Compos. Mater., 2017; 51 (12): 1667-1679. <https://doi.org/10.1177/0021998316661870>
- [13] Bayraktar E, Ayari F, Tan MJ, Tosun Bayraktar A, Katundi D. Manufacturing of aluminum matrix composites reinforced with iron-oxide nanoparticles: microstructural and mechanical properties. Metallurgical and Materials Transactions B, 2014; 45B (26): 352-362. <https://doi.org/10.1007/s11663-013-9970-1>
- [14] Abd-Elwaheda MS, Meselh AF. Experimental investigation on the mechanical, structural and thermal properties of Cu-ZrO₂ nanocomposites hybridized by graphene nanoplatelets. Ceramics International, 2020; 46 (7): 9198-9206. <https://doi.org/10.1016/j.ceramint.2019.12.172>
- [15] Shehata F, Fathy A, Abdelhameed M, Moustafa SF. Preparation and properties of Al₂O₃ nanoparticle reinforced copper matrix composites by in situ processing. Mater. Design, 2009; 30 (7): 2756-2762. <https://doi.org/10.1016/j.matdes.2008.10.005>
- [16] Ferreira LFP, Bayraktar E, Robert MH, Miskioglu I. Particles reinforced scrap aluminium-based composites by combined processing sintering + thixoforming SEM, Mech. Composite Multi-funct. Mater., 2016; 17: 145-152. https://doi.org/10.1007/978-3-319-41766-0_17
- [17] Sadoun AM, Fathy A. Experimental study on tribological properties of Cu-Al₂O₃ nanocomposite hybridized by graphene nanoplatelets. Ceramic International, 2019; 45: 24784-24792. <https://doi.org/10.1016/j.ceramint.2019.08.220>
- [18] Katundi D, Ferreira LP, Bayraktar E, Miskioglu I, Robert MH. Design of magnetic aluminium (A356) based composites through combined method of sinter + forging SEM, Mech. Composite Multi-funct. Mater., 2017; 6: 89-101. https://doi.org/10.1007/978-3-319-63408-1_9



Mathematical modelling of drug release

Aykut Elmas^{*1,a}, Güliz Akyüz^{1,b}, Ayhan Bergal^{1,c}, Müberra Andaç^{1,2,d}, Ömer Andaç^{1,2,e}

¹Department of Nanoscience and Nanotechnology, Ondokuz Mayıs University, Samsun, Turkey

²Department of Chemistry, Ondokuz Mayıs University, Samsun, Turkey

Article Info

Abstract

Article history:

Received 22 Jan 2020

Revised 19 Mar 2020

Accepted 20 Mar 2020

Keywords:

Drug release;

Drug Delivery;

Mathematical Modelling;

Controlled Release

Mathematical models of the drug release have been used in the drug delivery (DD) field for more than 50 years by the scientists in the drug development process. These models not only help scientists to learn the dynamics of the drugs release, but also help them to save money and time by helping to design more effective experiments. There is no model in the literature that covers all drug release scenarios. Also, some system-specific models have complex mathematical equations and these models are not suitable for general use. Zero Order Model, First Order Model, Higuchi Model, Peppas Model and Hixon Crowell Model are used in 85% of drug release studies in total. The popularity of these models comes from their simplicity, easy mathematical expressions and implementation. In this review, mathematical derivations of these five models are shown in detail. The points to be considered during the derivation and the problems that may be encountered are carefully explained along with their solutions. In addition, the application of the models to drug release data and the points to be considered were obtained by writing from the scratch without using any ready software while obtaining the fit function. In this way, many problems are better understood, and their solutions are explained. Finally, the obtained fit functions are interpreted.

© 2020 MIM Research Group. All rights reserved.

1. Introduction

In the field of DD, deriving a mathematical model has been a challenging subject for scientists who want to predict drug release. A strong mathematical model can reduce the number of required experiments thanks to its prediction ability. And, these estimates prevent waste of time and money by helping to prepare more efficient experiments.

Up to date, there have been many attempts to describe drug release mathematically [1-4]. However, these models either failed to cover the entire DD area, or designed for very rare special systems and were not suitable for general use. Therefore, they cannot give accurate results, and some of them are too complex to apply to release data. In 1961, legendary professor Takeru Higuchi published his famous work on mathematical modelling of drug delivery [5]. And his equation becomes famous because it was theoretically stable, easy to apply, and has wide range of use which makes him called as a "father" of mathematical modelling of drug delivery. His surprisingly simple description of drug release from an ointment base was the beginning of the quantitative treatment of drug release. After Higuchi, there has been modifications of his model for describing porous systems and different geometries [1].

*Corresponding author: aykutdiamond@gmail.com

^aorcid.org/0000-0002-7721-4088; ^borcid.org/0000-0002-3522-9716; ^corcid.org/0000-0002-5930-9104;

^dorcid.org/0000-0001-7262-9762; ^eorcid.org/0000-0003-3641-9690

DOI: <http://dx.doi.org/10.17515/resm2020.178na0122>

Res. Eng. Struct. Mat. Vol. 6 Iss. 4 (2020) 327-350

A mathematical framework has been developed for studying to drug release from hydroxypropyl methyl cellulose (HPMC) tablets [6, 7]. A comprehensive model has been developed to describe dissolution and swelling behaviors from cylindrical HPMC tablets [8-10]. And an extension of this study has been developed for different coordinates [11-13]. This model was the most advanced one for the polymers undergoing erosion and swelling. For dissolving polymer system, first model has been developed in 1988 [14] and modified for macromolecular movements [15]. To overcome the blood-brain barrier, a finite element model was developed for central nervous system in 1997 [16]. Then, doxorubicin supported models developed for breast cancer [17]. Most of these models are based on the Fick's diffusion equation [18] and solutions for different variations [19]. Unfortunately, none of these models yield perfect solution. In drug delivery studies, there is no model covers all the problems. When developing a model, the following issues should be carefully considered.

- Only dominant features should be added to the model. Otherwise the equation would be too complex.
- Theory should be supported by the experiments.
- There is no mathematical theory that can be applied to all DD systems.
- Theory should be abandoned when it fails, even if it is compatible with the experiment.

The purpose of this article is to provide information about popular mathematical models. Since it is rarely encountered in the field of DD, the mathematics in deriving models is clearly explained and possible problems are shown with their solutions. Finally, it is shown that fitting procedure of the models into a release data. In the meantime, a program was written from scratch and the places that need attention are highlighted without using existing software. According to the work of Caccavo, some models are dominating the DD field [20]. They are, Zero Order model 18.9%, First Order model 15.6%, Higuchi model 19.4%, Peppas model 30% and Hixon-Crowell model 7.8% of usage frequency. It is also focused on these models in this work.

2. Derivation of the Models

For models that require long calculation, intermediate steps have been neglected. This neglect could mislead scientists because there may be some important points that guide calculations. Also jumping directly to the model result, makes harder to understand the theoretical concept of the model derivations.

The drug begins to dissolve in a special solvent such as water, blood, or gastric liquid. However, the dissolved molecules are not immediately dispersed into all the solvent called "bulk liquid". An imaginary layer occurs on the surface of the drug called "stagnant liquid". In sink conditions, concentration of the drug molecules is always considered zero for the simplification of the diffusion calculations. Because simplification assumes constant diffusion and gradient. The drug molecules will diffuse from higher concentration to the lesser concentration through stagnant liquid by the lead of Fick's law of diffusion [18].

$$J = -D_f \frac{dc}{dx} \quad (1)$$

Where J is the amount of substance passing perpendicularly through a unit surface area per time known as “flux”. D_f is the diffusion coefficient and dc/dx is the concentration gradient. The reason for the negative sign is, the gradient operator has the negative slope while concentration decreases with position. But the flux is a direction independent absolute quantity. Which means, there is flux or there is no flux. So, there shouldn't be a negative flux, that's why negative sign is added in the equation.

2.1. Zero Order Model

Zero Order model based on the reaction kinetics of the chemistry. According to these kinetics, speed of the reaction can be described as,

$$R = K_0[A]^0 \tag{2}$$

Where R is the reaction speed, $[A]^0$ represents the concentration of A which entering the reaction with zero degree, and K_0 is the zero order rate constant. Also, reaction speed can be written as,

$$R = -\frac{\Delta[A]}{\Delta t} \tag{3}$$

Where t is time. If reaction speed can be represented with two different equations, one can substitute equations (2) and (3).

$$\frac{d[A]}{dt} = -K_0$$

Or according to experimental conditions, one can write C in stead of $[A]$ to represent the concentration.

$$\frac{dC}{dt} = -K_0$$

Then, applying simple mathematics,

$$dC = -K_0 dt \quad \rightarrow \quad \int_{C_0}^{C_t} dC = -K_0 \int dt$$

$$(C) \Big|_{C_0}^{C_t} = -K_0 t \quad \rightarrow \quad C_t - C_0 = -K_0 t$$

$$C_t = C_0 - K_0 t \tag{4}$$

Here in eqn. (4) we have a linear representation of drug release as a Zero Order model. Advantages and disadvantages of this linearity will be discussed in experimental analysis part.

2.2. First Order Model

For the derivation of the First Order model, mathematical theory is same as the Zero Order model. Eqn. (3) remains same but eqn. (2) becomes first degree of concentration of substance A which enters the reaction.

$$R = K_1[A]^1 \tag{5}$$

Same as Zero Order model, one can substitute eqns. (3) and (5).

$$\frac{dC}{dt} = -K_1C \quad \rightarrow \quad \frac{dC}{C} = -K_1dt$$

$$\int_{C_0}^C \frac{1}{C} dC = -K_1 \int dt \quad \rightarrow \quad \ln(C) \Big|_{C_0}^C = -K_1t$$

$$\ln(C) - \ln(C_0) = -K_1t$$

$$\ln\left(\frac{C}{C_0}\right) = -K_1t \tag{6}$$

Here one should remember the rule which is $\log(x) = \ln(x)/\ln(10)$. So,

$$\ln(10) \log(x) = \ln(x) \tag{7}$$

By, substituting eqns. (6) and (7) one can get,

$$\ln(10) \log\left(\frac{C}{C_0}\right) = -K_1t \quad \rightarrow \quad \ln(10) = 2.303$$

$$\log\left(\frac{C}{C_0}\right) = \frac{-K_1t}{2.303} \quad \rightarrow \quad \log(C) - \log(C_0) = \frac{-K_1t}{2.303}$$

$$\log(C) = \log(C_0) - \frac{K_1t}{2.303} \tag{8}$$

Eqn. (8) can be considered the final representation of First Order model. This model also shows similarities with Zero Order model by linearity but thanks to logarithmic representation of the equation, there should be some important point to focus on while fitting procedure, which will be discussed in experimental analysis chapter.

2.3. Higuchi Model

Fifty years ago professor Takeru Higuchi created his famous equation that allows prediction of drug release from thin ointment films [5]. Before his derivation, he made some assumptions to overcome some problems. These assumptions should be taken into account otherwise it might cause misuse of the model.

- Transfer of the drug inside the ointment is slow, but inside the skin is fast. In these conditions one could observe stable diffusion.
- Skin acts like a perfect sink, which means the concentration of the drug is ignored. So, it is assumed the concentration in the skin is never increase.
- Concentration in the film is much more than the solubility of the drug at the ointment base.
- Drug separated to the ointment base uniformly and size of the drug particles much less than the ointment layer thickness.
- Speed of the drug solubility in the ointment base faster than the diffusion speed of the dissolved drug particles there. This assumption is important because diffused particle is immediately replaced by the new one.
- Diffusion coefficient in the ointment base is stable and not dependent neither time nor position of the layer.
- Edge effects are ignored. Skin surface area is much bigger than the thickness of the ointment film, so one can say the diffusion occurs in one dimension.
- Ointment base neither dissolves nor swells.

In the frame of these assumptions Higuchi made his derivations from graphic below (Figure 1).

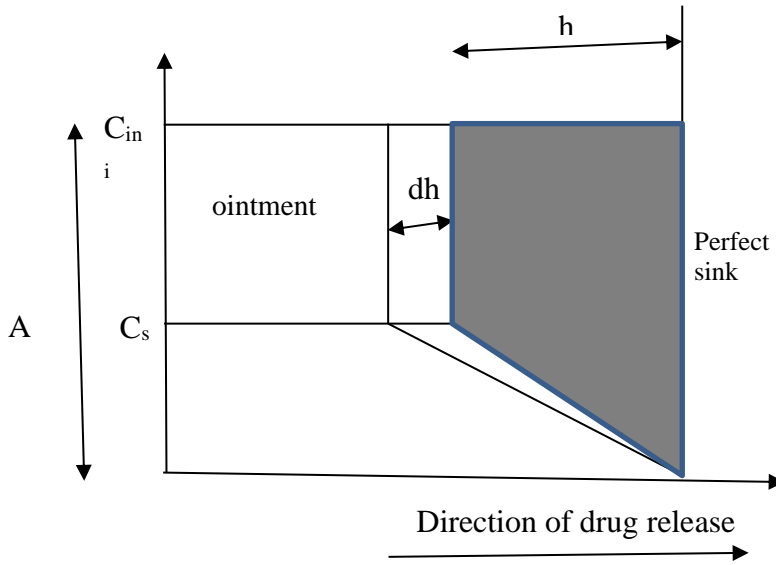


Fig. 1 Drug diffusion from ointment, where C_{ini} is the initial drug concentration, C_s is the drug solubility, horizontal axis is the diffusion direction of the molecules and the vertical axis is the drug concentration.

Here we can think that the perfect sink is the human skin and the grey area is soluted drugs membrane. If it is donated Q is the amount of absorbed at time t per unit area of exposure, and A is the concentration of drug expressed in units/cm³, surface area of the grey trapezoid in Figure 1 (right hand side of the eqn. (9)) corresponds to Q .

$$Q = h \left(A - \frac{C_s}{2} \right) \tag{9}$$

Here, h is an unknown parameter which should be fund. Rearranging Eqn. (9)

$$Q = h \left(A - \frac{C_s}{2} \right) \rightarrow Q = Ah - \frac{C_s}{2}h$$

$$dQ = Adh - \frac{1}{2}C_s dh \tag{10}$$

Also professor Higuchi foresaw that Fick's law [18] can be written as,

$$\frac{dQ}{dt} = DC_s/h \rightarrow dQ = D \frac{C_s}{h} dt \tag{11}$$

Where D is the diffusion constant. Substituting eqns. (10) and (11) we can get,

$$A dh - \frac{1}{2} C_s dh = D \frac{C_s}{h} dt$$

Dividing both sides by dt we get,

$$A \frac{dh}{dt} - \frac{1}{2} C_s \frac{dh}{dt} = \frac{D C_s}{h} \frac{dt}{dt} \rightarrow A \frac{dh}{dt} - \frac{1}{2} C_s \frac{dh}{dt} = \frac{D C_s}{h}$$

$$\frac{dh}{dt} \left(A - \frac{1}{2} C_s \right) = \frac{D C_s}{h} \rightarrow \frac{dh}{dt} \left(A - \frac{1}{2} C_s \right) h = D C_s$$

$$dh \left(A - \frac{1}{2} C_s \right) h = D C_s dt \rightarrow \frac{\left(A - \frac{1}{2} C_s \right)}{D C_s} h dh = dt$$

Both multiplying and dividing by 2 will simplify the calculations,

$$\frac{2 \left(A - \frac{1}{2} C_s \right)}{2 D C_s} h dh = dt \rightarrow \frac{(2A - C_s)}{2 D C_s} h dh = dt$$

$$\frac{(2A - C_s)}{2 D C_s} \int h dh = \int dt \rightarrow \frac{(2A - C_s)}{2 D C_s} \left(\frac{h^2}{2} \right) = t$$

$$\frac{(2A - C_s)}{4 D C_s} h^2 = t \rightarrow h^2 = \frac{4 D C_s t}{2A - C_s}$$

$$h = 2 \sqrt{\frac{D C_s t}{2A - C_s}} \tag{12}$$

Now, h can be represented by eqn (12). Substituting into Eqn. (9),

$$Q = Ah - \frac{C_s}{2} h \rightarrow Q = 2A \sqrt{\frac{D C_s t}{2A - C_s}} - \frac{C_s}{2} 2 \sqrt{\frac{D C_s t}{2A - C_s}}$$

$$Q = \sqrt{\frac{D C_s t}{2A - C_s}} (2A - C_s) \rightarrow Q = \sqrt{\frac{D C_s t (2A - C_s)^2}{(2A - C_s)}}$$

$$Q = \sqrt{D C_s t (2A - C_s)}$$

According to Higuchi, if $C_s \ll A$, then $(2A - C_s) \approx 2A$. So Q becomes

$$Q = \sqrt{2ADC_s t}$$

Here A, D and C_s are constant. If they merge into one single constant like k final equation becomes popular Higuchi model form as,

$$Q = k\sqrt{t} \tag{13}$$

As it seen from the Eqn. (13) Higuchi model is very simple equation. Zero Order and First Order models were linear representations of the drug release but, Higuchi model defines the release with square root of time which makes sense and strong relationship with the experiments.

2.4. Peppas Model

Peppas model also based on diffusion mechanics[19-21]. For the starting point, one may think the diffusion occurs in one dimension which is not real but simplifies the calculations. Figure 2

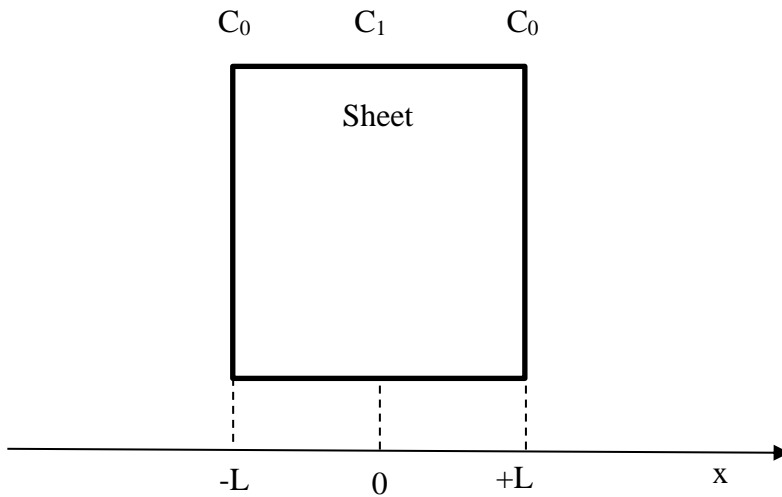


Fig. 2 Diffusion from a plane sheet. C, L and x represents concentration, length and direction respectively.

Defining boundary conditions as,

$$t = 0 \quad , \quad -L < x < L \quad , \quad C = C_{in} \tag{14}$$

$$t > 0 \quad , \quad x \leq L \quad , \quad C = C_0 \tag{15}$$

$$t \geq 0 \quad , \quad \frac{dC}{dx} = 0 \quad , \quad x = 0 \tag{16}$$

Where C_{in} represents the initial concentration and,

$$C_0 = C_{surface} - C_{ext} \tag{17}$$

Where C_0 is the concentration at $x=L$, $C_{surface}$ is the surface concentration of the plane sheet and C_{ext} is the external concentration. After defining boundary conditions, one may focus on the Fick's second diffusion equation [18].

$$\frac{dC}{dt} = D \frac{d^2C}{dx^2} \tag{18}$$

Where D is the diffusion constant. In the Eqn. (18) concentration is both function of time and position. This differential equation is called partial differential equation and could be solved by separation of variables technique as,

$$C(x, t) = C_x C_t \tag{19}$$

If it is substituted Eqn. (19) into Eqn. (18),

$$\frac{dC_t}{dt} C_x = D C_t \frac{d^2C_x}{dx^2}$$

Rearranged as,

$$\underbrace{\frac{1}{C_t} \frac{dC_t}{dt}}_{\text{only depends on } t} = \underbrace{\frac{D}{C_x} \frac{d^2C_x}{dx^2}}_{\text{only depends on } x} \tag{20}$$

Here in Eqn. (20) two different differential equations depending different variables equal each other. So, both equations should be equal same constant. That constant could be chosen anything. In this part it is chosen $-\lambda^2 D$ for the convenience of the further calculations. By focusing left hand side of the Eqn. (20)

$$\frac{1}{C_t} \frac{dC_t}{dt} = -\lambda^2 D \tag{21}$$

We get the first ordinary differential equation. And the right hand side of the Eqn. (20)

$$\frac{D}{C_x} \frac{d^2 C_x}{dx^2} = -\lambda^2 D \tag{22}$$

Becomes the second ordinary differential equation. Solutions of the Eqns. (21) and (22) are known well by the calculus. These solutions are,

$$C_t = Constant \times Exp(-\lambda^2 Dt) \tag{23}$$

$$C_x = A \times Sin(\lambda x) + B \times Cos(\lambda x) \tag{24}$$

Respectively. So the Eqn. (19) should be the multiplication of Eqns. (23) and (24).

$$C(x, t) = C_x C_t = Constant \times (ASin(\lambda x) + BCos(\lambda x))Exp(-\lambda^2 Dt) \tag{25}$$

For all states, general solution of Eqn. (25),

$$C = \sum_{n=0}^{\infty} (A_n Sin(\lambda_n x) + B_n Cos(\lambda_n x))Exp(-\lambda_n^2 Dt) \tag{26}$$

Eqn. (26) will be the general solution but there are three unknown parameters like A_n , B_n and λ_n . To find these parameters one should apply the boundary conditions. But first Eqn. (17) should be understood well. From the Figure 2 if $C_{surface}$ and $C_{external}$ are equal, $C_0 = C_{surf.} - C_{ext.}$ becomes zero. That is why there is no obstacle to write concentration like $C - C_0$ and C_0 is constant.

$$C - C_0 = \sum_{n=0}^{\infty} (A_n Sin(\lambda_n x) + B_n Cos(\lambda_n x))Exp(-\lambda_n^2 Dt) \tag{27}$$

Now, let's focus on the boundary conditions. According to Eqn. (16) while ≥ 0 , $dC/dx = 0$, at $x = 0$ mid plane. Taking derivative of Eqn. (27) according to x , at $x = 0$ one get,

$$\frac{dC}{dx} = 0 = \sum_{n=0}^{\infty} \underbrace{\lambda_n}_{constant} \left[\underbrace{A_n Cos(\lambda_n 0) + B_n Sin(\lambda_n 0)}_{=0} \right] \underbrace{Exp[-\lambda_n^2 Dt]}_{\neq 0, t \geq 0} \tag{28}$$

$$\underbrace{A_n}_{=0} \underbrace{Cos(0)}_{=1} + \underbrace{B_n}_{\neq 0} \underbrace{Sin(0)}_{=0} = 0 \rightarrow A_n = 0, B_n \neq 0$$

$$C - C_0 = \sum_{n=0}^{\infty} [B_n Cos(\lambda_n x)]Exp[-\lambda_n^2 Dt] \tag{29}$$

The parameter A_n has been known and B_n is not equal zero. To keep searching the parameters lets apply another boundary condition form Eqn. (15) as, $t > 0$, $x = \mp L$, $C = C_0 \rightarrow C - C_0 = 0$.

$$\begin{aligned}
 \text{at } x = L \quad \rightarrow \quad C - C_0 = 0 &= \sum_{n=0}^{\infty} \left[\underbrace{B_n \cos(\lambda_n L)}_{=0} \right] \underbrace{\text{Exp}[-\lambda_n^2 D t]}_{\neq 0, t > 0} \\
 \underbrace{B_n}_{\neq 0} \underbrace{\cos(\lambda_n L)}_{=0} = 0 &\quad \rightarrow \quad \cos(\lambda_n L) = 0 \quad \rightarrow \quad \lambda_n L = (2n + 1) \frac{\pi}{2} \\
 \lambda_n &= \frac{(2n + 1)\pi}{2L} \tag{30}
 \end{aligned}$$

By substituting Eqn. (30) into Eqn. (29) we get,

$$C - C_0 = \sum_{n=0}^{\infty} \left[B_n \cos\left(\frac{(2n + 1)\pi x}{2L}\right) \right] \text{Exp}\left[-\frac{(2n + 1)^2 \pi^2}{4L^2} t D\right] \tag{31}$$

With Eqn. (31) there is only one parameter remains unknown which is B_n . To find that parameter the first boundary condition could be applied in Eqn. (14). After applying the first boundary condition, exponential part of the Eqn. (31) equals 1. Considering the concentration as, $C = C_1$ we get,

$$C_1 - C_0 = \sum_{n=0}^{\infty} B_n \cos\left(\frac{(2n + 1)\pi x}{2L}\right) \tag{32}$$

To solve the Eqn. (32) superposition theorem should be applied. Both sides of the equation should be multiplied by $\cos\left(\frac{(2P + 1)\pi x}{2L}\right)$ and, should be integrated from $-L$ to L . P is an arbitrary parameter which will be eliminated in further steps of the calculations.

$$\begin{aligned}
 (C_1 - C_0) \int_{-L}^L \cos\left(\frac{(2P + 1)\pi x}{2L}\right) dx \\
 = \sum_{n=0}^{\infty} B_n \int_{-L}^L \cos\left(\frac{(2P + 1)\pi x}{2L}\right) \cos\left(\frac{(2n + 1)\pi x}{2L}\right) dx
 \end{aligned}$$

According to superposition theorem,

$$\int_{-L}^L \cos\left(\frac{(2P + 1)\pi x}{2L}\right) \cos\left(\frac{(2n + 1)\pi x}{2L}\right) dx = \begin{cases} 0 & , \quad P \neq n \\ L & , \quad P = n \end{cases}$$

Equality of zero will not be physical because it is known that there is a concentration of substance. So, it is chosen $P = n$.

$$(C_1 - C_0) \int_{-L}^L \cos\left(\frac{(2n+1)\pi x}{2L}\right) dx = \sum_{n=0}^{\infty} B_n L \tag{33}$$

To solve the Eqn. (33), change of variables technique is applied as,

$$U = \frac{(2n+1)\pi x}{2L} \quad , \quad dU = \frac{(2n+1)\pi}{2L} dx \quad , \quad dx = \frac{2L}{(2n+1)\pi} dU$$

$$x = -L \rightarrow U = -\frac{(2n+1)\pi}{2} \quad , \quad x = L \rightarrow U = \frac{(2n+1)\pi}{2}$$

Then the Eqn. (33) becomes,

$$(C_1 - C_0) \times \int_{-\frac{(2n+1)\pi}{2}}^{\frac{(2n+1)\pi}{2}} \cos(U) \times \frac{2L}{(2n+1)\pi} dU = \sum_{n=0}^{\infty} B_n L$$

Rearranging,

$$(C_1 - C_0) \times \frac{2L}{(2n+1)\pi} \int_{-\frac{(2n+1)\pi}{2}}^{\frac{(2n+1)\pi}{2}} \cos(U) dU = \sum_{n=0}^{\infty} B_n L$$

$$(C_1 - C_0) \times \frac{2L}{(2n+1)\pi} (\sin(U)) \Big|_{-\frac{(2n+1)\pi}{2}}^{\frac{(2n+1)\pi}{2}} = \sum_{n=0}^{\infty} B_n L$$

$$(C_1 - C_0) \times \frac{4L}{(2n+1)\pi} \sin\left(\frac{(2n+1)\pi}{2}\right) = \sum_{n=0}^{\infty} B_n L \tag{34}$$

To simplify the Eqn. (34) it is observed the behavior of the trigonometric part by assigning numbers for n .

$$\left. \begin{array}{l} n=0 \rightarrow \sin\left(\frac{(2n+1)\pi}{2}\right) = \sin\left(\frac{\pi}{2}\right) = 1 \\ n=1 \rightarrow \sin\left(\frac{3\pi}{2}\right) = -1 \\ n=2 \rightarrow 1 \\ n=3 \rightarrow -1 \end{array} \right\} = \begin{array}{l} 1 \quad \text{if } n = \text{even} \\ -1 \quad \text{if } n = \text{odd} \end{array}$$

Then,

$$\sin\left(\frac{(2n+1)\pi}{2}\right) = (-1)^n \tag{35}$$

Substituting Eqn. (35) into Eqn. (34) and canceling L 's from both side, B_n can be found as,

$$B_n = \frac{(C_1 - C_0)4(-1)^n}{(2n + 1)\pi} \tag{36}$$

Substituting Eqn. (36) into Eqn. (31),

$$C - C_0 = \sum_{n=0}^{\infty} \frac{(C_1 - C_0)4(-1)^n}{(2n + 1)\pi} \cos\left(\frac{(2n + 1)\pi x}{2L}\right) \exp\left[-\frac{(2n + 1)^2\pi^2}{4L^2}tD\right] \tag{37}$$

At time t amount of substance which is transferring inside or outside the sheet is M_t can be found by the integration of the flux ($flux = D \left|\frac{dC}{dx}\right|$) at the surface.

$$M_t = \int_0^t D \left|\frac{dC}{dx}\right|_{x=-L} dt + \int_0^t D \left|\frac{dC}{dx}\right|_{x=-L} dt = 2 \int_0^t D \left|\frac{dC}{dx}\right|_{x=\mp L} dt$$

Concentration C is known by Eqn. (37), M_t will be searched.

$$\begin{aligned} &\left|\frac{dC}{dx}\right| \\ &= \sum_{n=0}^{\infty} \frac{(C_1 - C_0)4(-1)^n}{(2n + 1)\pi} \left|\frac{(-1)(2n + 1)\pi}{2L} \sin\left(\frac{(2n + 1)\pi x}{2L}\right)\right| \exp\left[-\frac{(2n + 1)^2\pi^2}{4L^2}tD\right] \\ &\left|\frac{dC}{dx}\right|_{x=\mp L} = \frac{2(C_1 - C_0)}{L} \sum_{n=0}^{\infty} \underbrace{(-1)^n \sin\left(\frac{(2n + 1)\pi x}{2L}\right)}_{x=\mp L \rightarrow (-1)^n} \exp\left[-\frac{(2n + 1)^2\pi^2}{4L^2}tD\right] \\ M_t &= 2D \int_0^t \left|\frac{dC}{dx}\right|_{x=\mp L} dt \\ &= 2D \int_0^t \frac{2(C_1 - C_0)}{L} \sum_{n=0}^{\infty} (-1)^{2n} \exp\left[-\frac{(2n + 1)^2\pi^2}{4L^2}tD\right] \\ M_t &= \frac{4D(C_1 - C_0)}{L} \int_0^t \sum_{n=0}^{\infty} \exp\left[-\frac{(2n + 1)^2\pi^2 D t}{4L^2}\right] dt \end{aligned} \tag{38}$$

Integration in Eqn. (38) can be solved by change of variables technique as,

$$U = -\frac{(2n + 1)^2\pi^2 D t}{4L^2} , \quad dU = -\frac{(2n + 1)^2\pi^2 D}{4L^2} dt , \quad dt = -\frac{4L^2}{(2n + 1)^2\pi^2 D}$$

$$t = 0 \rightarrow U = -\frac{(2n + 1)^2\pi^2 D 0}{4L^2} = 0$$

$$t = t \rightarrow U = -\frac{(2n + 1)^2 \pi^2 Dt}{4L^2}$$

Substituting into Eqn. (38)

$$M_t = \frac{4D(C_1 - C_0)}{L} \int_0^{\frac{(2n+1)^2 \pi^2 Dt}{4L^2}} \text{Exp}[U] \times \frac{-4L^2}{(2n + 1)^2 \pi^2 D} dU$$

Rearranging,

$$M_t = \frac{4D(C_1 - C_0)(-4L^2)}{L(2n + 1)^2 \pi^2 D} \int_0^{\frac{(2n+1)^2 \pi^2 Dt}{4L^2}} \text{Exp}[U] dU$$

$$M_t = \frac{4(C_1 - C_0)(-4)L}{(2n + 1)^2 \pi^2} (\text{Exp}(U)) \Big|_0^{\frac{(2n+1)^2 \pi^2 Dt}{4L^2}}$$

$$M_t = -\frac{16(C_1 - C_0)L}{(2n + 1)^2 \pi^2} \left[\text{Exp}\left(-\frac{(2n + 1)^2 \pi^2 Dt}{4L^2}\right) - 1 \right]$$

$$M_t = \frac{16(C_1 - C_0)L}{\pi^2} \sum_{n=0}^{\infty} \frac{1}{(2n + 1)^2} \left[1 - \text{Exp}\left(-\frac{(2n + 1)^2 \pi^2 Dt}{4L^2}\right) \right] \tag{39}$$

For the infinite time the amount of substance entered or left the sheet can be defined as [21],

$$M_\infty = 2|C_1 - C_0|L \tag{40}$$

And the total amount of diffusing substance which has entered or left the sheet of thickness 2L (from -L to L) at time t, M_t is expressed as a fraction of the corresponding quantity after infinite time M_∞ as,

$$\frac{M_t}{M_\infty} \tag{41}$$

Then substituting Eqns. (39) and (40) into Eqn. (41) we get,

$$\frac{M_t}{M_\infty} = \frac{\frac{16(C_1 - C_0)L}{\pi^2} \sum_{n=0}^{\infty} \frac{1}{(2n+1)^2} \left[1 - \text{Exp}\left(-\frac{(2n+1)^2 \pi^2 Dt}{4L^2}\right) \right]}{2|C_1 - C_0|L}$$

$$\frac{M_t}{M_\infty} = \frac{8}{\pi^2} \sum_{n=0}^{\infty} \frac{1}{(2n+1)^2} \left[1 - \text{Exp} \left(-\frac{(2n+1)^2 \pi^2 Dt}{4L^2} \right) \right]$$

$$\frac{M_t}{M_\infty} = \frac{8}{\pi^2} \left[\sum_{n=0}^{\infty} \frac{1}{(2n+1)^2} - \sum_{n=0}^{\infty} \frac{1}{(2n+1)^2} \text{Exp} \left[-\frac{(2n+1)^2 \pi^2 Dt}{4L^2} \right] \right]$$

From the series rule,

$$\sum_{n=0}^{\infty} \frac{1}{(2n+1)^2} = \frac{\pi^2}{8}$$

Then,

$$\frac{M_t}{M_\infty} = \frac{8}{\pi^2} \left[\frac{\pi^2}{8} - \sum_{n=0}^{\infty} \frac{1}{(2n+1)^2} \text{Exp} \left[-\frac{(2n+1)^2 \pi^2 Dt}{4L^2} \right] \right]$$

Rearranging

$$\frac{M_t}{M_\infty} = \frac{8\pi^2}{\pi^2 8} - \frac{8}{\pi^2} \sum_{n=0}^{\infty} \frac{1}{(2n+1)^2} \text{Exp} \left[-\frac{(2n+1)^2 \pi^2 Dt}{4L^2} \right]$$

$$\frac{M_t}{M_\infty} = 1 - \sum_{n=0}^{\infty} \frac{8}{(2n+1)^2 \pi^2} \text{Exp} \left[-\frac{(2n+1)^2 \pi^2 Dt}{4L^2} \right] \tag{42}$$

For the alternating solution Laplace transformation will result [21]

$$\frac{M_t}{M_\infty} = 4 \left[\frac{Dt}{l^2} \right]^{1/2} \left[\frac{1}{\pi^2} + 2 \sum_{n=1}^{\infty} (-1)^n \text{ierfc} \frac{nl}{2\sqrt{Dt}} \right] \tag{43}$$

For the small times short time behavior sum part, has no effect to the summation after first few terms. So $\sum \approx 1/\sqrt{\pi}$.

$$\frac{M_t}{M_\infty} = 4 \left[\frac{Dt}{\pi l^2} \right]^{1/2} \tag{44}$$

In Eqn. (44), constants D , π , and l can be collected under a new constant k .

$$\frac{M_t}{M_\infty} = kt^{1/2} \tag{45}$$

For a second limiting case, according to kinetics of zero order, the drug release rate is independent of time. Such situation is described by a general equation of the form

$$\frac{M_t}{M_\infty} = kt \tag{46}$$

Most of the release falls between the Eqns. (45) and (46). So, both equations could be summed.

$$\frac{M_t}{M_\infty} = k_1\sqrt{t} + k_2t \tag{47}$$

Eqn. (47) can be generalized as,

$$\frac{M_t}{M_\infty} = kt^n \tag{48}$$

Eqn. (48) is the Peppas model which is very similar to the Higuchi model. One should focus on the exponential part of the time which is not constant. Fitting model to the experimental data with variable data will be slightly different from the routine process. Which will be discussed in further chapters.

2.5. Hixon Crowell Model

Hixon Crowell model is another popular model in the field [22]. It is not as popular as Higuchi and Peppas model but, considering its derivation, it is worth to mention. In Hixon Crowell model the basic concept can be specified as,

$$\underbrace{\frac{dC(t)}{dt}}_{\substack{\text{rate of} \\ \text{concentration} \\ \text{change}}} = k(C_s - C(t)) \tag{49}$$

Where $C(t)$ is the concentration depends on time, k is constant, C_s is the concentration of the saturated solution. Rate of change of weight described as,

$$\frac{dw}{dt} = k_2S(C_s - C) \tag{50}$$

Where w, k_2 and S are wieght, constant and surface of substance at time t respectively. If weight of the substance dissolved at timet,

$$w_0 - w \tag{51}$$

Then the mass in a specific volume is,

$$\frac{(w_0 - w)}{V} = C \tag{52}$$

Where V is volume, and,

$$\frac{w_s}{V} = C_s \tag{53}$$

If Eqns. (52) and (53) substituted into Eqn. (50)

$$\frac{dw}{dt} = -k_2 S \left(\frac{w_s}{V} - \frac{w_0 - w}{V} \right) \rightarrow V \left(\frac{dw}{dt} \right) = -k_2 S (w_s - w_0 + w) \tag{54}$$

Surface varies 2/3 power of its volume.

$$S = V^{2/3} \quad , \quad V = \frac{w}{d} \quad \rightarrow \quad S = \frac{1}{\underbrace{d^{2/3}}_k} w^{2/3} \tag{55}$$

Where d is density and k is constant which represents density. Then S is substituted into Eqn. (54).

$$V \left(\frac{dw}{dt} \right) = -k_2 k w^{2/3} (w_s - w_0 + w) \tag{56}$$

Collecting constants k_2 and k into a new constant as k_1 , defining $w_s - w_0 = g$ and rearranging Eqn. (56)

$$V \left(\frac{dw}{dt} \right) = -k_1 w^{2/3} (g + w) \rightarrow V \left(\frac{dw}{dt} \right) = -k_1 (g w^{2/3} + w^{5/3})$$

$$V \times \frac{1}{(g w^{2/3} + w^{5/3})} dw = -k_1 dt$$

Integrating both parts

$$V \int \frac{1}{(g w^{2/3} + w^{5/3})} dw = -k_1 \int dt$$

$$g^{1/3} = a \quad , \quad w_0^{1/3} = b \quad , \quad w^{1/3} = x \quad , \quad w = x^3 \quad , \quad dw = 3x^2 dx$$

$$V \int \frac{3x^2}{(a^3 x^2 + x^5)} dx = \frac{V \left(2\sqrt{3} \tan^{-1} \left[\frac{(-a+2x)}{\sqrt{3}a} \right] + 2 \ln[a+x] - \ln[a^2 - ax + x^2] \right)}{2a^2}$$

$$a = g^{1/3} \rightarrow g = (w_s - w_0) \quad , \quad x = w^{1/3}$$

While concentration change of a substance is negligible. So C is constant then $C_s - C$ is constant. The rate is proportional to the surface alone, which is,

$$\frac{dw}{dt} = -k_3 w^{2/3} \tag{57}$$

Integrating both parts,

$$\int_0^t \frac{1}{w^{2/3}} dw = -k_3 \int dt \rightarrow w_0^{1/3} - w^{1/3} = k_4 t \tag{58}$$

Eqn. (58) could be considered as Hixon Crowell model [22].

3. Experimental Analysis

For the experimental analysis part, public data table “Cumulative % drug release data of all the formulations” [23] is used from the work of Madhavi [24], under the creative commons license by, CC BY-NC-SA 3.0 [25]. The work corresponds the dissolution enhancement of efavirenz by solid dispersion and PEGylation techniques. In related work, PEGylated compound 2 is released with time by (5,10,15,20,25,30,45,60,80,100) minutes with (17,22,32,34,39,42,48,50,54,57) percentage which is sufficient for fitting and testing the models.

For the simplicity and linearity of the Zero Order model as seen in Eqn. (4), the fit of it does not require modification of axes to get a suitable representation. All the data collected in a suitable matrix and fitted to the function. In this article the Wolfram Mathematica 10 software is used to perform fitting, graphing and strength test.

For the Zero Order model it could be observed that fit does not look good enough because of the fit function is missing most of the data points. But when it is coming to compare many models visual comments might start debate. To test the strength of the models quantitatively it is chosen Watson’s U Square Method [26] because of the convenience of the data set. This test yields two results. One statistic and other P-Value. For the perfect fit statistic value should be equal to zero and P-Value should be equal to one. Then it could be commented on the strength test results comparison. Which model is strong or weak and which model is better? For the Figure 3 fit results, strength test yield statistic 0.0605 and P-Value 0.615658.

Fitting the First Order model is slightly different from the Zero Order model, because of the model functions logarithmic nature as seen in Eqn. (8). For this kind of equation, it is not possible to draw a graph as drug release versus time, because the function represents logarithm of the remaining drug. To overcome this axes problem, data matrix should be converted to the suitable form by first, converting release data into remaining data. Second, convert it into a logarithmic value. Then, fitting the function will be possible.

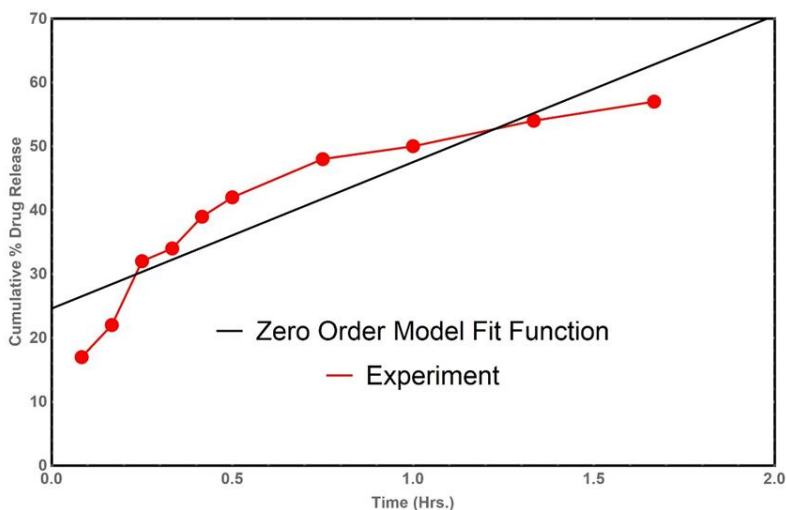


Fig. 3 Fit of Zero Order model function to the drug release data.

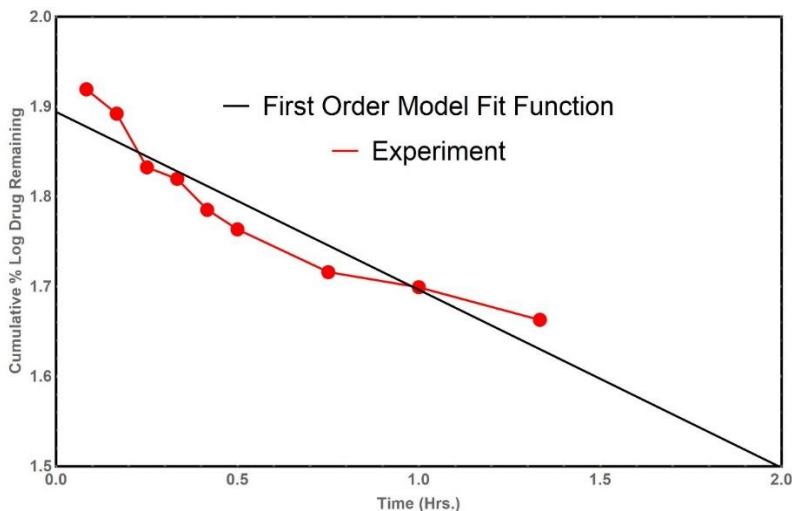


Fig. 4 Fit of First Order model function to the drug release data.

As seen from the Figure 4, vertical axes is different from the Figure 3. And function behaves linear with negative slope thanks to nature of the function. Strength test results as statistic 0.403509 and P-Value 0.000565739.

As it seen, every model needs specific data set arrangements for fitting. For Higuchi model, drug release remains same but time varies with the power of $\frac{1}{2}$ so it will not appropriate to use same horizontal axes with Zero and First Order models. Time part of the data matrix also should be converted into suitable form by adding the power of $\frac{1}{2}$ to it as,

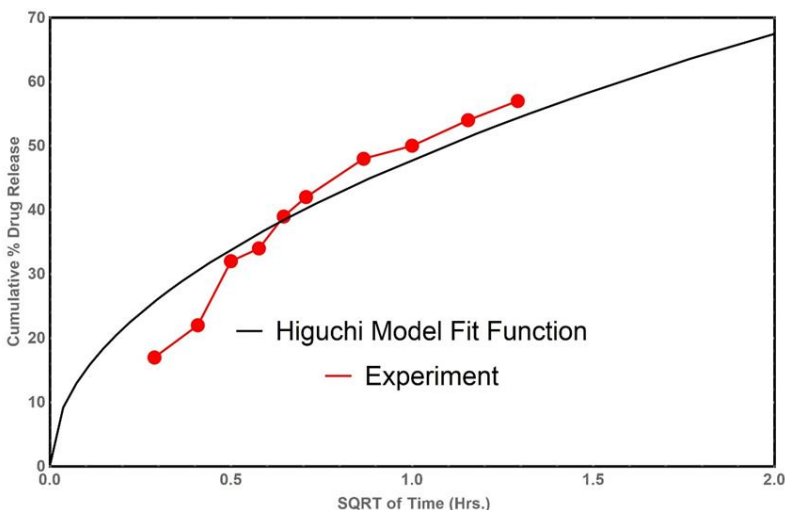


Fig. 5 Fit of Higuchi model function to the drug release data.

As it seen from the Figure 5 vertical axis is similar with the Zero Order model, but horizontal axis is converted into Higuchi form. Higuchi Eqn. (13) predicts fast diffusion for short term first, then release starts to get slower with time thanks to the $\frac{1}{2}$ power of time. That makes sense for most diffusion-based release, and that is why it stands one of the strongest and popular model of all time. For the fit in Figure 5, Higuchi model strength test results 0.0445 for statistic and 0.808438 for P-Value.

In Peppas model time varies with the power of a parameter n as seen in Eqn. (48). In this case it will not be possible to generate graph for an unknown axis. But fitting procedure still will generate the parameters. So, data matrix could be converted into Peppas form with the unknown parameter n than fitting is applied. In that way software will generate the most possible parameters for both k and n values which makes it possible to visualize.

As seen from the Figure 6 fit function gets close to the dataset and horizontal axes is converted into the Peppas form with the generated parameter. Strength test of the Peppas model yields, statistic 0.033 and P-Value 0.933232.

For another popular model Hixon Crowell model to arranging data matrix is follows the same procedure. As seen in Eqn. (58) function represents difference between cube roots of the initial amount and remaining amount. Applying this difference into the data matrix, it easily could be getting the vertical axes.

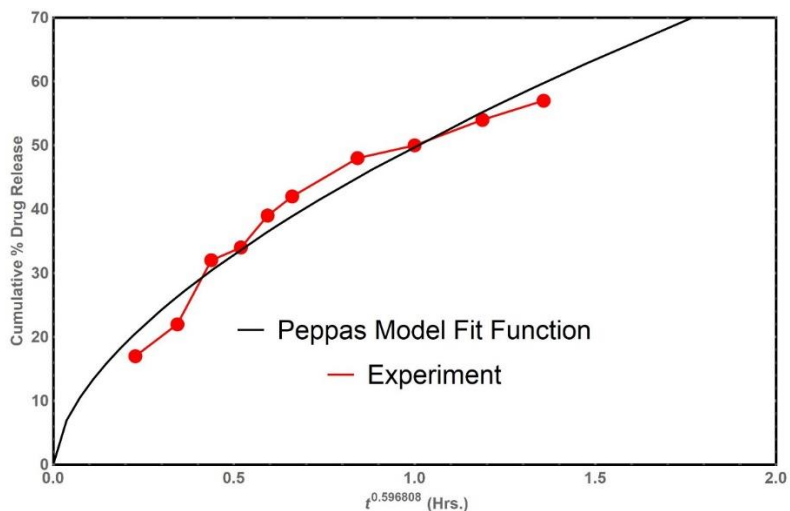


Fig. 6 Fit of Peppas model function to the drug release data.

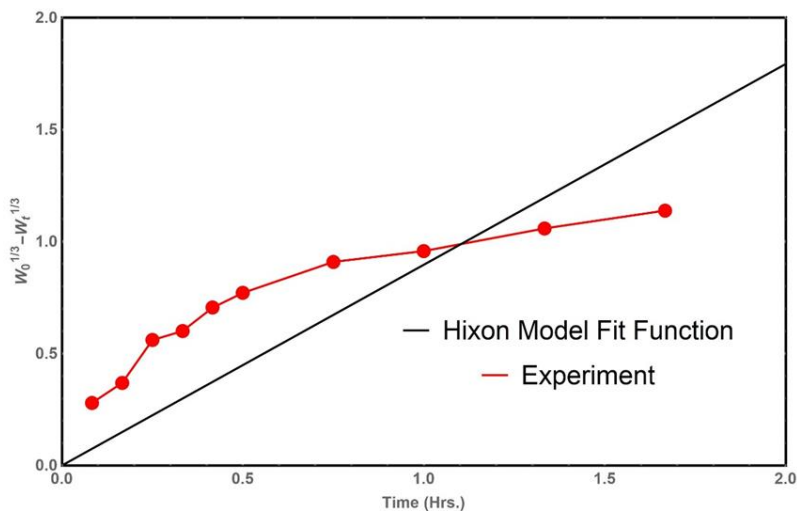


Fig. 7 Fit of Hixon Crowell model function to the drug release data.

It could easily be observed that the vertical axis has transformed the model suitable form from the Figure 7. Strength test of Hixon Crowell model results the statistic 0.425 and P-Value 0.00039154 which is far from a good fit because the model function is stacked to the origin.

Table 1 Model fit parameters.

Models	Parameters		
	C	K	n
Zero Order Model	24.5908	22.9373	-
First Order Model	78.3375	0.4555	-
Higuchi Model	-	47.8268	-
Peppas Model	-	49.8155	0.5968
Hixon Crowell Model	-	0.8965	-

Table 2 Comparison of the strength of the fits.

Models	Statistic	P-Value
Zero Order Model	0.060500	0.615658
First Order Model	0.403509	0.000565
Higuchi Model	0.044500	0.808438
Peppas Model	0.033000	0.933232
Hixon Crowell Model	0.425000	0.000391

As seen from the

Table 2, Higuchi and Peppas models are able to generate strong fits to the drug release data.

Finally it is seen from the experimental analysis, Zero Order model and First Order model can be applied for the 50% of the drug release approximately for the related data. However Higuchi and Peppas model can generate fit function up to 60% of drug release which is end of the release data. But the curvature of the fit functions foreseen that, the function is able to produce higher percentage representation. Also Hixon model is not as good as Higuchi and Peppas model because of its origin dependent nature. This behavior of the models is obviously occurred by the experimental details. In the related data set, drug is released up to 57%. In many experiments sink conditions is not satisfied and due to the saturation drug release is slowed, or in some scenarios there are some drug carriers that prevents the fast release. All the related parameters should be added into the models carefully if needed

4. Conclusions

In the DD field, there is no comprehensive resource describing the derivation of mathematical models explicitly. Existing works either focus on single model or jump into direct result of model functions. The purpose of this review is showing explicit derivation of the most popular models and collecting them under one single paper. At the same time, the problems encountered during calculation and fitting are also discussed in detail. These problems are not clarified in the literature.

The first of the two major problems is choosing the correct expression for release when applying boundary conditions (Eqn. (27)). There is no guide in the literature to the selecting boundary conditions correctly and to obtain parameters. This study might fill that gap by the explicit applications of the boundaries without non-dimensionalization. Second problem is the representation of the fitting functions in proper axes. In most of the studies, fitting is represented by build-in ready computer software and the obtained results are shown directly. Almost every specialist uses that way because it is faster and easier. But

there is still no guide to align the axes for the relevant model. This review also overcome that problem (Figure 4-Figure 7))

As a result, in this study it is focused on guiding the new researchers who interests to understand drug delivery mechanism by collecting all necessary subjects under one single source. Derivation, calculation, application and testing of the models have been explained carefully which might help scientists to take their works further in related area. Also, it is underlined the importance of the models that give predictions to the scientists for preventing waste of time and money for their experiments. In the future it will be focused on the relation between the reaction rate constant and activation energy by Arrhenius equation, which leads to the calculations to the thermodynamic studies. Thus, it is planned to investigate whether there is a relationship between entropy and enthalpy and the activation energy of the reaction.

Conflict of interest

The authors declare that they have no known competing financial interests or personal relationships that could have appeared to influence the work reported in this paper.

Acknowledgement

The authors acknowledge that this study is supported by BAP research project in the University of Ondokuz Mayıs (Project Number: PYO.FEN.1901.18.008).

References

- [1] Siepmann J, Peppas NA. Modeling of drug release from delivery systems based on hydroxypropyl methylcellulose (HPMC). *Advanced Drug Delivery Reviews*, 2001; 48:2-3 139-157. [https://doi.org/10.1016/S0169-409X\(01\)00112-0](https://doi.org/10.1016/S0169-409X(01)00112-0)
- [2] Siepmann J, Gopferich A. Mathematical modeling of bioerodible, polymeric drug delivery systems. *Advanced Drug Delivery Reviews*, 2001; 48:2-3 229-247. [https://doi.org/10.1016/S0169-409X\(01\)00116-8](https://doi.org/10.1016/S0169-409X(01)00116-8)
- [3] Arifin DY, Lee LY, Wang CH. Mathematical modeling and simulation of drug release from microspheres: Implications to drug delivery systems. *Advanced Drug Delivery Reviews*, 2006; 58:12-13 1274-1325. <https://doi.org/10.1016/j.addr.2006.09.007>
- [4] Lin CC, Metters AT. Hydrogels in controlled release formulations: Network design and mathematical modeling. *Advanced Drug Delivery Reviews*, 2006; 58:12-13 1379-1408. <https://doi.org/10.1016/j.addr.2006.09.004>
- [5] Brochmann-Hanssen E, Higuchi T. *Pharmaceutical analysis*, Interscience Publishers, New York,, 1961.
- [6] Grassi M, Voinovich D, Moneghini M, Franceschinis E, Perissutti B, Filipovic-Grcic J. Preparation and evaluation of a melt pelletised paracetamol/stearic acid sustained release delivery system. *Journal of Controlled Release*, 2003; 88:3 381-391. [https://doi.org/10.1016/S0168-3659\(03\)00011-7](https://doi.org/10.1016/S0168-3659(03)00011-7)
- [7] Grassi M, Zema L, Sangalli ME, Maroni A, Giordano F, Gazzaniga A. Modeling of drug release from partially coated matrices made of a high viscosity HPMC. *International Journal of Pharmaceutics*, 2004; 276:1-2 107-114. <https://doi.org/10.1016/j.ijpharm.2004.02.016>
- [8] Ju RT, Nixon PR, Patel MV. Drug-Release from Hydrophilic Matrices .1. New Scaling Laws for Predicting Polymer and Drug-Release Based on the Polymer Disentanglement Concentration and the Diffusion Layer. *Journal of Pharmaceutical Sciences*, 1995; 84:12 1455-1463. <https://doi.org/10.1002/jps.2600841213>
- [9] Ju RT, Nixon PR, Patel MV, Tong DM. Drug-Release from Hydrophilic Matrices .2. A Mathematical-Model Based on the Polymer Disentanglement Concentration and the

- Diffusion Layer. Journal of Pharmaceutical Sciences, 1995; 84:12 1464-1477. <https://doi.org/10.1002/jps.2600841214>
- [10] Ju RT, Nixon PR, Patel MV. Diffusion coefficients of polymer chains in the diffusion layer adjacent to a swollen hydrophilic matrix. Journal of Pharmaceutical Sciences, 1997; 86:11 1293-1298. <https://doi.org/10.1021/js970053n>
- [11] Siepmann J, Podual K, Sriwongjanya M, Peppas NA, Bodmeier R. A new model describing the swelling and drug release kinetics from hydroxypropyl methylcellulose tablets. Journal of Pharmaceutical Sciences, 1999; 88:1 65-72. <https://doi.org/10.1021/js9802291>
- [12] Siepmann J, Peppas NA. Hydrophilic matrices for controlled drug delivery: an improved mathematical model to predict the resulting drug release kinetics (the "sequential layer" model). Pharm Res, 2000; 17:10 1290-8.
- [13] Siepmann J, Kranz H, Peppas NA, Bodmeier R. Calculation of the required size and shape of hydroxypropyl methylcellulose matrices to achieve desired drug release profiles. International Journal of Pharmaceutics, 2000; 201:2 151-64. [https://doi.org/10.1016/S0378-5173\(00\)00390-2](https://doi.org/10.1016/S0378-5173(00)00390-2)
- [14] Harland RS, Gazzaniga A, Sangalli ME, Colombo P, Peppas NA. Drug/polymer matrix swelling and dissolution. Pharm Res, 1988; 5:8 488-94. <https://doi.org/10.1023/A:1015913207052>
- [15] Narasimhan B, Peppas NA. Molecular analysis of drug delivery systems controlled by dissolution of the polymer carrier. J Pharm Sci, 1997; 86:3 297-304. <https://doi.org/10.1021/js960372z>
- [16] Kalyanasundaram S, Calhoun VD, Leong KW. A finite element model for predicting the distribution of drugs delivered intracranially to the brain. Am J Physiol, 1997; 273:5 R1810-21. <https://doi.org/10.1152/ajpregu.1997.273.5.R1810>
- [17] Lankelma J, Fernández Luque R, Dekker H, Schinkel W, Pinedo HM. A mathematical model of drug transport in human breast cancer. Microvasc Res, 2000; 59:1 149-61. <https://doi.org/10.1006/mvre.1999.2218>
- [18] Fick A. On Liquid Diffusion (Reprinted from the London, Edinburgh, and Dublin Philosophical Magazine and Journal of Science, Vol 10, Pg 30, 1855). Journal of Membrane Science, 1995; 100:1 33-38. <https://doi.org/10.1080/14786445508641925>
- [19] Crank J. The mathematics of diffusion / by J. Crank, Clarendon Press, Oxford [England], 1975.
- [20] Caccavo D. An overview on the mathematical modeling of hydrogels' behavior for drug delivery systems. International Journal of Pharmaceutics, 2019; 560:175-190. <https://doi.org/10.1016/j.ijpharm.2019.01.076>
- [21] Ritger PL, Peppas NA. Transport of Penetrants in the Macromolecular Structure of Coals .7. Transport in Thin Coal Sections. Fuel, 1987; 66:10 1379-1388. [https://doi.org/10.1016/0016-2361\(87\)90185-2](https://doi.org/10.1016/0016-2361(87)90185-2)
- [22] Hixson AW, Crowell JH. Dependence of Reaction Velocity upon Surface and Agitation. Industrial and Engineering Chemistry, 1931; 923-931. <https://doi.org/10.1021/ie50260a018>
- [23] Madhavi B. Cumulative % drug release data of all the formulations, 2011.
- [24] Madhavi BB, Kusum B, Chatanya ChK, Madhu MN, Harsha VS, Banji D. Dissolution enhancement of efavirenz by solid dispersion and PEGylation techniques. Int J Pharm Investig, 2011; 1:1 29-34. <https://doi.org/10.4103/2230-973X.76726>
- [25] Creative Commons Licence 3.0. <https://creativecommons.org/licenses/by-nc-sa/3.0/>.
- [26] Batschelet E. United States. Office of Naval Research., Statistical methods for the analysis of problems in animal orientation and certain biological rhythms, American Institute of Biological Sciences, Washington, 1965.



Boundary layer flow of gold –thorium water based nanofluids over a moving semi-infinite plate

M. Govindaraju*^{1,a}, M. Selvaraj²

¹Department of Mathematics, Padmavani Arts and Science College for Women, Salem, India

²Department of Science and humanities, Ambal professional group of institutions, Coimbatore, India

Article Info

Article history:

Received 14Jan 2020

Revised 09 Jun 2020

Accepted 10 Jun 2020

Keywords:

Nanoparticle Volume Fraction;

HPM; Boundary Layer; Runge Kutta Gill Method

Abstract

The 2-dimensional steady state boundary layer flow of nanofluids over an impermeable semi-infinite moving flat plate is studied. It is assumed that the flat plate moves with a constant velocity. Utilizing similarity transformation, the nonlinear governing equations are transformed to ordinary differential equations and then the resulting ODE is solved using the homotopy perturbation method. The strength of HPM solutions were verified by comparing with numerical results obtained using Runge-Kutta Gill method with shooting technique. Two types of nanoparticles gold and thorium in the water based fluid are considered. The Dimensionless velocity profiles are addressed for various nanoparticles and for different values of the nanoparticle volume fraction. The outcome of the nanoparticle volume fraction on the flow characteristics and mainly on the velocity gradient $f''(0)$ is investigated. It is finding that thorium nanoparticles have the highest velocity compared to Gold nanoparticles, that is the Thorium nanoparticle density is low compared to Gold nanoparticle density. The enhancing values nanoparticle volume fraction slowdown the fluid velocity and velocity gradient is high for Gold compared to Thorium.

© 2020 MIM Research Group. All rights reserved.

1. Introduction

Gold nanoparticles have advantages over other metal nanoparticles due to their biocompatibility and non-cytotoxicity. Gold is utilized internally in human from last fifty years due to their chemical inertness. The size of Gold nanoparticles can be minimized during their synthesis and functionalization with various groups. Gold nanoparticles accumulate in the tumor cells and illustrate optical scattering. So these can act as the probe for the microscopic study of cancer cells. These are also used in chemotherapy and diagnosis of cancer cell. Gold-water nanofluids using molecular dynamics nanofluids belong to a new class of fluids with enhanced thermo physical properties and heat transfer performance.

Nanofluid is a considerable factor affecting the next major industrial revolution of the recent century. Many researchers have focused on modeling the thermal conductivity and obtained different viscosities of nanofluid. Ultra high- performance cooling is one of the most vital needs of many industrial technologies. Choi et al. [1] further a little quantity of nanoparticles to conventional heat transfer fluids and scrutinized the increase of thermal conductivity. Das [2] studied the effect of nanofluid flow past a permeable stretching sheet with slip, thermal buoyancy and heat Source/sink by numerically. Makinde and Aziz [3]

*Corresponding author: govimaths@gmail.com

^aorcid.org/0000-0002-8456-5150;

DOI: <http://dx.doi.org/10.17515/resm2020.174na0114>

Res. Eng. Struct. Mat. Vol. 6 Iss. 4 (2020) 351-361

offered a numerical study on the boundary layer flow induced in a nanofluid due to a linearly stretching sheet with a convective boundary condition. Thiagarajan and Selvaraj [4] investigated nanofluid MHD stagnation point flow over a flat plate with heat transfer. Sobamowo et al. [5-8] presented the various types of nanofluid boundary layer flow problems. Anwar et al. [9] investigated the effect of free convection boundary layer nanofluid flow through a non-linear stretching surface. Bachok et al. [10] presented boundary-layer flow nanofluid past a moving semi-infinite flat plate in unvarying free stream, and establish that dual solutions exist when the plate and the free stream shift in the opposite directions. Bachok et al. [11] presented the problem of the identical free stream of nanofluid parallel to a fixed or moving flat plate by numerically. Presently, number of researchers studied numerical investigation of nanofluid flow over various types of plate problems [Hayate et al. [12, 13], Sheikholeslami [14, 15], Ahmad et al. [16]]. He [17-20] expanded the homotopy perturbation method for solving linear, nonlinear and initial and boundary value problems by combining the standard homotopy and the perturbation methods. Recently, Sobamowo et al. [21-24] studied the homotopy perturbation method for different type of fluids with boundary value problems. Oguntala et al. [25] investigated the homotopy perturbation method for heat transfer process on inclination with porous fin heat sink. By making use of above research work, the plan of the current investigation to study the effect of Gold – Thorium water based nanofluid through a semi-infinite moving plate. The similarity transformations are used and solved by both HPM method and Runge-Kutta Gill method; the solutions are compared with the help of graphs.

2.Mathematical formulation

Consider the 2-dimensional laminar flow through a continuously moving flat horizontal plate embedded in Gold – Thorium water-based nanofluid. The nanofluid can contain each of six types of nanoparticles including gold and thorium. It is considered that the plate has a constant velocity. A uniform spherical size and shape is assumed for the nanoparticles. It is also assumed that the base fluid and the nanoparticles are in the thermal equilibrium, and no velocity slip occurs between the base fluid and the nanoparticles Raftari et al. [26]. Considering these assumptions the laminar boundary layer equations are as follows.

$$\frac{\partial u}{\partial x} + \frac{\partial v}{\partial y} = 0 \tag{1}$$

$$u \frac{\partial u}{\partial x} + v \frac{\partial u}{\partial y} = \frac{\mu_{nf}}{\rho_{nf}} \frac{\partial^2 u}{\partial y^2} \tag{2}$$

The principal boundary conditions are as follows:

$$\begin{aligned}
 u &= U_w, v = 0, \text{ at } y = 0 \\
 u &\rightarrow 0 \text{ as } y \rightarrow \infty
 \end{aligned}
 \tag{3}$$

In which U_w is the plate velocity which is constant, and x and y directions with corresponding velocity components are u and v respectively. Where the viscosity of the nanofluid μ_{nf} , the density of the nanofluid ρ_{nf} .

$$\mu_{nf} = \frac{\mu_f}{(1-\phi)^{2.5}}, \rho_{nf} = (1-\phi)\rho_f + \phi\rho_s \tag{4}$$

Where μ_f is the viscosity of the fluid, ρ_f and ρ_s are the reference density of the fluid fraction and solid fraction respectively, and ϕ is the nanoparticle volume fraction.

The similarity variable and stream functions are defined as follows,

$$\eta = \frac{y}{x} \text{Re}_x^{\frac{1}{2}}, \quad f(\eta) = \frac{\psi(x, y)}{(U_w \nu_f x)^{\frac{1}{2}}} \tag{5}$$

Where the local Reynolds number is $\text{Re}_x = U_w x / \nu_f$, in which the kinematic viscosity of the base fluid (water) is ν_f . The stream function is $\psi(x, y)$ which identically satisfies Eq.(1) and is defined as $u = \frac{\partial \psi}{\partial y}, v = -\frac{\partial \psi}{\partial x}$.

The dimensionless momentum and boundary conditions are as follows;

$$f''' + \frac{1}{2}(1-\phi)^{2.5} \left(1 - \phi + \phi \frac{\rho_s}{\rho_f} \right) f f'' = 0 \tag{6}$$

with the boundary conditions

$$f(0) = 0, f'(0) = 1, f'(\infty) = 0 \tag{7}$$

The significant quantity is the local skin friction coefficient $C_{f,x}$ defined as $c_{x,f} = \tau_w / \rho_f U_w^2$ in which the plate surface shear stress is given as $\tau_w = \mu_{nf} (du / dy)_{y=0}$. Use of the similarity parameters (5) gives [27].

$$C_{f,x} \text{Re}_x^{0.5} = \frac{f''(0)}{(1-\phi)^{2.5}} \tag{8}$$

3. Solution by homotopy perturbation method (HPM)

Using HPM [17, 18, 19 and 20], the original nonlinear ODE (which cannot be solved easily) is divided into some linear ODEs.

At first, the governing ODE (6) and the boundary conditions (7) are written as:

$$u''' + \frac{1}{2}(1-\phi)^{2.5} \left(1 - \phi + \phi \frac{\rho_s}{\rho_f} \right) u u'' = 0; \tag{9}$$

$$u(0) = 0, u'(0) = 1, u'(\infty) = 0 \tag{10}$$

Then, a homotopy is constructed in the following form:

$$u''' - \alpha^2 u' + p \left(\frac{1}{2}(1-\phi)^{2.5} \left(1 - \phi + \phi \frac{\rho_s}{\rho_f} \right) u u'' + \alpha^2 u' \right) = 0. \tag{11}$$

According to HPM, the following series in terms of powers of p is substituted in Eq. (11):

$$u = u_0 + pu_1 + p^2u_2 + \dots \tag{12}$$

After some algebraic manipulation, equating the identical powers of ρ to zero gives:

$$p^0 : u_0''' - \alpha^2 u_0' = 0; u_0(0) = 0, u_0'(0) = 1, u_0'(\infty) = 0; \tag{13}$$

$$p^1 : \left. \begin{aligned} &u_1''' - \alpha^2 u_1' + \frac{1}{2}(1-\varphi)^{2.5} \left(1 - \varphi + \varphi \frac{\rho_s}{\rho_f} \right) u_0 u_0'' + \alpha^2 u_0' = 0; \\ &u_1(0) = 0, u_1'(0) = 0, u_1'(\infty) = 0; \end{aligned} \right\} \tag{14}$$

$$p^2 : \left. \begin{aligned} &u_2''' - \alpha^2 u_2' + \frac{1}{2}(1-\varphi)^{2.5} \left(1 - \varphi + \varphi \frac{\rho_s}{\rho_f} \right) \times (u_0 u_1'' + u_1 u_0'') + \alpha^2 u_1' = 0; \\ &u_2(0) = 0, u_2'(0) = 0, u_2'(\infty) = 0 \end{aligned} \right\} \tag{15}$$

Eq. (13) for ρ^0 has the following solution:

$$u_0(\eta) = \frac{1}{\alpha} (1 - \exp(-\alpha\eta)). \tag{16}$$

Here α is a constant which is further to be determined. If solution (16) for u_0 is substituted in the equation for ρ^1 , Eq. (14), it will become as:

$$u_1''' - \alpha^2 u_1' = \left[\frac{1}{2}(1-\varphi)^{2.5} \left(1 - \varphi + \varphi \frac{\rho_s}{\rho_f} \right) - \alpha^2 \right] \times \exp(-\alpha\eta) - \frac{1}{2}(1-\varphi)^{2.5} \left(1 - \varphi + \varphi \frac{\rho_s}{\rho_f} \right) \times \exp(-2\alpha\eta) \tag{17}$$

Eq. (17) for u_1 can be solved in an unbounded domain under the boundary conditions $u_1(0) = 0, u_1'(0) = 0, u_1'(\infty) = 0$ (as it is shown in the Appendix) [17],

which gives u_1 as:

$$u_1(\eta) = \left(\frac{1}{2\alpha} - \frac{\Omega}{6\alpha^3} \right) + \frac{\Omega}{12\alpha^3} \exp(-2\alpha\eta) + \left(-\frac{1}{2\alpha} + \frac{\Omega}{12\alpha^3} \right) \exp(-\alpha\eta). \tag{18}$$

in which $a = (\Omega/2)^{0.5}$ and $\Omega = (1-\varphi)^{2.5} \left[1 - \varphi + \varphi \left(\frac{\rho_s}{\rho_f} \right) \right]$ it should be noted that α can be $\alpha = \pm \left(\frac{\Omega}{2} \right)^{2.5}$, but here as α is demanded to be positive ($\alpha > 0$), therefore $a = (\Omega/2)^{2.5}$. Thus the first order approximate semi analytical solution $f(\eta) = u(\eta) + u_1(\eta)$ becomes as:

$$f(\eta) = \left(\frac{3}{2\alpha} - \frac{\Omega}{6\alpha^3} \right) + \frac{\Omega}{12\alpha^3} \exp(-2\alpha\eta) + \left(-\frac{3}{2\alpha} + \frac{\Omega}{12\alpha^3} \right) \exp(-\alpha\eta). \tag{19}$$

According to Eq. (19), the dimensionless plate surface shear stress is as:

$$f''(0) = -\frac{3}{2}\alpha + \frac{5\Omega}{12\alpha} \tag{20}$$

4. Numerical Analysis

The equations (6) with boundary conditions are solved numerically using the Runge-Kutta Gill method algorithm with a systematic governing of $f''(0)$ by the shooting technique until the boundary conditions are satisfied. The step size is taken as $\Delta\eta = 0.01$. The process is repeated until the results are correct up to the desired accuracy of 10^{-5} level. Numerical results are found for several values of the nanoparticle volume fraction ϕ on velocity $f'(\eta)$ and velocity gradient $f''(0)$. Table 1 compares the HPM solution and numerical solution values of the dimensionless fluid velocity gradient at the surface $f''(0)$ for gold and thorium water nanofluids for various values of the nanoparticle volume fraction ϕ .

Table 1. Values of velocity gradient $f''(0)$ for some values ϕ for thorium and gold water nanofluids.

ϕ	Thorium (HPM)	Thorium (Numerical)	Gold (HPM)	Gold (Numerical)
0	-0.471404	-0.44411	-0.471404	-0.44411
0.1	-0.594801	-0.55999	-0.695050	-0.65412
0.2	-0.632370	-0.59599	-0.769766	-0.72461

Table 2. Thermophysical properties of base fluid and the nanoparticles at 288K

	Water	Thorium	Gold
$\rho(kg/m^3)$	1000.5	11724	19300
$C_p(j/kgK)$	4181.8	118	126
$k(W/mK)$	0.59	54	318

5. Results and Discussion

In this study, boundary layer flow of nanofluids over a semi-infinite moving flat plate embedded in the water-based nanofluid is investigated analytically utilizing homotopy perturbation method. Also, comparison between the numerical results and HPM solution of velocity including different values of active parameters is shown in this figure. In table. 2 the density of water and nanoparticles used in the present study are given.

Figure 1 and 2 display the effect of nanoparticle volume fraction on the velocity profiles of the thorium and gold water nanofluids. It is clear that an increase in the nanoparticle volume fraction decreases the velocity profiles. This phenomenon occurs because presence of the nanoparticles leads to further thinning of boundary layer thickness. The physical meaning is the increasing value of nanoparticle volume fraction means the fluid density is increased, so fluid velocity is reduced [6].

From Figure 3 it is observed that the thorium nanoparticles have the highest value of velocity profile compared to gold nanoparticles. The velocity profile of a nanofluid is based on the density of the nanofluids. The reason is thorium nanoparticle have low density compared to gold nanoparticle.

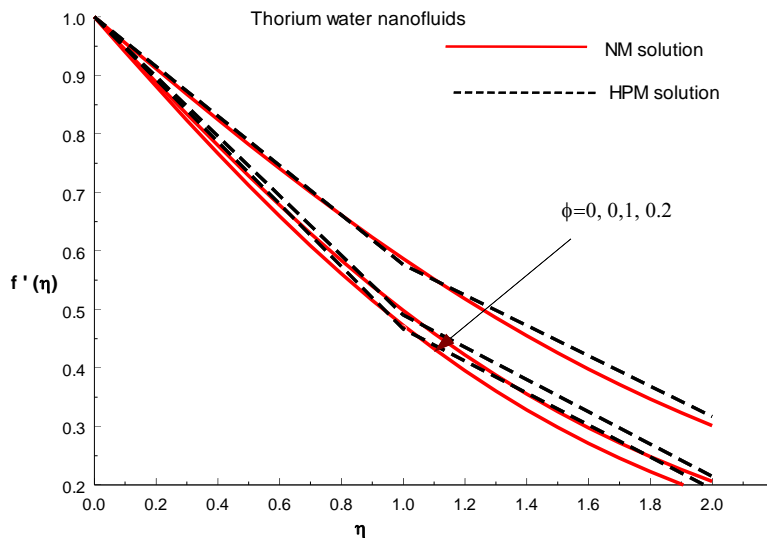


Fig. 1 Velocity profiles $f'(\eta)$ for different nanoparticle volume fractions for thorium water nanofluid.

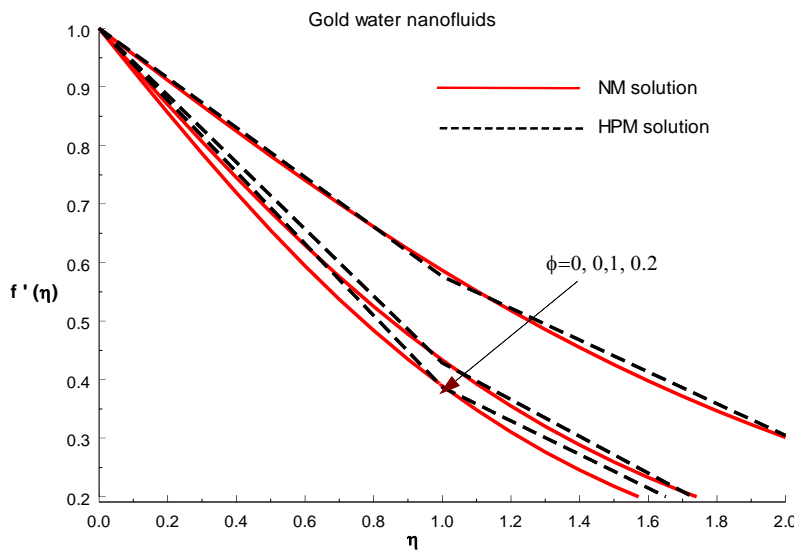


Fig. 2 Velocity profiles $f'(\eta)$ for different nanoparticle volume fractions for gold water nanofluid.

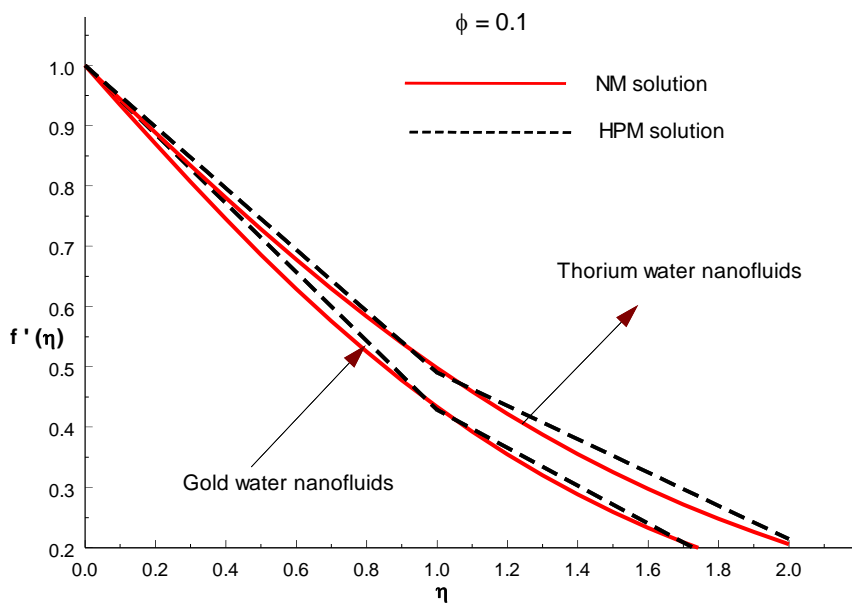


Fig. 3 Velocity profiles $f'(\eta)$ for different nanoparticles when $\phi = 0.1$.

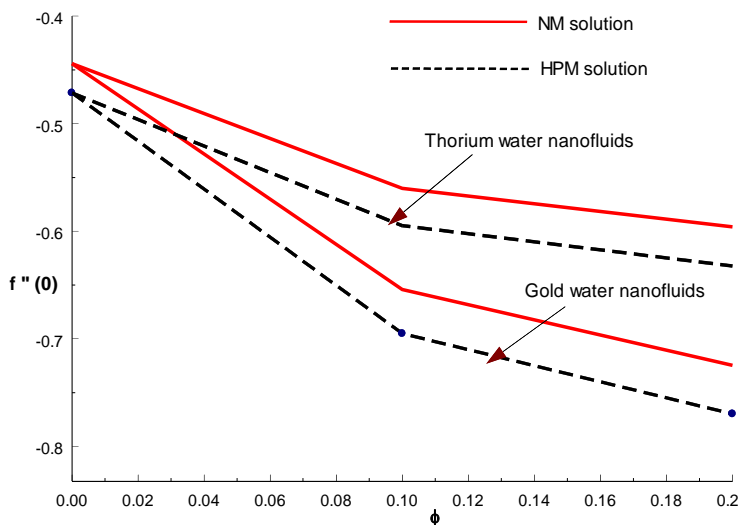


Fig. 4 Effect of the nanoparticle volume fraction ϕ on the fluid velocity gradient for different types of nanofluids.

Figure 4 presents the variations of $f''(0)$ with ϕ for various nanoparticles (Gold and Thorium) using HPM solution from Table 1. It is seen that with the increase of ϕ the magnitude of $f''(0)$ increases for thorium-water and gold-water working fluids. Comparison of Figure 4 with the nanoparticles densities in table 2 makes it clear that the nanoparticles with higher density result in higher magnitudes of $f''(0)$.

6. Conclusion

In this work was to examined the effect of convective boundary layer flow of a Gold – Thorium water based nanofluid through a moving flat plate by both analytically and numerically. Analytically by HPM method and numerically by Runge-Kutta Gill method. The effects of different nanofluids on Skin friction and velocity profiles are discussed with the help graph. The main concluding observations can be summarized as follows:

- The two dimensional boundary layer flows of nanofluids over an impermeable consciously moving horizontal plate is studied. The results show that the present HPM solution with only two terms agrees within 3% error with numerical solutions for the velocity gradient at the plate surface.
- Thorium nanoparticles have the highest value of velocity profile compared to gold nanoparticles.
- Velocity gradient decreases with increasing values of nanoparticle volume fraction for both of thorium water nanofluid and gold water nanofluid
- Increasing values nanoparticle volume fraction decreases the velocity profile.

Nomenclature

(u, v)	velocity of the fluid in the x, y directions respectively(m/s)
Cf_x	skin friction coefficient
Re_x	local Reynolds number
x	distance along the surface (m)
y	distance normal to the surface (m)
f	dimensionless stream functions

Greek Symbols

η	similarity variable
ρ	density of the fluid (kg/m ³)
ν_f	kinematic viscosity of the base fluid (water)
ρ_f	density of the fluid fraction
ρ_s	density of solid fraction
μ_f	the viscosity of the fluid
μ_{nf}	viscosity of the nanofluid
ρ_{nf}	the density of the nanofluid
ϕ	the nanoparticle volume fraction

References

- [1] Choi SUS, Zhang ZG, Yu W, Lockwood FE, Grulke EA. Anomalously thermal conductivity enhancement in nanotube suspensions, *Appl. Phys. Lett.*, 2001; 2252-2254. <https://doi.org/10.1063/1.1408272>
- [2] Das K. Slip flow and convective heat transfer of nanofluids over a permeable stretchingsurface, *Computers & Fluids.*, 2012;64;34-42. <https://doi.org/10.1016/j.compfluid.2012.04.026>
- [3] Makinde OD, Aziz A. Boundary layer flow of a nanofluid past a stretching sheet with a convective boundary condition, *Int. J. Thermal Sci.* 2011; 50; 1326-1332. <https://doi.org/10.1016/j.ijthermalsci.2011.02.019>
- [4] Thiagarajan M, Selvaraj M. Nanofluid MHD stagnation point flow over a flat with heat transfer, *Journal of Nanofluids*, 2015; 4; 328-334. <https://doi.org/10.1166/jon.2015.1165>
- [5] Sobamowo G.M, Akinshilo A, Yinusa A.A., Two-dimensional flow analysis of nanofluid through a porous channel with suction/injection at slowly expanding/contracting walls using variation of parameter method, *Trans. Phenom.Nano.Micro.Scales*,2019;7(2);120-129.
- [6] Sobamowo G.M, Yinusa A.A., Insight into the Boundary layer flows of free convection and heat transfer of nanofluids over a vertical plate using multi-step differential transformation method, *Iranian Journal of Mechanical Engineering*, 2019;20;5-45.
- [7] Sobamowo G.M, Adeleye O.A., Yinusa A.A., Heat Transfer And Flow Analysis of Magnetohydrodynamic Dissipative Carreau Nanofluid Over A Stretching Sheet with

- Internal Heat Generation, Journal of Computational and Engineering Mathematics, 2019;6; 3-26. <https://doi.org/10.14529/jcem190101>
- [8] Sobamowo M.G, Yinusa A.A, Oluwo A.A, Alozie S.I., Finite element analysis of flow and heat transfer of dissipative Casson-Carreau nanofluid over a stretching sheet embedded in a porous medium, Aeron Aero Open Access J. 2018;2(5);294-308. <https://doi.org/10.15406/aaaj.2018.02.00064>
- [9] Anwar MI, Khan I, Sharidan S, Salleh MZ. Conjugate effects of heat and mass transfer of nanofluids over a nonlinear stretching sheet, Int. J.Physical Sciences, 2012;7; 4081-4092. <https://doi.org/10.5897/IJPS12.358>
- [10] Bachok N, Ishak A, Pop I. Boundary-layer flow of nanofluids over a moving surface in a flowing fluid, Int. J. Thermal Sci. 2010;49; 1663-1668. <https://doi.org/10.1016/j.ijthermalsci.2010.01.026>
- [11] Bachok N, Ishak A, Pop I. Flow and heat transfer characteristics on a moving plate in a nanofluid, Int. J. Heat Mass Transfer, 2012;55; 642-648. <https://doi.org/10.1016/j.ijheatmasstransfer.2011.10.047>
- [12] Hayat T, Rashid M, Alsaedi A, Ahmad B. Flow of nanofluid by nonlinear stretching velocity, Results in Physics, 2018; 8; 1104-1109. <https://doi.org/10.1016/j.rinp.2017.12.014>
- [13] Hayat T, Rashid M, Alsaedi A. Three dimensional radiative flow of magnetitenanofluid with homogeneous-heterogeneous reactions, Results in Physics, 2018; 8; 268-275. <https://doi.org/10.1016/j.rinp.2017.11.038>
- [14] Sheikholeslami M, Shehzad SA. Simulation of water based nanofluid convective flow inside a porous enclosure via non-equilibrium model, Int. J. Heat. Mass. Transfer, 2018; 120; 1200-1212. <https://doi.org/10.1016/j.ijheatmasstransfer.2017.12.132>
- [15] Sheikholeslami M, Jafaryar M, Zhixiong Li. Second law analysis for nanofluid turbulent flow inside a circular duct in presence of twisted tape turbulators, Journal of Molecular liquids., 2018; 263; 489-500. <https://doi.org/10.1016/j.molliq.2018.04.147>
- [16] Ahmad S, Rohani AM, Pop I. Blasius and Sakiadis problems in nanofluids, Acta Mech. 2011;218;195-204. <https://doi.org/10.1007/s00707-010-0414-6>
- [17] He JH. Homotopy perturbation technique for solving boundary value problems, PhysicsLettersA,2006;350;87-88. <https://doi.org/10.1016/j.physleta.2005.10.005>
- [18] He JH. Homotopy perturbation technique, Computer Methods in Applied Mechanics and Engineering.,1999;178; 257-262. [https://doi.org/10.1016/S0045-7825\(99\)00018-3](https://doi.org/10.1016/S0045-7825(99)00018-3)
- [19] He J.H., A Coupling method of a homotopy technique and a perturbation technique for non-linear problems, International Journal of Non-Linear Mechanics. 2000; 35; 37-43. [https://doi.org/10.1016/S0020-7462\(98\)00085-7](https://doi.org/10.1016/S0020-7462(98)00085-7)
- [20] He J.H., Periodic solutions and bifurcations of delay-differential equations, Physics Letters A. 2005; 347; 228-230. <https://doi.org/10.1016/j.physleta.2005.08.014>
- [21] Sobamowo M.G, Akinshilo A.T, Yinusa A.A., Thermo-Magneto-Solutal Squeezing flow of nanofluid between two parallel disks embedded in a porous medium: Effects of nanoparticle geometry, slip and temperature jump conditions, Modelling and Simulation in Engineering, 2018;1-18; 7364634. <https://doi.org/10.1155/2018/7364634>
- [22] Sobamowo M.G, Yinusa A.A., Thermo-fluidic parameters effects on nonlinear vibration of fluid-conveying nanotube resting on elastic foundations using homotopy perturbation method, Journal of Thermal Engineering, 2018; 4(8); 2211-2233. <https://doi.org/10.18186/journal-of-thermal-engineering.434043>
- [23] Sobamowo M.G, Adeleye O, Yinusa A.A., Analysis of convective-radiative porous fin with temperature-dependent internal heat generation and magnetic field using homotopy perturbation method, Journal of Computational and Applied Mechanics, 2017; 12(2);127-145. <https://doi.org/10.32973/jcam.2017.009>

- [24] Sobamowo G, Alaribe K.C, Yinusa A. Homotopy perturbation method for analysis of squeezing axisymmetric flow of first-grade fluid under the effects of slip and magnetic field, *Journal of Computational and Applied Mechanics*, 2018;13(1) 51-65. <https://doi.org/10.32973/jcam.2018.004>
- [25] Oguntala G, Sobamowo G, Yinusa A, Abd-Alhameed R. Application of Approximate Analytical Technique Using the Homotopy Perturbation Method to Study the Inclination Effect on the Thermal Behavior of Porous Fin Heat Sink, *Math. Comput. Appl.* 2018;23(62);1-12. <https://doi.org/10.3390/mca23040062>
- [26] Raftari B, Mohyud-din ST, Yildirim A. Solution to the MHD flow over a non-linear stretching sheet by homotopy perturbation method, *Science China Physics Mechanics & Astronomy*, 2011;54; 342-345. <https://doi.org/10.1007/s11433-010-4180-1>
- [27] Noghrehabadi A, Pourrajab R, Ghalambaz M. Effect of partial slip boundary condition on the flow and heat transfer of nanofluids past stretching sheet prescribed constant wall temperature, *Int. J. Thermal Science.*, 2012; 54; 253-261. <https://doi.org/10.1016/j.ijthermalsci.2011.11.017>

Blank Page



Research Article

Evaluation of annual performance of a photovoltaic thermal system integrated with natural zeolites

Canan Kandilli^{*a}, Mert Uzel

Department of Mechanical Engineering, Usak University, Usak, Turkey

Article Info

Article history:
Received 18 Jun 2020
Revised 02 Aug 2020
Accepted 20 Aug 2020

Keywords:

Photovoltaic Thermal Systems;
Natural Zeolites;
Thermal management;
Annual performance

Abstract

Photovoltaic thermal systems (PVT) produces both electricity and thermal energy by the same module. However, solar energy exhibits non-continuous character, and causes some problems for obtaining stabile energy due to its unsteady regime. Thermal energy storage systems could be employed as a solution the mentioned problems. There are no studies in the literature regarding evaluation of the annual performance of PVT systems integrated with natural zeolites. It is the motivation behind of the present study. Natural zeolites could be utilized for thermal storage and management with PVT systems. In this study, it is aimed to performed annual performance of the PVT system integrated with natural zeolite as a thermal storage material to manage the excessive heat on PV. Average overall energy efficiency values were found as 0.56; 0.54; 0.49; 0.49; 0.48; 0.46; 0.45; 0.46; 0.50; 0.53; 0.54 and 0.56 from January to December, respectively. Annual total overall energy produced by the PVT system integrated with natural zeolite was found as 1294.88 kWh/year per module. Annual saving per module is reached as 117.83 € per module. With the acceptance of the system cost of 942.8 €, simple payback period is approximately 8 years. This payback time, which is found on a single module, will surely decrease at higher installed powers.

© 2020 MIM Research Group. All rights reserved.

1. Introduction

For crystalline silicon photovoltaic (PV) cells, a drop in the electrical power output of about 0.2–0.5% was reported for every 1°C rise in the PV module temperature principally due to the temperature dependence of the open-circuit voltage of the cell depending on the PV technology [1]. Photovoltaic Thermal System (PVT) presents a useful solution to overcome the excessive heat on PV surface [2]. During the melting or solidification processes, a Phase Change Material (PCM) can store or release a large amount of latent heat. The temperature of the PCM can be maintained during the latent heat transfer process. Therefore, PCM is a very promising material for energy storage and for controlling the thermal environment. In the last decades, there are numerous studies on PVT systems integrated with PCM have been carried out in the literature [3-10].

However, PCMs have many disadvantages in practice and natural zeolite for PVT system as a heat storage material to manage excessive heat has been newly proposed [11]. As known, PCMs are the first material that comes to mind to provide more thermal energy in PVTs. However, it is a critical advantage that natural zeolite has almost free, very affordable cost. On the other hand, PCMs significantly increases PVT costs. Another issue is ease of application. Natural zeolite can be easily integrated into PVTs than PCMs. In order to use paraffin, it is necessary to melt, split or apply as microcapsules. It is also necessary to

*Corresponding author: canan.kandilli@usak.edu.tr

orcid.org/0000-0001-7159-4174

DOI: <http://dx.doi.org/10.17515/resm2020.200en0618>

Res. Eng. Struct. Mat. Vol. 6 Iss. 4 (2020) 363-374

quickly remove paraffin from the PVT system when it is hot. High cost, harmful to health and risk of leakage make PCMs disadvantageous. On the other hand, natural zeolites are superior to PCMs in terms of human health in terms of both antibacterial structure and lack of harmful chemicals.

Zeolite is a porous crystalline hydrated aluminosilicate with a cage-like structure. Its framework structure encloses cavities occupied by water molecules and cations which can move freely permitting reversible dehydration and ion exchange. There are more than 40 types natural zeolites while synthesized zeolites have more than 150 types [12]. 75% of natural zeolite reserve takes place in Turkey, half of the reserved in Turkey are in Gordes. Other significant zeolite deposits in Turkey Ankara, Kütahya, Manisa, İzmir, Balıkesir and is located in Cappadocia. The main physical and chemical properties of zeolites are; the ability to make ion exchanges, adsorption and molecular sieve structure, silica content, as well as being light colored in sedimentary zeolites, lightness, pore structure of small crystals caused zeolites to be used in a wide variety of industrial areas. Usage areas of one or more of these properties of natural zeolites which have become an important industrial raw material in recent years are Pollution Control; Mining and Metallurgy; paper, building, health and chemistry sectors [13] In the literature, PVTs have been integrated with PCMs so far. Natural zeolites have many advantages over PCMs. In this study, natural zeolites are recommended for thermal management and heat storage of PVTs. Moreover, in the efficiency calculations in the study, the stored thermal energy that the zeolite will provide to the system after the sunset is not taken into consideration. Considering the stored temperature, the integration of zeolites with PVT is a remarkable alternative.

In this study, annual performance of the PVT system integrated with natural zeolite to control the excessive heat on PV module has been evaluated. There is no study on the annual performance of the natural zeolite based PVT system in the literature. It is the motivation of the present study. However, some studies on annual performance of PVT systems could be found in the literature. Brottier and Bennacer performed a statistical study was realized to analyze in-field performances of twenty-eight hybrid solar domestic hot water installations equipped with innovative non-overglazed PVT collectors in Western Europe. They showed that PVT technology, more than PV production, is particularly relevant on domestic hot water preheating, with a monthly average of daily maximal temperature in the panels reaching above 45°C during 5 months in the year [14]. Ji et al. established a mathematical model, verified by experimentally, evaluated annual performance and investigated aspect ratio of a building integrated PV system (BIPV) to analyze seasonal energy demand of four cities of China [15]. Gholami and Røstvik presented BIPV as a building envelope material for the whole building skins, performed economic analyses of a BIPV system in 30 countries. They emphasized that even the north facade is economically feasible in some countries in Europe if all the environmental and societal benefits of the BIPV system are being taken into consideration [16].

In the present study, it is aimed to performed annual performance of the PVT system integrated with natural zeolite as a thermal storage material to manage the excessive heat on PV. There are no studies in the literature regarding evaluation of the annual performance of PVT systems integrated with natural zeolites. It is the motivation behind of the present study. Firstly, mathematical models were derived by experimental data and solar irradiance values. These models were employed to estimate monthly average hourly values of overall energy efficiency, produced electrical power, overall produced energy and savings by PVT system based on natural zeolites. Estimated parameters were calculated depending on solar irradiance data that found by taking the average of 8-year hourly data. Evaluation of annual performance of the PVT integrated with natural zeolites is firstly presented in the open literature.

2. System Description

It is very important to analyze the energy systems thermodynamically to determine system efficiency. For this aim, the following assumptions have been considered:

- PV surface temperature is assumed as a constant through the PV module.
- The system is assumed as steady-state open system.
- Inner surface of fluid channel is smooth.
- The thermal resistance of the fluid channel and radiation losses is ignored.
- Atmospheric pressure is assumed as $P_0 = 1 \text{ atm}$.
- The heat losses for the bottom and the edge surface of the PVT could be ignored due to the insulation layer.
- The dead state temperature is assumed as equal to the ambient temperature.

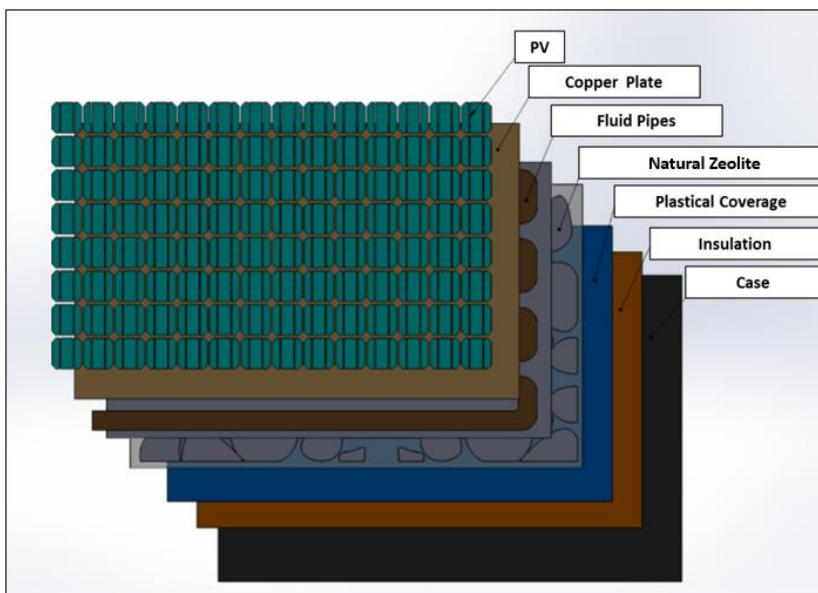


Fig 1. Diagram of the layers of PVT-Zeolite system.

The layers of PVT system integrated with natural zeolite are shown in Fig.1 for the present study. Solar radiation, which cannot be converted into electricity by solar cells, creates an excessive heat on PV. This excessive heat is removed by the working fluid and is stored as sensible heat in the zeolite layer. Thus, the stored heat energy will continue to provide thermal energy at times when solar energy is not sufficient or after the sun goes down. Furthermore, the heat load on the PV will also be removed and the electrical efficiency will be reduced. Energy analysis of the PVT systems based on natural zeolite has been reported in detail before [11]. For this reason, a short reminder about the parameters used in this study will be made.

$$\dot{Q}_{\text{thermal}} = \dot{m}C_p(T_{\text{out}} - T_{\text{in}}) \tag{1}$$

In the above equation, \dot{Q}_{thermal} is the useful power (W), \dot{m} is mass flow rate of working fluid, T_{in} and T_{out} are inlet and outlet temperatures and C_p is specific heat respectively.

The thermal (η_{thermal}) and electrical efficiency (η_{PV}) of the PVT system could be defined as below, respectively:

$$\eta_{\text{thermal}} = \frac{\dot{Q}_{\text{thermal}}}{I \times A_c} \quad (2)$$

$$\eta_{\text{PV}} = \frac{\dot{W}_{\text{PV}}}{I \times A_c} \quad (3)$$

$$\dot{W}_{\text{PV}} = I \cdot V \quad (4)$$

Electrical power is the product of voltage and current obtained from PV. Overall power is the sum of thermal and electrical power:

$$\dot{Q}_{\text{overall}} = \dot{Q}_{\text{thermal}} + \dot{W}_{\text{PV}} \quad (5)$$

3. Results

The aim of this study is to reveal the annual performance evaluation in the light of the data obtained from PVT systems based on natural zeolite. First of all, the statistical relationships between solar irradiance and electrical power, overall energy efficiency and produced overall energy have been presented. The mathematical models were derived from these relationships to estimate annual values by using solar irradiance data in hourly basis. Electrical power, overall system energy efficiency and produced overall power values were hourly calculated by these models for whole year. Then, for all these parameters, monthly average hourly values were reached. Monthly savings from the PVT systems integrated with natural zeolite has been calculated.

In the present study, global solar irradiance, ambient temperature and wind speed data have been obtained by the meteorology station (Davis Vantage Pro2) established on the terrace of the building of Department of Mechanical Engineering. These meteorological data has been recorded since 2011. Usak, as a small Anatolian province, is located at a latitude of 38.41 °N, longitude of 29.25 °E and altitude of 906 m. Usak, located in the transition region from Mediterranean climate belt to continental climate condition, has hot and dry summers and long cold winters.

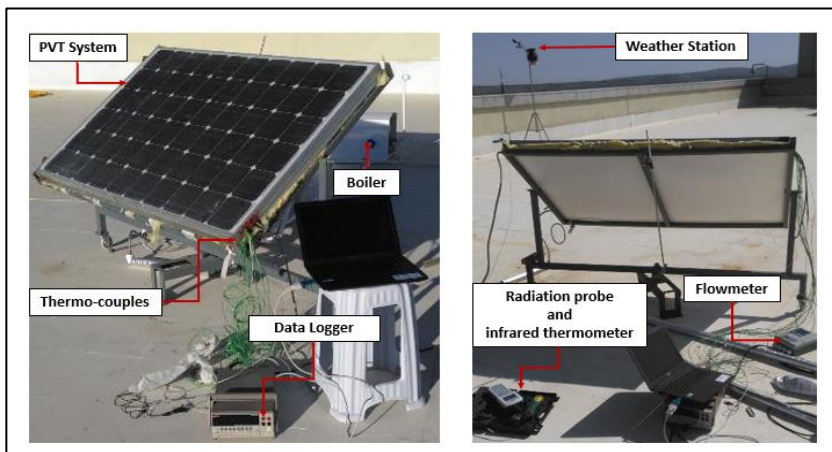


Fig 2. PVT test system based on natural zeolites and measuring devices.

PVT test system based on natural zeolites and measuring devices are presented by Fig.2. The PVT experiments were carried out on the roof of the Usak University Mechanical Engineering Building on April, May and June 2016 under different meteorological conditions. In natural zeolite PVT system experiments operating naturally under a flow of 18 l/h, inlet and outlet temperatures, surface temperatures and surface solar radiation, flow and meteorological data were measured, uncertainties and theoretical analysis were presented in previous studies [11]. Figures 3-5 present the statistical relationships between overall energy efficiency, electrical power (W) and overall power (W) that is sum of thermal and electrical power produced by PVT system and solar irradiance on PVT surface. Determination coefficients were found as 0.9543; 0.9294 and 0.9254 for the relations between overall energy efficiency, electrical power and overall power and solar radiation on PVT surface. Derived models by these statistical relationships were employed to calculate the monthly average of hourly values of overall energy efficiency, electrical power, and overall power for a whole year. Hourly solar radiation data required to make calculations. By using these parameters models were calculated using 8-year solar radiation data obtained from the weather station. As it is known, weather station measures the global solar radiation on horizontal surface. However, the PVT system in this study was directed to the south and a 38° tilt angle was given. The hourly solar radiation data received from the meteorology station was directed to the south and the solar radiation coming to the 38° inclined panel was calculated hourly. Detailed information on the calculation of solar radiation on the inclined surface is available in the basic literature [15]. As a result, based on the experimental models, annual total energy efficiency, electrical power and total power calculations were made for PVT with solar radiation data on an hourly basis. The results for these calculations are presented below.

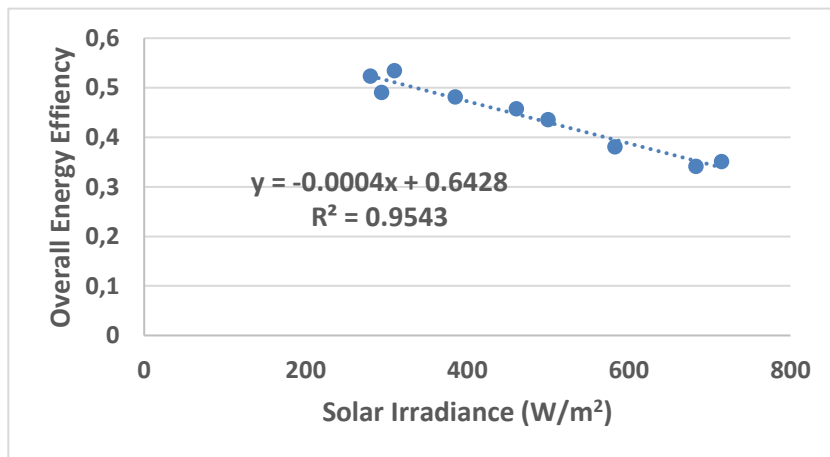


Fig 3. Statistical relationship between overall energy efficiency of the PVT system and solar irradiance (W/m²)

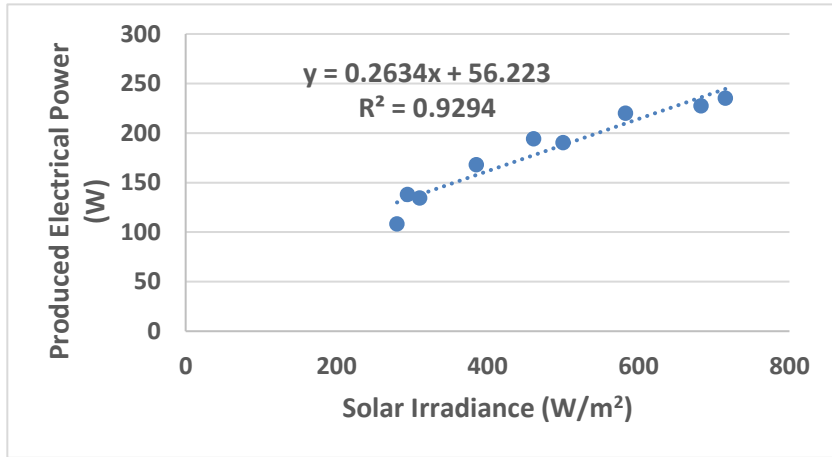


Fig 4. Statistical relationship between electrical power produced by the PVT system and solar irradiation (W/m²)

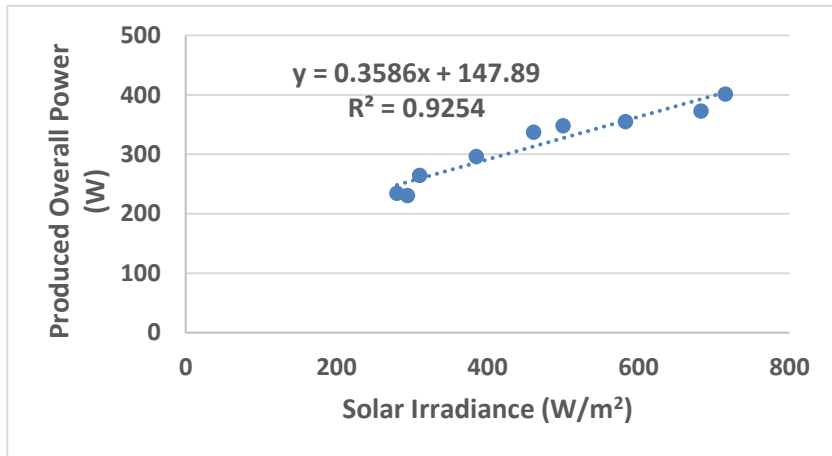


Fig 5. Statistical relationship between overall power produced by the PVT system and solar irradiation (W/m²)

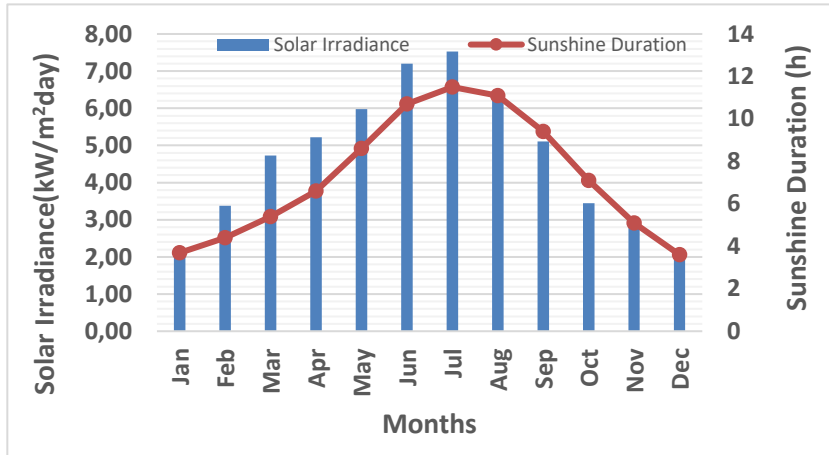


Fig 6. Monthly variation of average daily solar irradiance (kW/m²day) and sunshine duration (h)

Variation of monthly variation of average daily solar irradiance (kW/m²day) and sunshine duration (h) were plotted in Fig. 6. To calculate monthly variation of average daily solar irradiance, for all days of the month in question, the average of the data at a certain hour is taken. For example, for all days of January (Jan 1-31), all irradiation values in each hour are summed and divided by 31, the number of days per month. Thus, hourly values that characterize the relevant month were obtained. For each calculation, 8760 solar radiation data were used. Monthly variation of average daily solar irradiance values were found as 2.11; 3.38; 4.73; 5.22; 5.98; 7.20; 7.53; 6.44; 5.11; 3.44; 2.85; 2.13 from January to December, respectively. One of the important data in energy calculations produced from photovoltaic panels is sunshine duration. Monthly average sunshine duration values for Usak Province were also given by Fig.6. That is listed as 3.7; 4.4; 5.4; 6.6; 8.6; 10.7; 11.5; 11.1; 9.4; 7.1; 5.1 and 3.6 hours for January to December, respectively [18]. Yearly average sunshine duration is 7.3 hours/day for the study location. As expected, the total solar radiation increases as the sunshine duration increases. Surely, the main purpose in providing this information is to show under which solar radiation conditions performance evaluations are obtained.

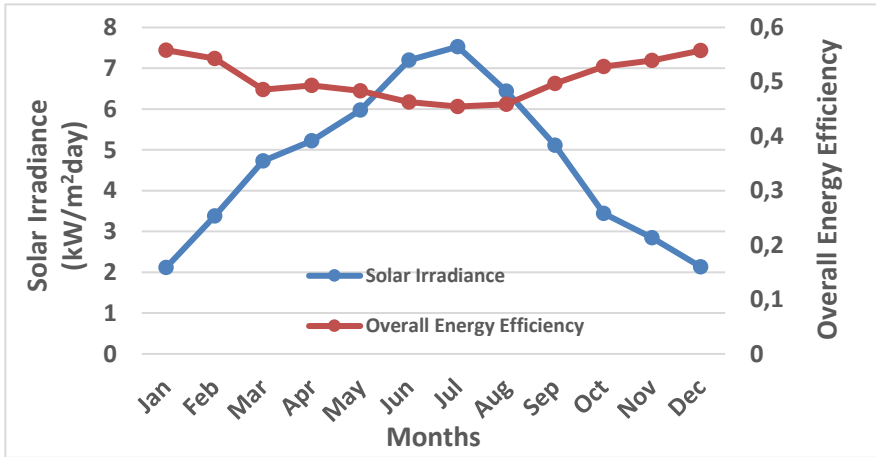


Fig 7. Monthly variation of overall energy efficiency against average daily solar irradiance (kW/m²/day)

Fig 7 gives monthly variation of overall energy efficiency against average daily solar irradiance (kW/m²/day). Average overall energy efficiency values were found as 0.56; 0.54; 0.49; 0.49; 0.48; 0.46; 0.45; 0.46; 0.50; 0.53; 0.54 and 0.56 from January to December, respectively. As with all thermal collectors, the efficiency of the system decreases as the solar radiation increases.

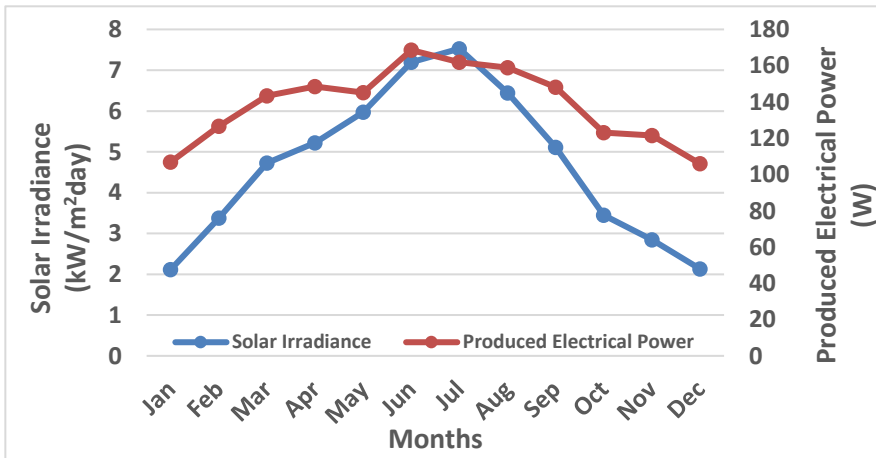


Fig 8. Monthly variation of produced electrical power (W) against average daily solar irradiance (kW/m²/day)

Monthly variation of produced electrical power and monthly variation of overall produced energy (kWh) by solar irradiance are given by Fig.8 and Fig.9. As the solar radiation increases, the electrical power produced and the overall energy increase. Monthly average hourly produced electrical power values per module were calculated as 106.8; 126.7;

143.4; 148.5; 145.2; 168.6; 161.9; 158.9; 148.2; 123.0; 121.4 and 105.9 W from January to December, respectively. Similarly, monthly average overall produced energy values (kWh) were determined as 73.93; 85.39; 105.59; 117.66; 131.15; 148.04; 151.35; 131.67; 117.50; 87.12; 79.90 and 65.59 from January to December, respectively. After calculating the hourly average values representing all the days of that month for each month, the daily total values were found, multiplied by the number of days in the relevant month, so the monthly average total produced energy was calculated. Annual total overall energy produced by the PVT system integrated with natural zeolite was found as 1294.88 kWh/year per module.

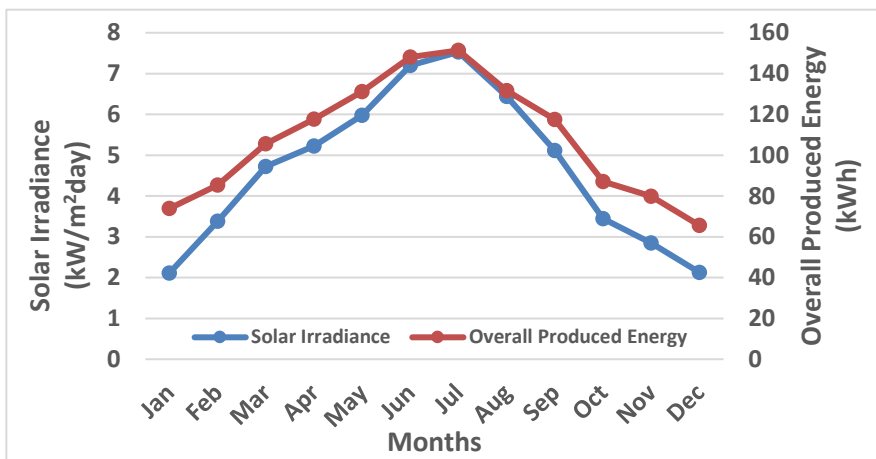


Fig 9. Monthly variation of overall produced energy (kWh) against average daily solar irradiance (kW/m²day)

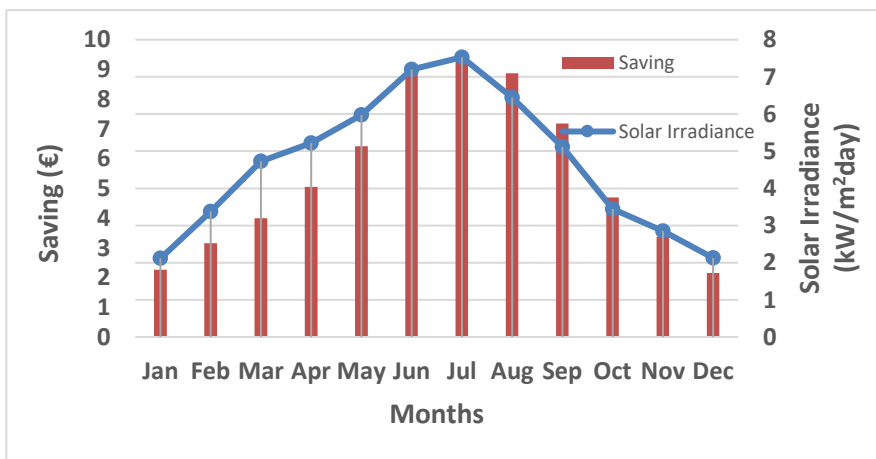


Fig 10. Monthly variation of savings (€) by average daily solar irradiance (kW/m²day)

Regarding the savings from the system, total monthly savings and monthly average solar irradiance were plotted by Fig.10. Total monthly savings (€) were calculated as 6.73; 7.77; 9.61; 10.71; 11.93; 13.4; 13.77; 11.98; 10.69; 7.93; 7.27 and 5.97 from January to December, respectively. Annual saving per module is reached as 117.83 €.

4. Conclusions

In the present study, annual performance covering electrical, overall energy and savings of PVT system integrated with natural zeolite was evaluated. Performance parameters were calculated hourly and averaged. In hourly calculations, correlations obtained from the experiments were used and real meteorological data and annual values on an hourly basis were estimated. Monthly average hourly values of energy efficiency, electrical power, overall produced energy and the savings were estimated. Remarkable results of the study could be listed as below:

- Average daily solar irradiance values were found as 2.11; 3.38; 4.73; 5.22; 5.98; 7.20; 7.53; 6.44; 5.11; 3.44; 2.85; 2.13 from January to December, respectively for Usak province where the experiments were carried out.
- Average overall energy efficiency values were found as 0.56; 0.54; 0.49; 0.49; 0.48; 0.46; 0.45; 0.46; 0.50; 0.53; 0.54 and 0.56 from January to December, respectively for natural zeolite based PVT systems. Considering that the laboratory efficiency of the PV module in the PVT system is 15%, the thermal efficiency of the natural zeolite PVT is remarkable.
- Monthly average hourly produced electrical power values per module were calculated as 106.8; 126.7; 143.4; 148.5; 145.2; 168.6; 161.9; 158.9; 148.2; 123.0; 121.4 and 105.9 W from January to December, respectively.
- Monthly average overall produced energy values (kWh) were determined as 73.93; 85.39; 105.59; 117.66; 131.15; 148.04; 151.35; 131.67; 117.50; 87.12; 79.90 and 65.59 from January to December, respectively.
- Annual total overall energy produced by the PVT system integrated with natural zeolite was found as 1294.88 kWh/year per module.
- Annual saving per module is reached as 117.83 € per module. With the acceptance of the system cost of 942.8 €, simple payback period is approximately 8 years. This payback time, which is found on a single module, will surely decrease at higher installed powers.

Considering the industry, transportation and housing sectors, the highest share in energy consumption belongs to the buildings. According to research by the International Energy Agency (IEA), it has been revealed that in many IEA member countries, energy use in buildings accounts for over 40% of primary energy consumption [19, 20]. Energy use in buildings has increased significantly over the past few decades due to population growth, economic growth and an increase in quality of life. However, as of 2019, the Covid-19 pandemic, quarantine processes and remote work applications, which have been on the agenda of the world, increase the energy consumed in the buildings far above these values. Increasing demand for energy supply has led to even faster development of low energy technologies for building applications, with global warming due to CO₂ emissions from the use of non-renewable energy sources.

PVT systems based on natural zeolites could offer a very promising option to supply electrical and thermal energy demand of the building. It is hoped that this study could help to understand the performance of natural zeolite based PVT systems for building applications.

Acknowledgment

This study has been supported by The Scientific and Technological Research Council of Turkey (TUBITAK) within 214M615 research project.

References

- [1] Huang BJ, Yang PE, Lin YP, Lin BY, Chen HJ, Lai RC. Solar cell junction temperature measurement of PV module. *Solar Energy*, 2011; 85:388-92. <https://doi.org/10.1016/j.solener.2010.11.006>
- [2] Kandilli C. A comparative study on the energetic- exergetic and economical performance of a photovoltaic thermal system (PVT), *Research on Engineering Structures and Materials*, 2019; 5:1, 75-89. <https://doi.org/10.17515/resm2019.90en0117>
- [3] Huang MJ, Eames PC. Norton B. Phase change materials for limiting temperature rise in building-integrated photovoltaics. *Solar Energy*, 2006; 80, 1121-1130. <https://doi.org/10.1016/j.solener.2005.10.006>
- [4] Huang MJ, Eames PC. Norton B., Hewitt NJ. Natural convection in an internally finned phase change material heat sink for the thermal management of photovoltaics. *Solar Energy Materials and Solar Cells*, 2011; 95, 1598-1603. <https://doi.org/10.1016/j.solmat.2011.01.008>
- [5] Park J, Kim T, Leigh SB. Application of a phase-change material to improve the electrical performance of vertical-building-added photovoltaics considering the annual weather conditions. *Solar Energy*, 2014, 105, 561-574. <https://doi.org/10.1016/j.solener.2014.04.020>
- [6] Ho CJ, Chou WL, Lai CM. Application of a water-saturated MEPCM-PV for reducing winter chilling damage on aqua farms. *Solar Energy*, 2014; 108:135-145. <https://doi.org/10.1016/j.solener.2014.07.006>
- [7] Hasan A, McCormack SJ, Huang MJ, Norton B. Characterization of phase change materials for thermal control of photovoltaics using Differential Scanning Calorimetry and Temperature History Method. *Energy Conversion and Management*;2014, 81, 322-329. <https://doi.org/10.1016/j.enconman.2014.02.042>
- [8] Ho CJ, Tanuwijava AO, Lai CM. Thermal and electrical performance of a BIPV integrated with a microencapsulated phase change material layer. *Energy and Buildings*, 2012; 50:331-8. <https://doi.org/10.1016/j.enbuild.2012.04.003>
- [9] Lin W, Ma Z, Sohel MI, Cooper P. Development and evaluation of a ceiling ventilation system enhanced by solar photovoltaic thermal collectors and phase change materials. *Energy Conversion and Management*, 2014; 88, 218-230. <https://doi.org/10.1016/j.enconman.2014.08.019>
- [10] Gurmen Ozcelik T. Investigation of glycerol-Ni(NO₃)₂·6H₂O /perlite composites as form stable phase change materials. *Research on Engineering Structures and Materials*, 2020; 6(2): 141-151. <https://doi.org/10.17515/resm2019.122ma0221>
- [11] Kandilli C. Energy, exergy, and economical analyses of a photovoltaic thermal system integrated with the natural zeolites for heat management. *International Journal of Energy Research*. 2019;43, 4670-4685. <https://doi.org/10.1002/er.4605>
- [12] <https://www.mgm.gov.tr/veridegerlendirme/il-ve-ilceler-istatistik.aspx?m=USAK> [access, 07.07.2020]
- [13] Negis F. Zeolite Based Composites In Energy Storage, Izmir Institute of Technology The Graduate School, Master of Science in Materials Science and Engineering, 1999.
- [14] Brottier L, Bennacer R, Thermal performance analysis of 28 PVT solar domestic hot water installations in Western Europe, *Renewable Energy* (2020). <https://doi.org/10.18086/swc.2019.05.01>
- [15] Xu L, Ji J, Zhaomeng KL, Xu LT, Huang S. Annual analysis of a multi-functional BIPV/T solar wall system in typical cities of China, *Energy* , 2020;197:117098 <https://doi.org/10.1016/j.energy.2020.117098>

- [16] Gholami H, Røstvik HN. Economic analysis of BIPV systems as a building envelope material for building skins in Europe. *Energy*, 2020; 204: 117931 <https://doi.org/10.1016/j.energy.2020.117931>
- [17] Duffie JA, Beckman WA. *Solar Engineering of Thermal Processes*, Wiley-Interscience Publication, Second Edition, 1991, pp.25-32
- [18] <https://www.mta.gov.tr/v3.0/bilgi-merkezi/zeolit> [access, 07.07.2020]
- [19] IEA. Modernising building energy codes to secure our global energy future. International Energy Agency <www.iea.org> [accessed 4.11.13].
- [20] <https://www.ase.org/initiatives/buildings#:~:text=Energy%20Use%20in%20Buildings,other%20sector%20of%20the%20economy> . [10.07.2020]



Acid modified graphite felt cathode electrode for low temperature H₂/Br₂ redox flow battery

Büşranur Duman^a, Berker Fıçıcılar^{*b}

Department of Chemical Engineering, Ondokuz Mayıs University, Samsun, Turkey

Article Info

Abstract

Article history:

Received 17 Dec 2019

Revised 07 May 2020

Accepted 09 May 2020

Keywords:

Hydrogen-bromine flow battery;

Graphite felt;

Surface modification

In this study, the performance of a modified PAN based graphite felt, an alternative electrode for cathode, was investigated for hydrogen/bromine flow battery. In these experiments, carbon paper was used as porous transport layer in the anode and graphite felt (GF) was used as the catalytically active electrode in the cathode. Graphite felt electrode used for cathode is also used in industry as thermal insulation material. The cathode kinetics of this relatively low-cost material was increased by acidic modification and used in flow battery cathode electrodes. To create functional groups on the cathode electrode, acidic surface modification of the graphite felt was carried out with H₂SO₄ and HNO₃ acid pairs with a volumetric ratio of V_{H₂SO₄} / V_{HNO₃} = 3:1. XRD and SEM analyzes were used for physical characterization of the modified graphite felt electrodes. Single cell potentiostatic polarization and power curves of the hydrogen/bromine flow battery were obtained to elucidate the effect of cathode graphite felt surface modification. In this study, comparison tests were performed for pristine graphite felt and modified graphite felt. The maximum powers detected from the single cell flow battery formed by pristine graphite felt and modified graphite felt cathode electrodes are 0.32 W/cm² (0.65V) and 0.40 W/cm² (0.65V), respectively. In flow battery tests, this 25% power increase in similar voltage values may be attributed to the improvement of the weak electrochemical properties of the graphite felt electrode by acidic modification.

© 2020MIM Research Group. All rights reserved.

1. Introduction

Energy storage technologies are vital for the practical use of renewable energy. Among the renewable energy resources, wind and solar powers are widely used energy sources and they are considered as intermittent systems [1]. In order to increase the energy efficiency, these renewable energy sources must be coupled with a suitable energy storage system. One such promising technology for the electrical energy storage is flow batteries. Flow batteries can store electrical energy with high efficiency and for a longer period. Among all flow batteries, H₂/Br₂ flow batteries are considered as a promising battery technology due to their rapid cathode kinetics. In a typical low temperature H₂/Br₂ flow battery system operating on discharge mode, hydrogen gas (anolyte) is fed to the anode side and protons are formed by hydrogen oxidation reaction in the catalytic region. Then, protons are transported through the solid polymer membrane to the cathode. In the cathode side,

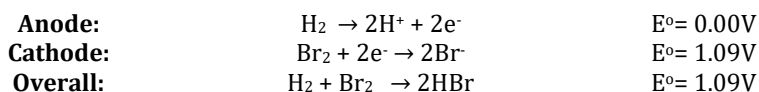
*Corresponding author: berker.ficicilar@omu.edu.tr

^a orcid.org/0000-0001-7761-1510; ^b orcid.org/0000-0003-3882-1691

DOI: <http://dx.doi.org/10.17515/resm2019.170en1217>

Res. Eng. Struct. Mat. Vol. 6 Iss. 4 (2020) 375-384

liquid bromine solution (catholyte) is reduced to bromide ions at the cathode and form hydrobromic acid. The half-cell reactions for the H₂/Br₂ 2 flow battery system are (discharge mode):



One of the major advantages of this battery is that hydrogen and bromine are relatively inexpensive chemicals. Since the system contains bromine with its toxic and corrosive structure, overall flow battery design should be bromine and hydrobromic acid tolerant. Although the hydrogen-bromine flow battery has higher electrode kinetics compared to other popular flow battery systems, Br⁻, Br³⁻ or Br⁵⁻ ions in the cathode can pass through the anode and poison the platinum-containing catalyst in the anode (crossover), thus reducing the flow battery performance [2]. Bromine-based ions which pass through the membrane to the anode catalyst also hinder efficient operation of the battery at 0.6 V and below. Therefore, Preventing/reducing the passage of bromine based ions as a result of crossover through the conventional membrane (Nafion® 212) is an important problem to be solved for the hydrogen-bromine flow battery. In addition, expensive catalysts and electrodes that can be used on the cathode side increase the cost considerably. Cost-effective catalysts and porous transport layers may be used to reduce overall cost of the cell. For the Hydrogen/Bromine flow battery reactions precious metallic or bimetallic catalysts such as Pt/C and Pt-Ru/C or Rh_xS_y and Rh_xS_y/C may be used [3-6]. In addition, the bromine reduction reaction (BRR) can also be catalyzed by only carbon structures. Besides its role as porous transport layer (PTL), it is well documented in the literature that carbon paper, carbon cloth, carbon felt, and graphite felt also act as active catalyst for BRR. Graphite felt (GF) can be produced from polyacrylonitrile (PAN) by high temperature carbonization and graphitization process. Graphite felt is widely used as PTL in redox flow batteries due to its low cost (ca. \$70/m²), good electrical conductivity, high surface area with a porous structure (470-600 m²g⁻¹), and stable mechanical and chemical properties [7-9]. The performance of the hydrogen-bromine redox flow battery can be improved by applying surface modification processes to low-cost carbon-based electrodes.

The graphite felt used in this study is a low cost material generally used for thermal insulation at high temperature. On the other hand, poor electrochemical properties of the graphite felt limit the performance of the hydrogen-bromine flow battery system [10]. To enhance H₂/Br₂ flow battery system performance, one strategy may be to increase electrochemical catalytic activity. One way to achieve this goal is to increase functional oxygen groups within the electrode structure. Supply of functional oxygen groups over the surface of graphite felt leads to an increase in surface wettability and this results in an improved electrical conductivity. There are various effective techniques for surface modification in the literature such as thermal modification [11], acidic modification [12], electrochemical oxidation [10], nitrogen modification [13], metal modification [14], thermo-chemical modification oxygen plasma treatment and gamma-ray irradiation [15]. Among these methods, the acidic modification process increases the electrochemical activity by increasing the oxygen-containing functional groups on the graphite felt surface, as well as increasing the active reaction area due to acid corrosion. In a study by W. Zang et al. for vanadium redox flow batteries, it was observed that acid treatment applied to the graphite felt for VO²⁺/VO₂⁺ reaction increased the wettability of the graphite felt and decreased the resistance during charge transfer [16].

In this study, it was aimed to improve the kinetics of bromine reduction reaction in cathode by modifying the surface of low-cost graphite felt by acidic treatment. The effect of

modified graphite felt electrodes and carbon loading on H₂/Br₂ redox flow battery performance were investigated and compared with pristine graphite felt electrodes.

2. Materials and method

In this study, the electrode surface of graphite felt was modified with sulfuric acid and nitric acid. Then, anode and cathode catalysts were prepared. The catalysts were loaded over the electrodes in the specified proportions and pressed with a hot press by inserting a commercial membrane between them. Finally, steady state potentiostatic performance tests were performed with an electronic load in a single-cell (5 cm², interdigitated flow field) hydrogen bromine flow battery system.

2.1. Acidic modification

5 mm thick graphite felt (SGL[®] Carbon, Sigratherm GFA5) was cut to obtain an electro active area of about 5 cm² (2.2cm x 2.2cm). The graphite felt electrode was sonicated in anhydrous ethanol (%99, Sigma-Aldrich[®]) for 30 min. to remove impurities. Then, GF electrode was washed with de-ionized water. GF electrode was dried in an oven at 100°C for 5 h. Sulfuric acid (%98, Sigma-Aldrich[®]) and nitric acid (%69, Merck[®]) pairs were used for acidic oxidation. 2M sulfuric acid and 2M nitric acid were used in the acidic treatment process. The acid mixture was prepared so that the volumetric ratio was kept at about V_{H₂SO₄}/V_{HNO₃}= 3. GF electrode was oxidized in a sealed 100 mL Teflon-lined flask containing 40 mL of mixed acid solution at 80°C. The oxidized electrode was first washed with deionized water, and then sonicated with deionized water for 30 min. Electrode was dried in oven at 100°C for 5h.

2.2 MEA Preparation

Anode electrode was prepared by using commercial Pt/C catalyst (67 wt% from Tanaka Kikinzoku Kogyo) onto the porous transport layer (PTL) with a loading amount of 0.4 mg Pt/cm². On the cathode side, commercial carbon black (Vulcan XC-72, Cabot[®]) was used as catalyst. The electrode was prepared by loading the catalyst in an amount of 0.4 mg C/cm² onto PTL. In the anode and cathode catalyst loading process, the catalyst solution was prepared using catalyst (Pt/C or C), Nafion solution (15%, Ion Power[®]), deionized water and 2-propanol (Sigma-Aldrich[®]). The ratio of catalyst to Nafion solution was kept at around 7: 3 by weight. After the catalyst solution was homogenized using an ultrasonic bath, the catalyst ink was loaded onto the PTL by conventional brushing method. The membrane electrode assembly (MEA) structure is formed by placing a solid polymer membrane between the anode and cathode electrodes. Nafion-212 (DuPont[®]), a commercial solid polymer electrolyte membrane, was used without pretreatment for the proton exchange. Electrodes were prepared using porous carbon paper (SGL[®] Carbon, GDL 25BC) in the anode and graphite felt (SGL[®] Carbon, Sigratherm GFA5) in the cathode as the porous transport layer. MEA structure was prepared with a hot press at 135 °C and 5 bar for about 4 min.

2.3 Physical characterization

Surface morphology analyses of the samples were performed using scanning electron microscopy (SEM) with an acceleration voltage of 10kV (JEOL, JSM-7001F). The X-Ray diffraction (Rigaku, SmartLab) analysis of the samples was conducted using the Cu-K α 1 source with a screening angle of 2-90°, and scanning speed of 2° min⁻¹. X-ray photoelectron spectroscopy (XPS) (Specs-Flex XPS) was used to examine the functional groups over the surface of the electrodes.

2.4 Single cell performance tests of hydrogen-bromine redox flow battery

Hydrogen/Bromine redox flow battery polarization tests were performed using a single cell test system with an active area of 5 cm². Bipolar plates produced from graphite have interdigitated flow field design. Gold-plated electrolytic copper current collectors are used to record the potential and current. 200 micron thick Teflon gaskets are used at the anode and cathode to seal the cell. A torque wrench is used to compress the cell with a torque of 4 N.m per bolt. In the electrode preparation stage, SGL GDL 25BC and Sigratherm GFA5 graphite felt were used as porous transport layer at the anode and cathode respectively. For all anode electrodes, 0.4 mg/cm² (67% Pt/C) catalyst was loaded onto the SGL 25BC gas diffusion layer. In this study, no humidification was performed on the anode side. Hydrogen flow rate was set to 0.1L min⁻¹.

At the cathode, a mixture of 1 M HBr (500 mL) and 1 M (500 mL) Br₂ was circulated at a volumetric rate of 50 mL/min with a peristaltic pump (Watson Marlow E323). All experiments were conducted at room temperature (~25°C). Under the same conditions, 25BC/Nafion-212/Pristine GF, 25BC/Nafion-212/Modified GF, and 25BC/Nafion-212/Modified GF + Vulcan XC-72 MEAs were used in the cell and single cell hydrogen-bromine flow battery performance tests were performed. While the battery was operated in discharge mode, current values were recorded at the potentiostatic steady-state potentials at 0.05 V intervals starting from the open circuit voltage with an electronic load (Maynuo® M9714).

3. Result and Discussion

XRD patterns of pristine graphite felt and graphite felt after acidic modification are shown in Fig. 1. The most prominent peaks in all pristine and modified graphite felt samples are the peaks corresponding to planes (002) (JCPDS: No. 75-1261) and (100) at 26.4° and 44.6° respectively [17,18].

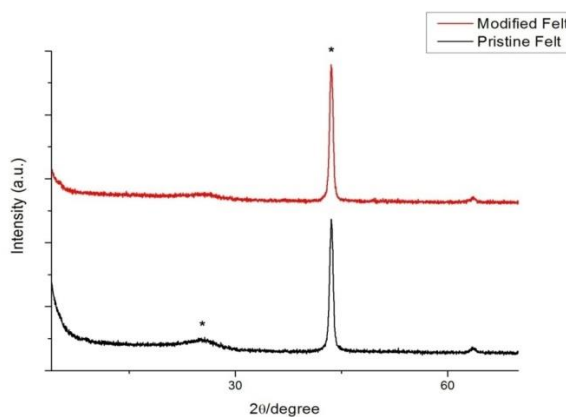


Fig. 1 XRD patterns of electrodes

The characteristic diffraction of the graphite felt in the (002) and (100) planes indicates that the graphite felt is partially oxidized. When the diffraction densities of pristine GF and modified GF were compared, it was found that the diffraction density decreased after oxidation due to acidic treatment. This reduction in diffraction intensity is generally attributed to defects formed in the structure after oxidation process. These structural defects may also be seen from the SEM micrographs given in Fig. 2. Diffraction peaks weaken as these defects in the structure cause partial irregularity of the reflection planes

in the crystal plane [17,19]. Type and content of the functional groups are validated by XPS analysis and this may explain and confirm the reduced diffraction intensity observed in XRD patterns. Pristine GF and modified GF surface morphologies are given in Figure 2. When SEM micrographs are analyzed, it is seen that acidic modification causes a change in the surface of graphite felt fibers. The fibers in the structure of the graphite felt are about 10 μm thick.

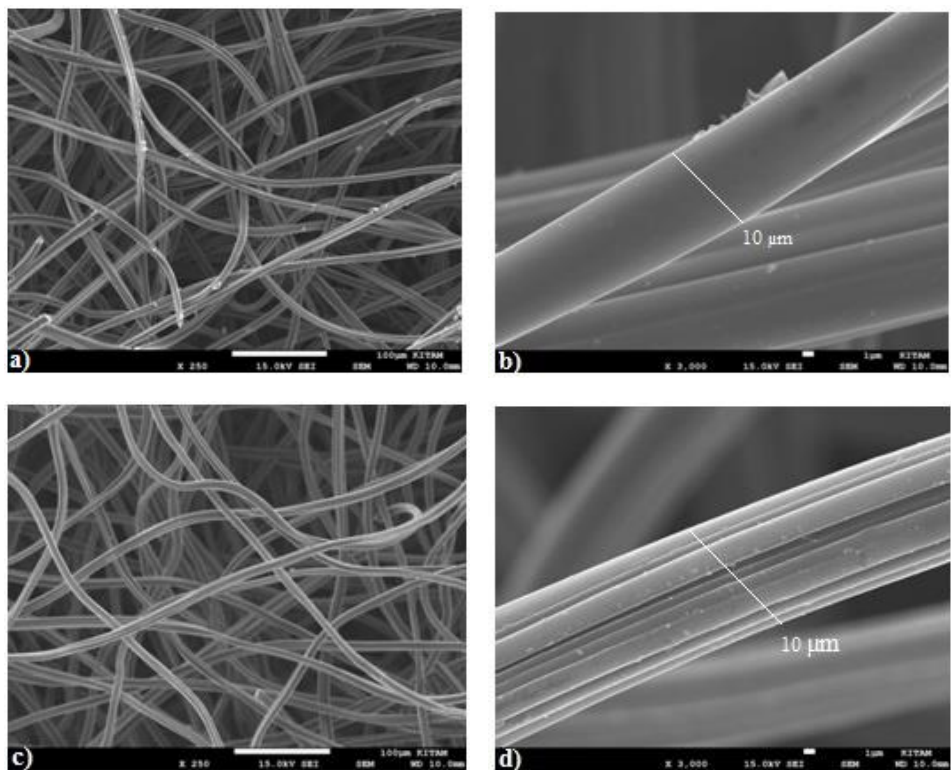


Fig. 2 SEM micrographs of cathode electrodes for a-b) Pristine graphite felt, and c-d) Modified graphite felt

When the SEM micrograph is examined, it is seen that there are micro changes due to oxidation on the graphite felt surface. Acidic modification caused roughness on the surface of graphite felt fibers. Surface oxygen groups and roughness can be controlled by altering the concentration of the acid pair to values higher than 2M used in this study. These defects caused by modification especially created small cavities on the fiber structure and increased the surface area of the graphite felt.

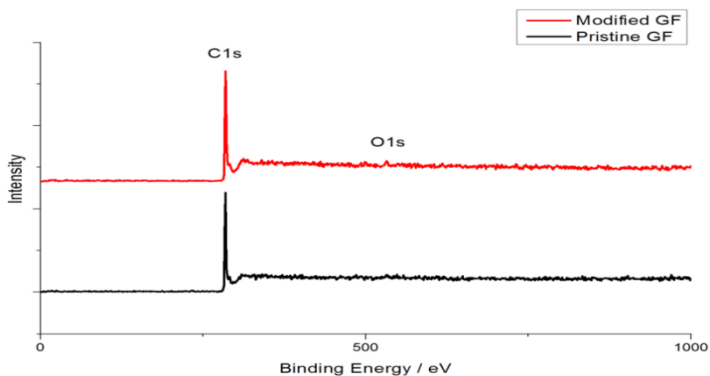


Fig.3 XPS surveys of pristine and modified graphite felts

XPS survey spectra given in Fig. 3, indicates C1s and O1s binding energy values were centered at 284.7 eV and 532.0 eV respectively. Considering XPS results, no significant impurities were found on the graphite felt surface. In addition, oxygen containing functional groups were detected with the XPS analysis. XPS data were used to fit a curve by peak deconvolution method to get C1s and O1s spectra of the pristine and modified graphite felt samples. C1s and O1s spectrums of the graphite felt samples are given in Fig. 4. Spectra are calibrated according to the binding energy of the carbon at 284.7 eV. The functional group contents on the surface of the samples are listed in Table 1. Table 1 confirmed the increase of oxygen-containing functional groups on the electrode surface after modification.

Table 1. XPS curve fit data for the surface functional groups

Sample	C1s			O1s	
	C=C	C-C	C-O	C=O	C-OH
Pristine GF	33.70	16.31	14.93	18.54	16.52
Modified GF	31.21	18.78	18.20	31.81	

As it can be seen from Fig. 4, C1s peak positions and binding energies were attributed to C-C (287.7 eV), C=C (283.75 eV, 285.1 eV) functional groups [20]. Considering oxygen containing carbon bonds, C-O (532.0 eV, 533.4 eV, 533.4 eV), C=O (530.0 eV, 531.2 eV, 531.4 eV, 531.7 eV), -OH (532.7 eV) functional groups are detected for O1s peak [21-23].

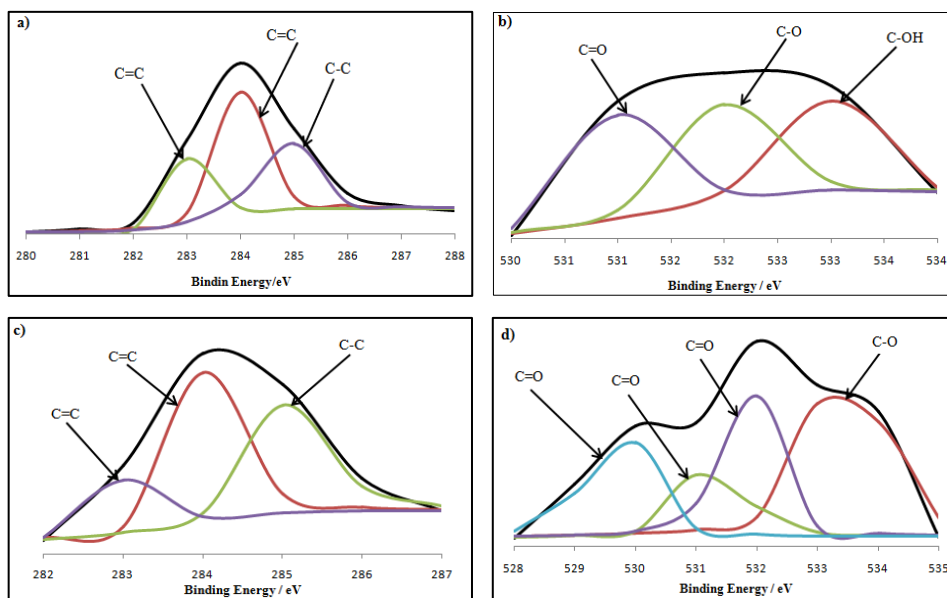


Fig. 4 XPS curve-fit for C1s and O1s spectra of cathode electrodes, pristine GF (a and b), modified GF (c and d)

The hydrogen/bromine redox flow battery performances of pristine GF and modified GF were performed by an electronic load using a single cell with an active area of 5 cm² and bipolar plates having interdigitated flow channel architecture. Polarization and power curve data of the flow battery system for different cathode electrodes are presented in Figure 5. Table 2 lists the maximum current and power density for the tested electrodes. As Fig. 5 and Table 2 are examined, the increase in cell performance due to acidic modification is clearly observed. It may be suggested to use more concentrated acid pair solution to modify the surface electrodes to get even better performance results. On the other hand, a slight increase in hydrogen/bromine redox flow battery performance was detected when a typical carbon black (Vulcan XC72) was loaded (0.4 mg C/cm²) into the cathode electrode, especially when the fuel cell is operated at higher current densities. Optimal cathode carbon black loading values over the surface of the modified graphite felt will be reported in a future study.

The maximum power densities obtained from Pristine GF, modified GF and modified GF + Vulcan XC-72 cathode electrodes are 0.32 W cm², 0.38 W cm², and 0.40 W cm², for the potentials of 0.65 V, 0.75 V, and 0.65 V respectively.

As the flow battery is operated at lower potentials (< 0.6 V), considerable performance loss is observed. This phenomenon may result from the crossover of species such as Br⁻ Br³⁻ [8]. This performance loss may be prevented with a proper electrolyte to minimize crossover and as well as with a better anode catalyst (bromine tolerant HOR catalyst).

Considering the low current density region, it is observed that the performance of pristine GF is low. Losses in this region can be attributed to catalytic activation. Relatively higher performance of the modified GF in the low current density region may result from the increased kinetics of bromine reduction after acidic modification and consequently to an increase in catalytic activity.

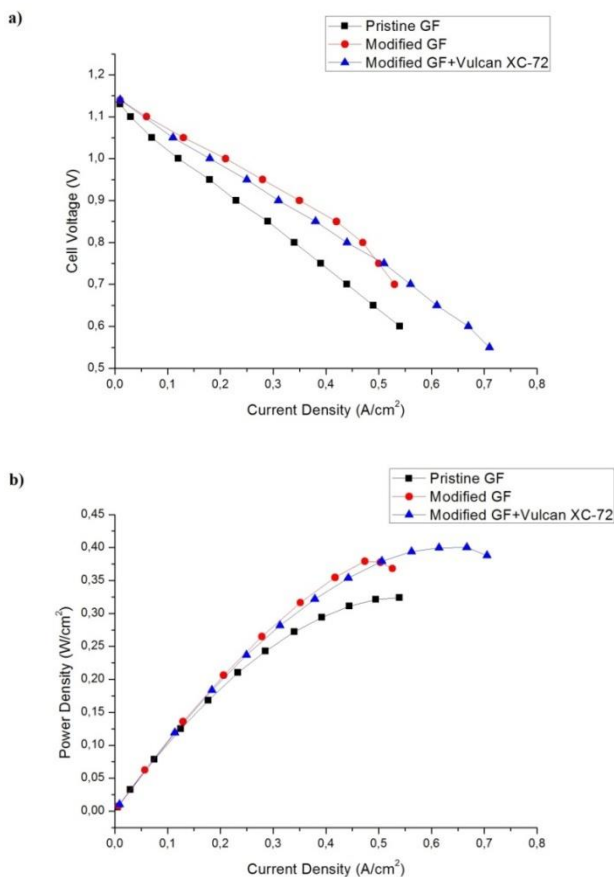


Fig. 5 Single cell H₂/Br₂ redox flow battery performance for different cathode electrodes at 25 °C a) polarization curve and b) power curve

Table 2. Current and maximum power densities for the prepared cathode electrodes

Anode	Cathode	Cell Voltage (V)	Current Density (A/cm ²)	Power Density (W/cm ²)
SGL 25BC	Pristine GF	0.65	0.49	0.32
SGL 25BC	Modified GF	0.75	0.50	0.38
SGL 25BC	Modified GF+Vulcan XC-72	0.65	0.61	0.40

4. Conclusion

In this study, it was aimed to increase the performance and decrease the cost of the hydrogen-bromine flow cell system. For this purpose, low-cost modification processes were applied to the graphite felt electrode used in the cathode. The surface of the graphite felt used as an electrode in the cathode can be modified by methods such as thermal, electrochemical or acidic treatment. Acidic treatment, which is fast and low cost, provided the desired improvement in this work. Compared with the modified and carbon loaded

cathode electrodes, pristine graphite felt performance was observed to be lower. Selected graphite felt is generally used for insulation purposes (e.g. high temperature oven applications) and this felt has a relatively lower surface area. As a result of the surface modification of cathode graphite felt with acidic treatment, flow battery performance increased with the increase in electrocatalysis for bromine reduction reaction. The use of graphite felt electrode as a bromine cathode electrode in the hydrogen-bromine flow battery system significantly reduces the cost of the battery. XPS results indicate the presence of oxygen-containing functional groups on the electrode surface and confirm the increase of these groups after acidic modification. The electrochemical activity of the electrode has been significantly improved by increasing the defects created on the graphite felt electrode surface and the active functional groups containing oxygen. The electroactive reaction area provided by the functional groups enhanced the hydrogen/bromine flow battery performance by accelerating the electrode kinetics of the reduction reaction at the cathode. In addition, functional groups on the surface reduced resistance on the cathode electrode formed during charge transfer, and accordingly, single cell flow battery performance was improved. In order to further improve the electrocatalysis of cathode electrode, it is recommended to determine the appropriate carbon types (e.g. carbon blacks, ordered mesoporous carbons, CNTs, etc.) and the optimum carbon loading amounts for graphite felt electrodes modified with concentrated acid pairs.

Acknowledgement

The authors are very grateful for XPS analysis carried out at DAYTAM laboratory. We also would like to thank Black Sea Advanced Technology Research and Application Center (KITAM) at OMU for XRD and SEM analysis. Authors are also grateful for the partial support provided by TÜBİTAK project through grant number 2209-A.

References

- [1] Yang Z, Zhang J, Kintner-Meyer MCW, Lu X, et al. Electrochemical Energy Storage for Green Grid. *Chemical Reviews* 2011; 111: 3577-3613. <https://doi.org/10.1021/cr100290v>
- [2] Hugo YA, Kout W, Sikkema F, Borneman Z, Nijmeijer K. Performance mapping of cation exchange membranes for hydrogen-bromine flow batteries for energy storage. *Journal of Membrane Science* 2018; 566:406-414. <https://doi.org/10.1016/j.memsci.2018.09.006>
- [3] Choa KT, Ridgwaya P, Weber AZ, Haussener S, Battaglia V, et al. High Performance Hydrogen/Bromine Redox Flow Battery for Grid-Scale Energy Storage. *Journal of The Electrochemical Society* 2012; 159(11): A1806-A1815. <https://doi.org/10.1149/2.018211jes>
- [4] Livshits V, Ulus A, Peled E. High-power H₂/Br₂ fuel cell. *Electrochemistry Communications* 2006; 8: 1358-1362. <https://doi.org/10.1016/j.elecom.2006.06.021>
- [5] Van Nguyen T, Kreutzer H, Yarlagadda V, McFarland E, Singh N. HER/HOR catalysts for the H₂-Br₂ fuel cell system. *ECS Transactions* 2013; 53(7): 75-81. <https://doi.org/10.1149/05307.0075ecst>
- [6] Ivanovskaya A, Singh N, Liu RF, Kreutzer H, Baltrusaitis J, et al. Transition Metal Sulfide Hydrogen Evolution Catalysts for Hydrobromic Acid Electrolysis. *American Chemical Society* 2013; 29(1): 480-492. <https://doi.org/10.1021/la3032489>
- [7] Viswanathan V, Crawford A, Stephenson D, Kim S, Wang W, et al. Cost and performance model for redox flow batteries. *Journal of Power Sources* 2014; 247: 1040-1051. <https://doi.org/10.1016/j.jpowsour.2012.12.023>

- [8] Yarlagadda V, Dowd, Jr. R.P, Park J.W, Pintauro P. N, Nguyen T.V. A Comprehensive Study of an Acid-Based Reversible H₂-Br₂ Fuel Cell System. *Journal of The Electrochemical Society* 2015; 162 (8): F919-F926. <https://doi.org/10.1149/2.1041508jes>
- [9] Kaneko H, Nozaki K, Wada Y, Aoki T, Negishi A, et al. Vanadium redox reactions and carbon electrodes for vanadium redox flow battery. *Electrochimica Acta* 1991; 36(7): 1191-1196. [https://doi.org/10.1016/0013-4686\(91\)85108-J](https://doi.org/10.1016/0013-4686(91)85108-J)
- [10] Li X, Huang K, Liu S, Tan N, Chen L. " Characteristics of graphite felt electrode electrochemically oxidized for vanadium redox battery application" *Transactions of Nonferrous Metals Society of China*, vol.17, no. 1, pp. 195-199, 2007. [https://doi.org/10.1016/S1003-6326\(07\)60071-5](https://doi.org/10.1016/S1003-6326(07)60071-5)
- [11] Sun B, Skyllas-Kazacos M. Chemical modification of graphite electrode materials for vanadium redox flow battery application-part II. Acid treatments. *Electrochimica Acta* 1992; 37(13): 2459-2465. [https://doi.org/10.1016/0013-4686\(92\)87084-D](https://doi.org/10.1016/0013-4686(92)87084-D)
- [12] Sun B, Skyllas-Kazacos M. Modification of graphite electrode materials for vanadium redox flow battery application-I. Thermal treatment. *Electrochimica Acta* 1992; 37(7): 1253-1260. [https://doi.org/10.1016/0013-4686\(92\)85064-R](https://doi.org/10.1016/0013-4686(92)85064-R)
- [13] Wu T, Huang K, Liu S, Zhuang S, Fang D, Li S, Su A. Hydrothermal ammoniated treatment of PAN-graphite felt for vanadium redox flow battery. *Journal of Solid State Electrochemistry* 2012;16(2):579-585. <https://doi.org/10.1007/s10008-011-1383-y>
- [14] Wu X, Xu H, Lu L, Zhao H, Fu J, Shen Y, Dong, Y. PbO₂-modified graphite felt as the positive electrode for an all-vanadium redox flow battery. *Journal of Power Sources* 2014;250:274-278. <https://doi.org/10.1016/j.jpowsour.2013.11.021>
- [15] Kim KJ, Kim YJ, Kim JH, Park MS. The effects of surface modification on carbon felt electrodes for use in vanadium redox flow batteries. *Materials Chemistry and Physics* 2011; 131 (1-2): 547-553. <https://doi.org/10.1016/j.matchemphys.2011.10.022>
- [16] Zhang W, Xi J, Li, Z, Zhou, H, Liu, L, et al. Electrochemical activation of graphite felt electrode for VO₂⁺/VO₂⁺ redox couple application. *Electrochimica Acta* 2013; 89: 429-435. <https://doi.org/10.1016/j.electacta.2012.11.072>
- [17] Li W, Liu J, Yan C. Graphite-graphite oxide composite electrode for vanadium redox flow battery. *Electrochimica Acta* 2011;56(14):5290-5294. <https://doi.org/10.1016/j.electacta.2011.02.083>
- [18] Ye JS, Cui HF, Liu X, Lim T.M, Zhang WD, Sheu FS. Preparation and characterization of aligned carbon nanotube-ruthenium oxide nanocomposites for supercapacitors. *Small* 2005;1(5):560-565. <https://doi.org/10.1002/sml.200400137>
- [19] Yue L, Li W, Sun F, Zhao L, Xing L. Highly hydroxylated carbon fibres as electrode materials of all-vanadium redox flow battery. *Carbon* 2010; 48(11): 3079-3090. <https://doi.org/10.1016/j.carbon.2010.04.044>
- [20] He H, Jiang Y, Meng W, Jiang F, Zhou H, et al. HF/H₂O₂ treated graphite felt as the positive electrode for vanadium redox flow battery. *Applied Surface Science* 2017; 423: 111-118. <https://doi.org/10.1016/j.apsusc.2017.06.154>
- [21] Zhong RS, Qin YH, Niu DF, Tian J-W, Xin-Sheng Zhang XS, et al. Effect of carbon nanofiber surface functional groups on oxygen reduction in alkaline solution. *Journal of Power Sources* 2013; 276 (225): 192-199. <https://doi.org/10.1016/j.jpowsour.2012.10.043>
- [22] Kabtamu DM, Chen JY, Chang YC, Wang CH. Water-activated graphite felt as a high-performance electrode for vanadium redox flow batteries. *Journal of Power Sources* 2017; 341: 270-279. <https://doi.org/10.1016/j.jpowsour.2016.12.004>
- [23] Shibagaki K, Motojima S. Surface properties of carbon micro-coils oxidized by a low concentration of oxygen gas. *Carbon* 2000; 38: 2087-2093. [https://doi.org/10.1016/S0008-6223\(00\)00065-8](https://doi.org/10.1016/S0008-6223(00)00065-8)



Research Article

Design charts for linear elastic pavements

Abdullah Fettahoglu*^{1,a}, Mehmet Cemal Genes^{2,b}

¹Department of Civil Engineering, Usak University, Usak, Turkey.

²Department of Civil Engineering, Eastern Mediterranean University, Famagusta, Northern Cyprus Turkish Republic

Article Info

Article history:

Received 10 Dec 2019

Revised 24 Apr 2020

Accepted 05 May 2020

Keywords:

Linear elastic pavements;
Design charts;
Hand calculations;
Concrete pavements

Abstract

Deformation of most pavements is practically inelastic. Thus, the exact calculation of pavement deformation often requires use of a damage evaluation law to characterize the stress-strain relationship mathematically. Asphalt, polymer, and reinforced concrete are all examples of such pavements. However, concrete pavements without reinforcement are generally assumed to behave linear elastic. Concrete pavements without reinforcement are used sometimes as permanent pavements with dowels such as airport apron pavement, but sometimes they are used as temporary pavements during the mobilization or initial phases of new construction projects as well. When used as permanent pavements, their design is performed similar to rigid pavements, which has international acceptance by highway engineers, or by finite element analysis. When used as temporary works during the mobilization phase, or when a road is urgently required on a construction site, their design is often problematic, because advanced highway design or finite element analysis might be momentarily unavailable. A rapid, conservative, and reliable hand calculation method for temporary concrete pavements without reinforcement is therefore required. In this study, design charts are provided to allow hand calculations of temporary concrete pavements. In addition, a numerical example is solved to illustrate the use of derived charts. The effects of certain parameters on the stress behavior of concrete pavements are also investigated.

© 2020 MIM Research Group. All rights reserved.

1. Introduction

In this study, some hand calculation charts are derived to enable quick and conservative design of linear elastic rigid pavements, such as temporary concrete pavements without reinforcement, of the type frequently used at the mobilization phase of construction. The design of a linear elastic rigid pavement is based on the maximum stress developed in the pavement itself and in its base. The source of these stresses relates of course to the heaviest wheel load on the top of the pavement. As a result, the maximum stress develops in the contact zone between the wheel and the pavement. The first stage is therefore the calculation of this maximum (or peak) stress, which is necessary to determine the required strength of pavement. At the same time, the stresses induced by the wheel load are dispersed through the thickness of the pavement, and a reduced, dispersed stress is then obtained at the base of the pavement. The maximum value of these vertical stresses must be less than the bearing capacity of the soil. This leads to the second consideration, which is the calculation of the maximum stress at the pavement base in order to determine the pavement thickness required. Starting from the beginning, Groenendijk (1998), Pottinger (1992), Tielking (1994), De Beer (1996), and Jong (2007) [1-5] investigated the contact stress developed between the wheel and the pavement. Of all, Groenendijk [1] derived formulas to determine the maximum stress between the wheel and the pavement, also referred to as the "Footprint pressure" in the literature. This subject is

*Corresponding author: abdullah.fettahoglu@usak.edu.tr

^a orcid.org/0000-0001-5759-1794; ^b orcid.org/0000-0002-9052-7361

DOI: <https://dx.doi.org/10.17515/resm2019.169st1210>

Res. Eng. Struct. Mat. Vol. 6 Iss. 4 (2020) 385-409

discussed in the first section after the introduction. The issue of the second maximum stress at the base of the pavement is evaluated in the subsequent sections. A 45° stress dispersal in the direction of pavement thickness is generally assumed to calculate that second stress. This assumption is applied in many engineering calculations, and is also supported in the literature [6]. However, it is still unclear whether this proposed 45° stress dispersion and the uniform vertical stress distribution is appropriate. Unfortunately, stress dispersal through pavement thickness is less investigated by the researchers. Among that less data available in the literature, Li et al. [7] investigated the stresses in the pavement for the safety of underground pipelines. They studied a range of parameters in an attempt to reduce the stress in the base of the pavement and in the top of the infrastructure pipe and revealed that the burial depth of the pipes should be increased to provide acceptable levels of stress above the pipes. Therefore, the aim of the present study is to investigate the magnitude and shape of the dispersed wheel load in the pavement base. First, a finite element (FE) model of the pavement and wheel model is developed using ANSYS [8]. Second, pavement is assumed to be linear elastic and wheel is assumed conservatively to be a static load rather than a moving load. Third, the possible parameters that could affect the value and shape of the dispersed load at the pavement base are selected. Fourth, the shape and value of the dispersed load at the pavement base is determined by means of FE analysis. Fifth, verification of the FE model is undertaken using Boussinesq equation. Sixth, the effects of the parameters on the dispersed stress are assessed, and finally design charts are derived to estimate the magnitude and shape of the dispersed stress at the pavement base.

2. Determination of the Contact Stress (First Maximum Stress) between the Wheel and Pavement

Groenendijk [1] performed extensive research on the contact stresses between tyre and pavement. He measured the footprint pressure using the Vehicle-Road Surface Pressure Transducer Array (VRSPATA) system. VRSPATA measures the stresses between relatively slow moving free-rolling tyres and the road surface. It measures the vertical stresses, as well as longitudinal and lateral shear stresses. Groenendijk [1] also performed tests for various combinations of wheel load, tyre inflation pressure, and wheel speed for two wide-base single tyres (type C) [6]. With the VRSPATA system, it is possible to measure stress patterns at the interface between tyre and pavement. Fig. 1 shows an example of a measured 3D stress pattern for a 425/65 R22.5 tyre [6] for an inflation pressure of 0.7 MPa, loaded at 100 kN, moving at 0.3 m/s [5].

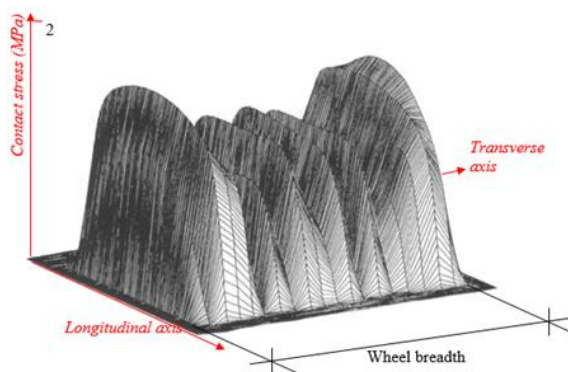


Fig. 1 Example of measuring contact stress using VRSPATA [5].

Groenendijk formulated the following conclusions from his research [5]:

1. The wheel load mainly governs the stresses at the tyre edges, while the tyre pressure governs the stresses at the center of the tyre.
2. The tyre/pavement contact area can be modeled as a rectangle as wide as the tyre tread area, and with a length that depends on the load and inflation pressure. For stress modeling, this area should be divided into three zones in the transverse direction: Two edge zones each 20% of the tyre width, and one middle zone covering the remaining 60%.
3. The vertical contact stresses may be treated as uniformly distributed loads, but generally with different values for the middle and edge zones.

Groenendijk derived equations for the footprint (contact) stress:

$$\sigma_{z,ave,middle} = 422 - 1.20 \cdot F + 4.60 \cdot 10^{-3} \cdot F \cdot p + 0.322 \cdot p + 8.60 \cdot v \quad (1)$$

$$\sigma_{z,ave,edge} = 85.5 + 9.25 \cdot F + 0.290 \cdot p + 1.29 \cdot v \quad (2)$$

where:

F = Wheel load (kN)

p = Tyre inflation pressure (kPa)

v = Wheel speed (m/s)

$\sigma_{z,ave,middle}$ = Average vertical contact stress over the middle 60% of the tyre width (breadth) and the full tyre footprint length (kPa)

$\sigma_{z,ave,edge}$ = Average vertical contact stress over the edges 2 x 20% of the tyre width and the full tyre footprint length (kPa).

Using the load, the inflation pressure, and the velocity, contact stresses can be calculated. The equations derived by Groenendijk are based on measurements for wide-base tyres (type C). It may be assumed that these equations are also valid for the single (type A) and the double (type B) tyres, because these tyre types differ only slightly from the super single (type C) [5]. Fortunately, Jong [5] proved in his thesis that the wheel contact areas given in EC3 [6] are acceptable by means of the Lintrack measurement system used by Jong [5].

If the velocity and tyre pressure in Eq.1 and Eq.2 are conservatively replaced with 0 m/s and 0.9 kPa respectively, Eq.3 and Eq.4 are obtained as follows:

$$\sigma_{z,ave,middle} = 422.3 - 1.2042 \cdot F \quad (3)$$

$$\sigma_{z,ave,edge} = 85.761 + 9.25 \cdot F \quad (4)$$

The variation of contact stresses on edge and middle zones depending on wheel load (N) are given in Fig. 2 using Eq.3 and Eq.4.

Because the method derived here is aimed for the design of temporary concrete pavements, the lowest strength of the pavement can be conservatively taken as 10 MPa (lean concrete). In this case a wheel load or a set of adjacent wheel loads must be 1000 kN to overcome the strength of the concrete and crack the pavement, which is almost impossible in practice. As a result, there is no need to consider the contact stress between the pavement and the wheel in the design of temporary concrete pavements without reinforcement.

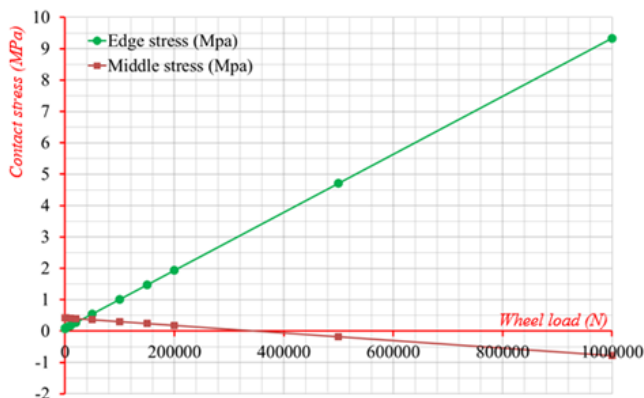


Fig. 2 Variation of edge and middle zone contact stresses according to Eq.3 and Eq.4.

3. Determination of the Dispersed Stress (Second Maximum Stress) at the Pavement Base

The second maximum stress depends on the dispersed stresses at the pavement base, because the wheel-induced stresses might not just be due to a single wheel, but instead, due to a set of wheels. Therefore, it is considered here both the distribution and the maximum of the vertical stress value at the pavement base. If the pavement design is to be performed for more than one wheel, where the wheels are adjacent and interact with each other, the maximum vertical stress can be determined from the superposition of both of the dispersed stresses at the pavement base. To determine the distribution of the dispersed stress at the pavement base, it is first necessary to select the potential parameters influencing the dispersed stress. The effect of these parameters on this distribution is then analyzed separately. Finally, charts are derived for the calculation of the single-wheel load-induced dispersed stress.

3.1. Definition of Parameters

The intended parameters shown in Fig. 3 are wheel load (W_L), wheel breadth (W_B), elasticity modulus (E_P), Poisson ratio (ν_P), width (W_P) and thickness of pavement (T_P). All parameters and their default values are shown in Fig. 3. Finite element (FE) analysis, termed “reference” analysis, is performed using the default (or initial) parameter values. Then, a single parameter is changed, while keeping the others constant. In this way, the effect of this single parameter on the magnitude and distribution of the dispersed stresses is evaluated.

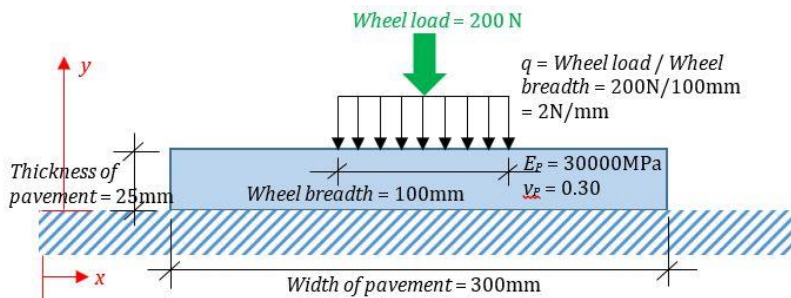


Fig. 3 Default (or initial) values of parameters

3.2. FE Model

The reference FE analysis is used to find the distribution of the dispersed stress at the base of the pavement and additionally in the intermediate layers. The FE model employed in this study is fully restrained against translation and rotation on the pavement base. The number of elements and nodes used in the FE model are 8748 and 9100 respectively. A four-node FE, referred to as SHELL181 in the ANSYS [8] documentation, is used to generate the FE model. Results of the reference FE-analysis, depending on the default values of the parameters are shown in Fig. 4, in which the dispersed stresses (See Fig. 3 for the definitions of the x and y -axes) are given for the top, intermediate, and base layers of pavement. The intermediate layers are selected for various elevations (Values of y in Fig. 4 relate to the y -axis shown in Fig. 3, not the depths of pavement layers).

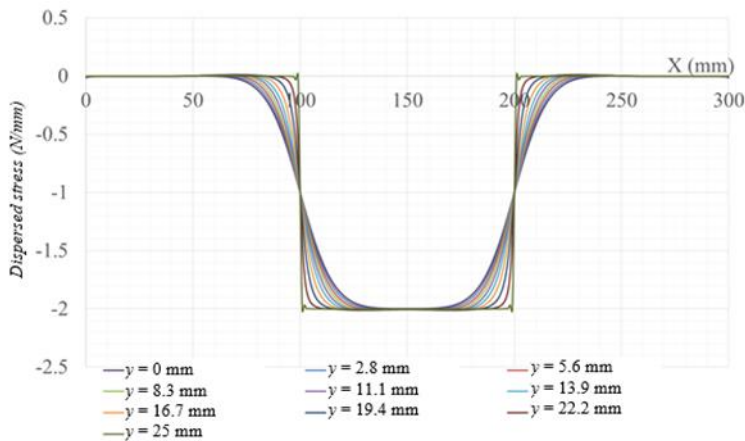


Fig. 4 Dispersed stresses at the top, intermediate layers, and base of pavement.

3.3. Comparison of FE-Analysis with Boussinesq Equation

A comparison of FE-analysis with the Boussinesq equation [9] is performed to determine the dispersed stress at intermediate depths in a semi-infinite continuum (semi-space), as shown in Fig. 5.

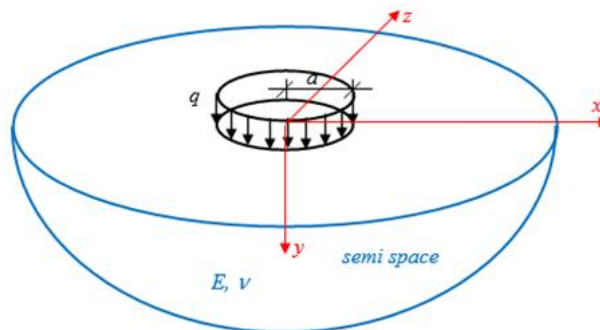


Figure 5. Semi-space with uniform load

The Boussinesq equation for dispersed stress (σ_y) provided by Timoshenko and Goodier [9] is

given below.

$$\sigma_y = q \cdot \left[-1 + \frac{y^3}{(a^2 + y^2)^{1.5}} \right] \tag{5}$$

Using Eq.5 in conjunction with FE results allows comparison between the FE and Boussinesq solutions as shown in Figs. 6a and b.

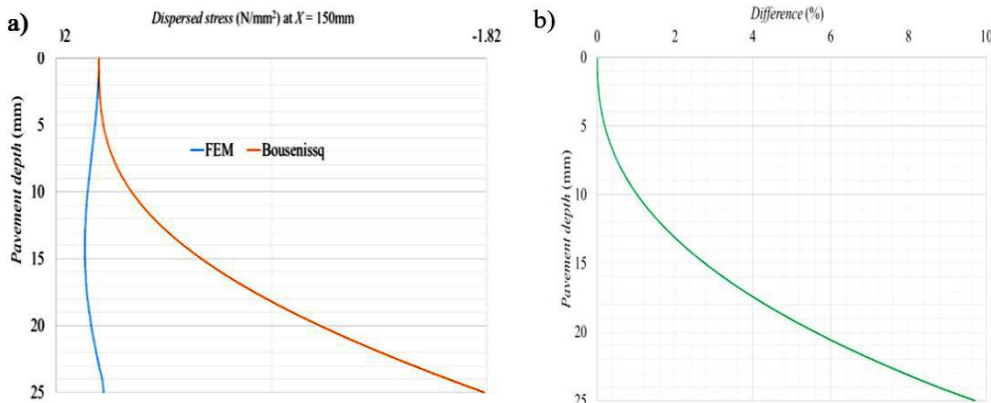


Fig. 6. a) Comparison of FE solution with Boussinesq solution b) Difference (%) between FE solution and Boussinesq solution

The difference between the two solutions is less than 1% up to a depth of 10 mm measured from the top of the pavement. Between 10 mm and almost 20 mm depth, the difference is not more than 5%. The maximum difference is approximately 9.5% at the base of the pavement (25 mm depth). Because the Boussinesq solution is developed for semi-space and results provided by it are more appropriate for small depths, the FE approach used is assumed satisfactory for the intended parameter study.

3.4. Assumed Distribution of Dispersed Load

As seen from Fig. 4 and Fig. 7, the distribution of the dispersed stress at the base of the pavement can be assumed to be trapezoidal, characterized using the dimensions f , e_1 and e_2 given in Fig. 7.

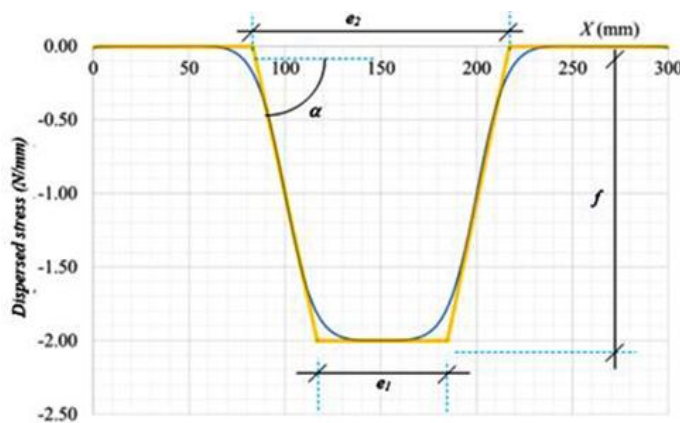


Fig. 7 Distribution of dispersed stress at the pavement base

Here f , e_1 and e_2 are clearly functions of *wheel load*, *wheel breadth*, *elasticity modulus*, *Poisson ratio*, *width*, and *thickness* of pavement. Using the default values of parameters f , e_1 and e_2 results

in -2 N/mm (-1.9979 ≈ -2), 69 mm, and 134 mm respectively, which are derived from Fig. 7 using the Fortran code provided in Appendix 1. The measured value of α is 3.52°. However, f , e_1 and e_2 are not totally independent and the area of the trapezoid must be equal to the wheel load as per Eq.6.

$$\text{Wheel load} = -f \cdot \left(\frac{e_1 + e_2}{2} \right) \tag{6}$$

If Eq.6 is not satisfied, it is advisable to keep f and e_1 the same and justify the value of e_2 , such that Eq.6 holds. In the subsequent sections, f , e_1 and e_2 are obtained as functions of the intended research parameters.

3.5. Effect of Parameters on f , e_1 and e_2

3.5.1 Effect of Elasticity Modulus on f , e_1 and e_2

The elasticity modulus of the pavement (E_p) is varied from 1 GPa to 100 GPa, while other parameter values are kept constant. From the results shown in Fig. 8, it is apparent that f , e_1 and e_2 are independent on the elasticity modulus of the pavement. The values of dispersed stress in Fig. 8 in all scenarios are so same, that all three curves for $E = 1, 10$ and 100 GPa are overlapped.

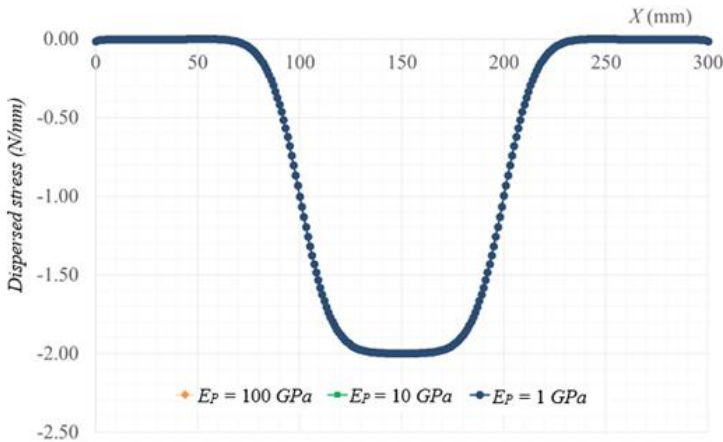


Fig. 8 Dispersed stress at the base of pavement for varying elasticity modulus

3.5.2 Effect of Poisson's Ratio on f , e_1 and e_2

As seen in Fig. 9, the effect of Poisson's ratio on f , e_1 and e_2 is very slight, that it can readily be ignored as a parameter affecting on f , e_1 or e_2 .

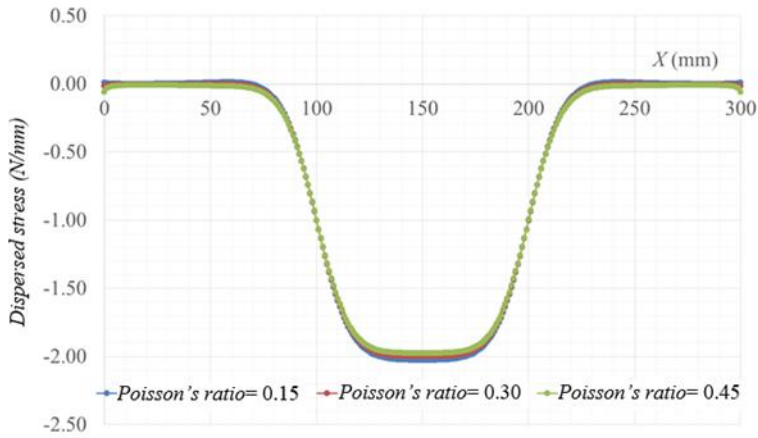


Fig. 9 Dispersed stress at the base of pavement for varying Poisson's ratio.

3.5.3 Effect of Pavement Width on f , e_1 and e_2

The effect of pavement width on f , e_1 and e_2 is shown in Fig. 10. It is clear that widths less than 150 mm lead to stress concentrations at the two edges of the pavement. At the same time, varying the width from 150 mm to 400 mm has almost no effect on the magnitude and distribution of the dispersed stress. Two conclusions may be drawn from Fig. 10: First, the width of the pavement should be at least one and a half times the *wheel breadth* ($Pavement\ width \geq 1.5 \cdot Wheel\ breadth$). Second, varying the width above this value has no effect on f , e_1 and e_2 .

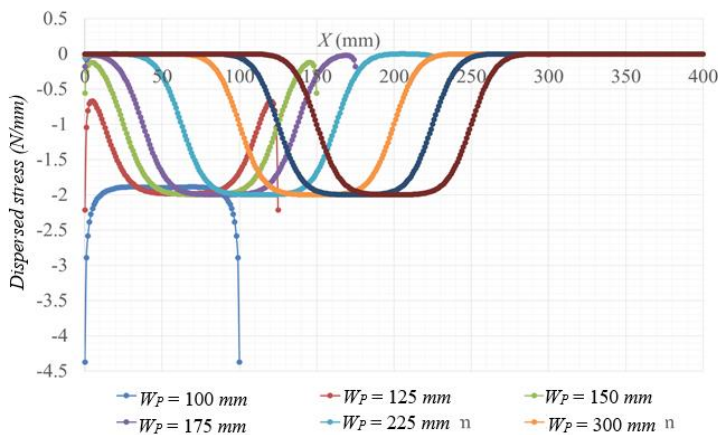


Fig. 10 Dispersed stress depending on the pavement width.

3.5.4 Effect of Wheel Load on f , e_1 and e_2

The variation of the dispersed load depending on wheel load is given in Fig. 11. e_1 and e_2 derived from the curves are all the same, meaning that the wheel load has no effect on them.

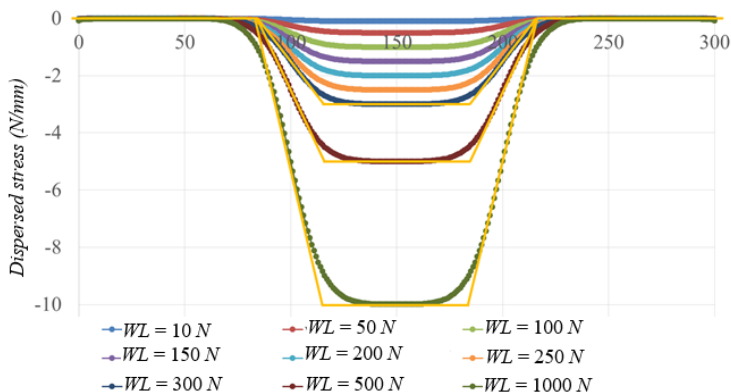


Fig. 11 Dispersed stress depending on the value of wheel load.

Nonetheless, f is directly proportional to the wheel load as given in Fig. 12, if the effect of the remaining parameters (*wheel breadth and pavement thickness*) are ignored.

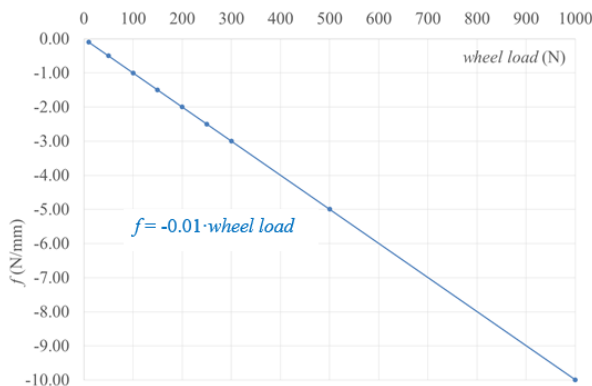


Fig. 12 Variation of f depending on wheel load.

According to Fig. 12, the relationship between f and wheel load is linear and may be described as follows:

$$f = -0.01 \cdot \text{wheel load} \tag{7a}$$

Here, it is apparent that the coefficient (0.01) comes from the ratio, *Wheel Load / Wheel Breadth* for all the cases. For instance, for $W_L = 700$ kN, f derived from Fig. 12 is 7 N/mm, which is equal to 700 N/100 mm = 7 N/mm. As a result, f is described using Eq.7b below.

$$f = -(W_L/W_B) \cdot g(WB, T_P) \tag{7b}$$

where g is a function of *wheel breadth* and *pavement thickness*.

3.5.5 Effect of Pavement Thickness on f , e_1 and e_2

As seen in Fig.13, f , e_1 and e_2 , all vary depending on thickness of pavement (T_P).

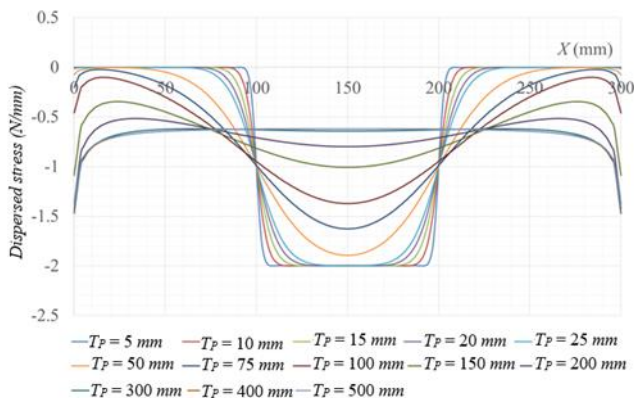


Figure 13. Dispersed stress depending on pavement thickness.

Fig. 13 indicates that starting from a thickness of 75 mm and up to 150 mm, some stress concentrations develop at the edges, but in sufficiently small numbers to allow them to be ignored. However, above a thickness of 150 mm the number of stress concentrations becomes critical, making an applied methodology to derive f , e_1 and e_2 extremely difficult.

3.5.6 Effect of Wheel Breadth on f , e_1 and e_2

Effect of wheel breadth on f , e_1 and e_2 is shown in Fig. 14, from which it is deduced that they are all functions of the parameter *wheel breadth* as in the case of *pavement thickness*.

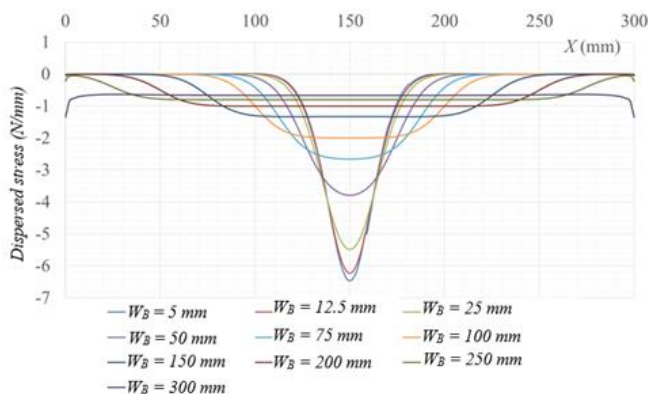


Fig. 14 Dispersed stress depending on *wheel breadth*.

3.5.7 Widening Width of Pavement to Eliminate Stress Concentrations

If the width of pavement is increased to 2 m, the stress concentrations are reduced significantly, however they cannot be completely eliminated especially at extreme pavement thicknesses such as 1000 mm, as observed from Fig. 15. Therefore, the pavement width of 2 m is taken as the default value of the parameter *pavement width* in the FE analyses hereafter. Since the shoulder width in highways is at least 1 m, and half the wheel spacing is approximately 1 m, the default *pavement length* = 1 m + 1 m = 2 m is seen to be realistic.

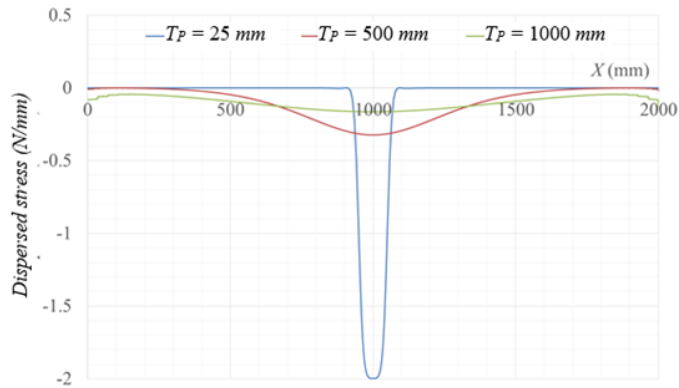


Fig.15 Stress concentrations developed for different pavement thicknesses, when pavement width is 2 m.

3.6. Assumed Distribution of Dispersed Load

Because f depends solely on wheel load, pavement thickness and wheel breadth, the function of f is derived based on these three variables. It has already been shown that f is directly proportional to wheel load according to Eq.7a, the variation of f depending on wheel breadth and pavement thickness for a wheel load of 1 N is shown in the chart given in Fig. 15. Data tables for Figs. 16, 17 and 18 are given in Appendix 2.

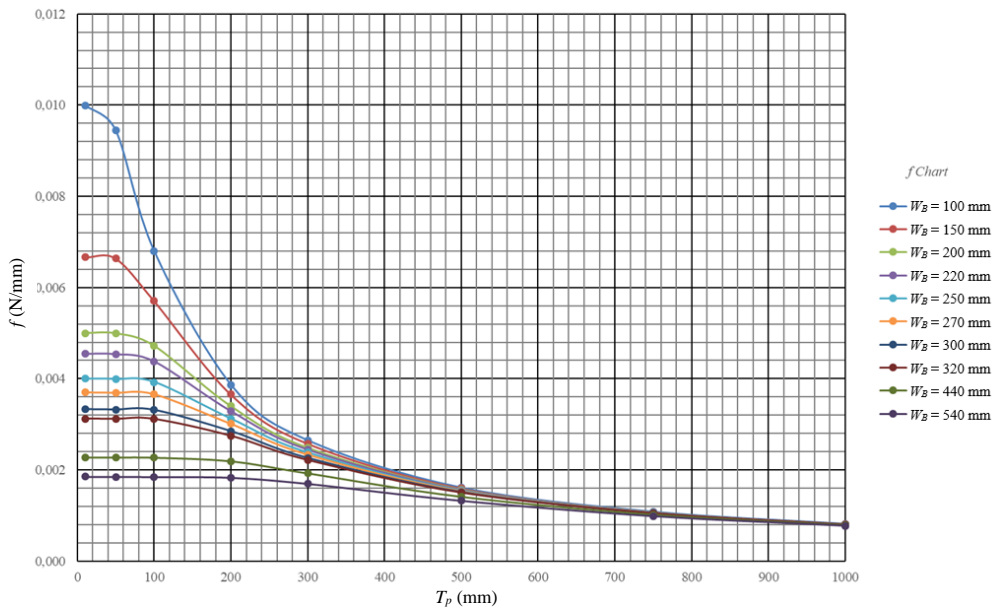


Fig. 16 f depending on pavement thickness (T_P) and wheel breadth (W_B) for wheel load = 1N.

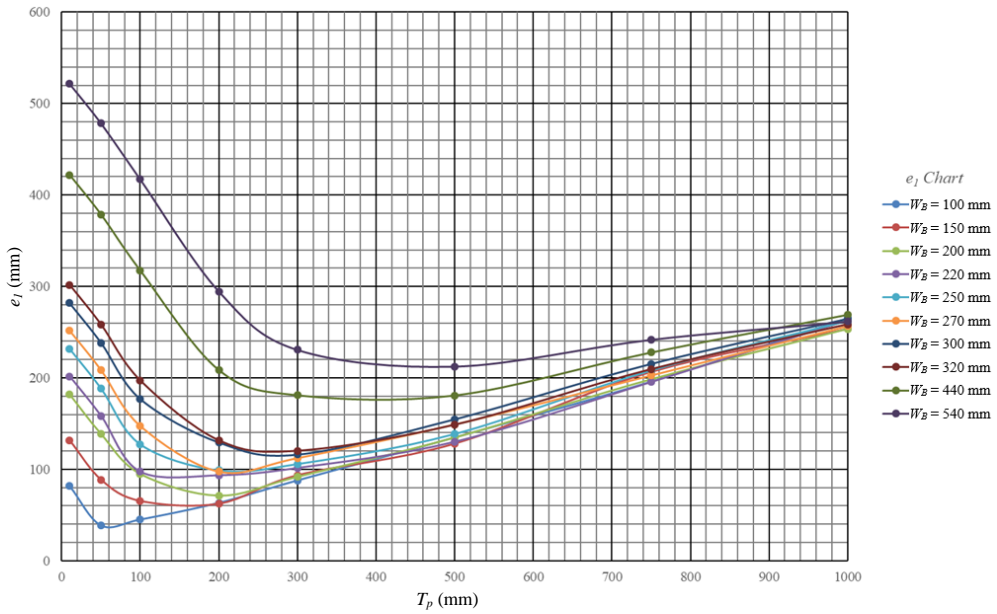


Fig. 17 Recommended values of e_1 .

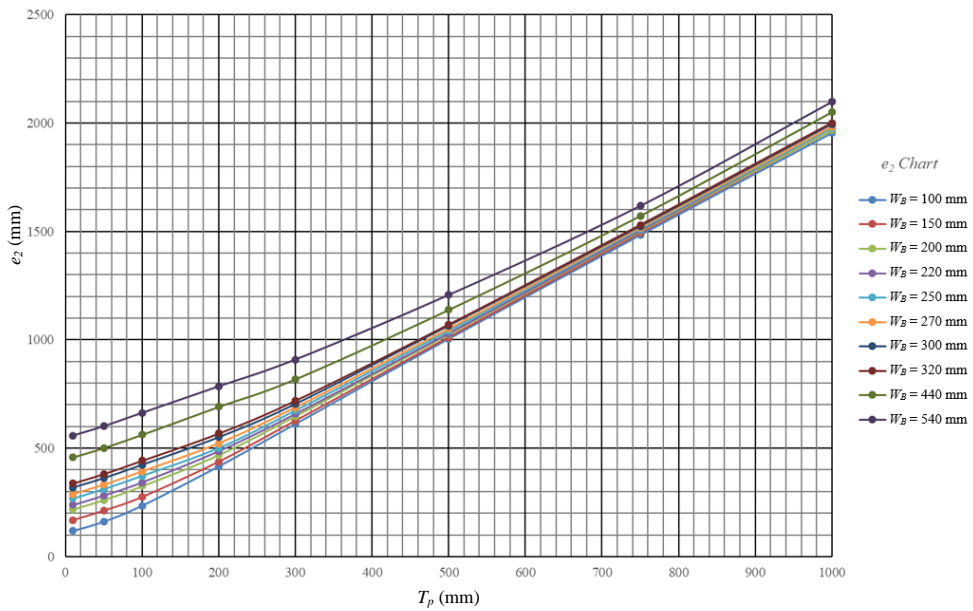


Fig. 18 Recommended values of e_2 .

4. A Numerical Example

The method derived here is a simple hand calculation method for designing concrete (or linear elastic) pavements under axle loads. The method allows rapid and easy calculation of pavement stresses and is especially recommended for engineers unable to perform a FE-analysis due to a lack of time and software. In this section, a truck load is first selected complying with EC 3 [6] and then the magnitude and distribution of stresses developed at the bottom of the pavement are calculated using the charts derived in this study. Finally, results obtained are compared with the results obtained from an FE-analysis.

4.1. Problem Description

According to EC 3 [6] heavy truck vehicles are defined by,

1. Axle number and distance between axles (Table 1, column 1 and 2),
2. Frequently used axle load (Table 1, column 3),
3. Wheel load area and transverse distance between wheel loads (Column 4 of Table 1 and Table 2).

Table 1 Group of frequently used heavy truck vehicles [6].

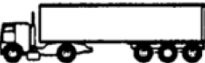
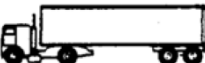
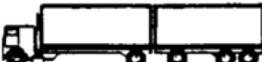
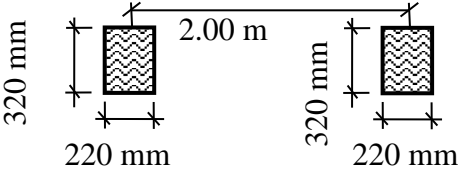
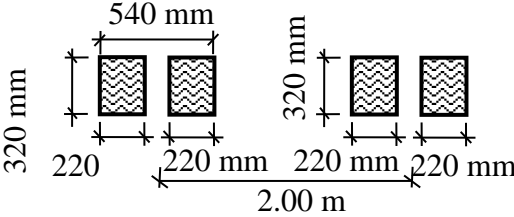
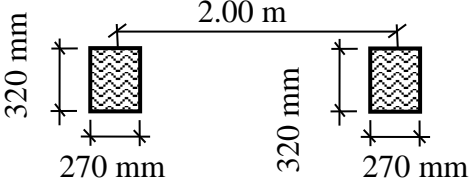
1	2	3	4
<i>View of heavy truck vehicle</i>	<i>Axle distance (m)</i>	<i>Frequently used axle load (kN)</i>	<i>Tyre type</i>
	4.50	90	A
		190	B
	4.20	80	A
	1.30	140	B
		140	B
	3.20	90	A
	5.20	180	B
	1.30	120	C
	1.30	120	C
	3.40	90	A
	6.00	190	B
	1.80	140	B
		140	B
	4.80	90	A
	3.60	180	B
	4.40	120	C
	1.30	110	C
		110	C

Table 2 Wheel contact areas [6].

<i>Type of wheel area and axle</i>	<i>Geometry</i>
A	 <p>Diagram A shows two square wheel contact areas. Each square has a height of 320 mm and a width of 220 mm. The two squares are positioned 2.00 m apart, measured from the center of one square to the center of the other.</p>
B	 <p>Diagram B shows four square wheel contact areas. Each square has a height of 320 mm and a width of 220 mm. They are arranged in two pairs. The total width of the two squares in each pair is 540 mm. The distance between the center of the first square and the center of the last square is 2.00 m.</p>
C	 <p>Diagram C shows two square wheel contact areas. Each square has a height of 320 mm and a width of 270 mm. The two squares are positioned 2.00 m apart, measured from the center of one square to the center of the other.</p>

From Table 1, the heavy vehicle in the second row is selected as the truck design load. A C10 concrete pavement without reinforcement is selected. The soil strength is taken as 300 kPa. The thickness of the concrete pavement must be justified to keep the maximum stress at the pavement base lower than the soil strength.

4.2. Solution

The truck loads in the longitudinal and transverse directions are given in Figs. 19, 20, and 21.

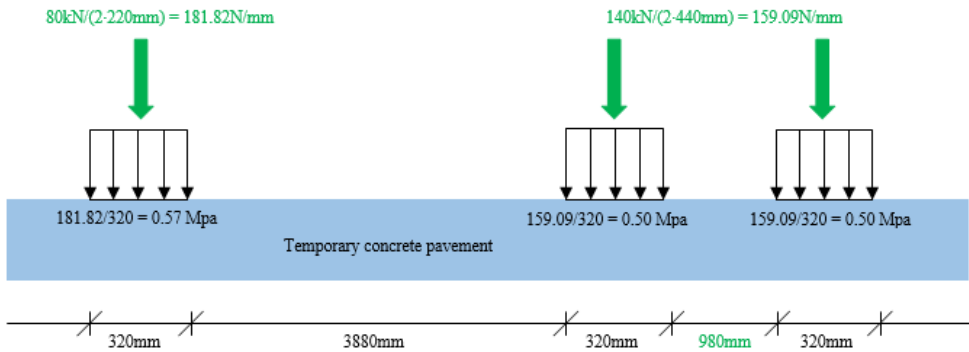


Fig. 19 Truck loading in longitudinal direction.

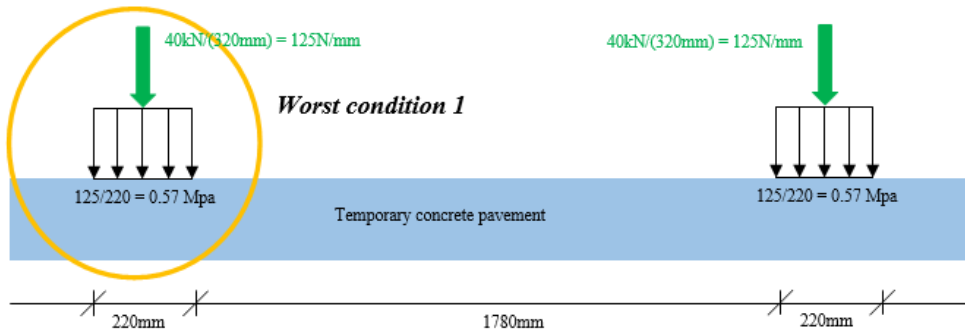


Fig. 20 Truck loading in transverse (1st axle) direction.

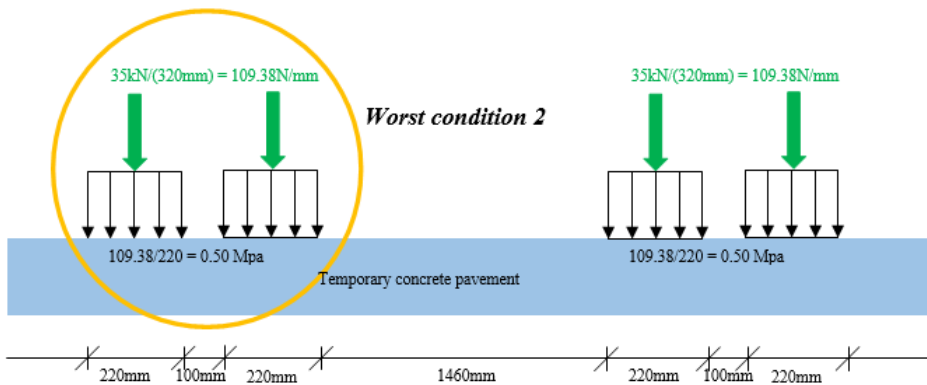


Fig. 21 Truck loading in transverse (2nd or 3rd axle) direction.

4.2.1 Solution of Worst Condition 1

Because the worst condition 1 is composed of a single wheel load, only the maximum stress at the pavement base (f) is calculated, and the shape of dispersed stress (e_1 and e_2) is not required. From Fig. 16, f is determined as follows:

$$125 \cdot f (\text{wheel breadth} = 220 \text{ mm, pavement thickness} = ?) \leq \text{soil strength} = 0.30 \text{ MPa}$$

$$f (\text{wheel breadth} = 220 \text{ mm, pavement thickness} = ?) \leq 0.0024 \text{ MPa}$$

From Figure 16, $f = 0.0022 \text{ MPa} \rightarrow T_p = 320 \text{ mm} = 32 \text{ cm}$

4.2.2 Solution of Worst Condition 2

Because the worst condition 2 is composed of two wheel loads, two maximum stresses at the bottom of the pavement (f) are calculated together with their corresponding distributions (e_1 and e_2 for both). However, since the two wheels are similar, this problem reduces to finding one set of f , e_1 and e_2 and the maximum stress in the interaction zone. From Fig. 16, f is determined as follows:

$$109.38 \cdot f (\text{wheel breadth} = 220 \text{ mm, pavement thickness} = ?) \leq \text{soil strength} = 0.30 \text{ MPa}$$

$$f \leq 0.0027 \text{ MPa}$$

From Fig. 16 $f = 0.0023 \text{ MPa} \rightarrow T_p = 240 \text{ mm} = 24 \text{ cm}$ and

$$109.38 \cdot f = 109.38 \cdot 0.0023 = 0.25 \text{ MPa} \leq \text{soil strength} = 0.30 \text{ MPa}$$

From Fig. 17, e_1 is determined as follows:

$$e_1 (\text{wheel breadth} = 220 \text{ mm, pavement thickness} = 240 \text{ mm}) = 95 \text{ mm}$$

From Fig. 18, e_2 is determined as follows:

$$e_2 (\text{wheel breadth} = 220 \text{ mm, pavement thickness} = 240 \text{ mm}) = 550 \text{ mm}$$

According to these values Fig. 22 is drawn and the maximum stress in the interaction zone is calculated. Using Fig. 22 and the affinity between triangles, this maximum stress is calculated as:

$$2 \cdot 0.0012 \text{ MPa} = 0.0024 \text{ MPa}$$

Since

Max. stress for 1 N = $0.0024 \text{ MPa} < 0.0027 \text{ MPa}$ or,

Max. stress for two adjacent wheel load (Worst condition 2) =

$$= 109.38 \cdot 0.0024 = 0.26 \text{ MPa} < 0.30 \text{ MPa} = \text{Soil strength},$$

24 cm pavement thickness is enough under selected truck loading.

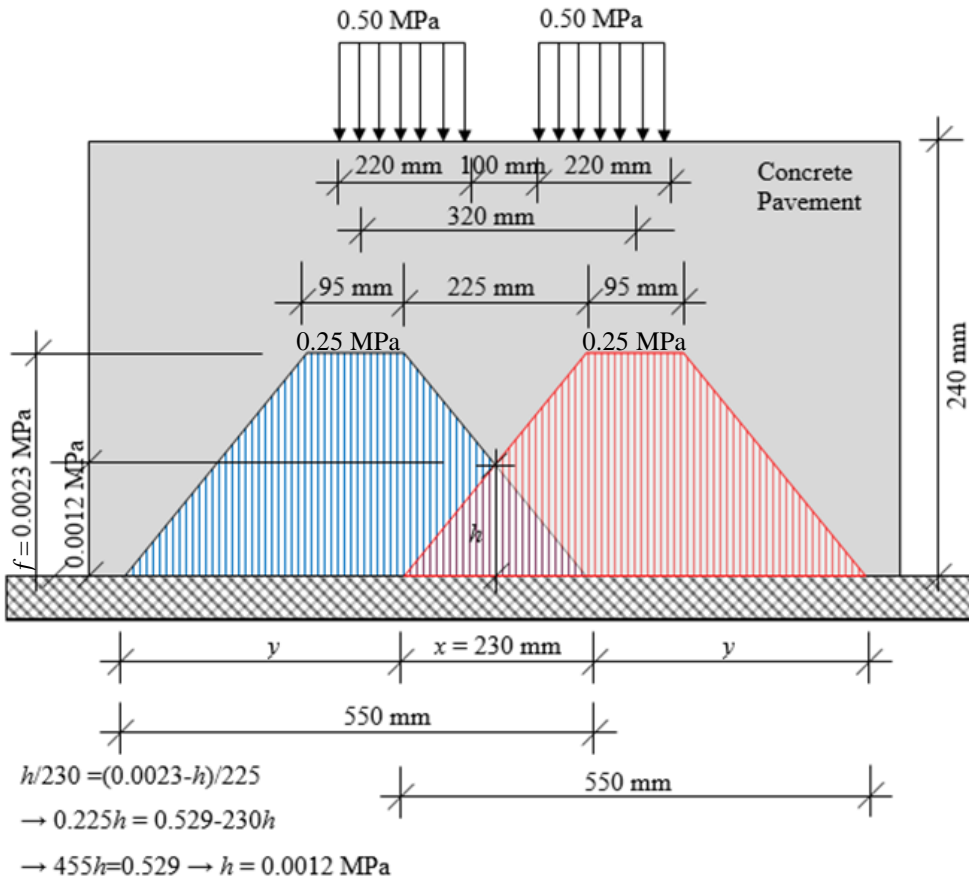


Fig. 22 Interacted dispersed stresses for *pavement thickness* = 24 cm and *wheel breadth* = 220 mm.

5. Conclusion

It is seen that the distribution of dispersed stress can be assumed to be trapezoidal, provided that stress concentrations that may develop at the edges are ignored. The generally assumed 45° angle for stress dispersal is not correct and moreover yields to unsafe pavement thickness values, because the dispersed stress does not remain uniform, but approximately trapezoidal. Thus, the maximum stress developed at the pavement base is aligned with the mid-point of the *wheel breadth*. The *elasticity modulus* and *Poisson's ratio* of the linear elastic pavement have no effect on the stress dispersal. If the *width* of the linear elastic pavement is greater than 1.5 times *wheel breadth*, then the *width* of the linear elastic pavement has also no effect on the stress dispersal. In summary, *f* is a function of *wheel load*, *wheel breadth*, and *thickness of pavement*, while *e₁* and *e₂* are functions of only *wheel breadth* and *pavement thickness*. Charts and tables derived using FE analysis have been verified, and the application of the proposed design method for linear elastic rigid (temporary or permanent concrete) pavements without reinforcement has been explained by means of a numerical example.

References

- [1] Groenendijk, J. Accelerated testing and surface cracking of asphaltic concrete pavement.- (Ph.D. Dissertation, Delft University of Technology, Delft, 1998.
- [2] Pottinger, M.G. The Three-Dimensional Contact Patch Stress Field of Solid and Pneumatic Tires. *Tire Science and Technology*, 1992; 20: 3-32. <https://doi.org/10.2346/1.2139508>
- [3] Tielking, J.K, Abraham, M. A. Measurement of Truck Tire Footprint Pressures. *Journal of the Transportation Research Board*, 1994; 1435: 92-99.
- [4] Beer, M. de. Measurement of tyre/pavement interface stresses under moving wheel loads. *Heavy Vehicle Systems, Special Series, Int. J. of Vehicle Design*, 1996; 3: 97-115.
- [5] Jong, F. B. P. de (2007). Renovation techniques for fatigue cracked orthotropic steel bridge decks.-Ph.D. Dissertation, Delft University of Technology, Delft.
- [6] Eurocode 3 Part 3. Actions on Structures, Brussel, Belgium, 2006.
- [7] Li, Y., Song, G, Cai, J. Mechanical Response Analysis of Airport Flexible Pavement Above Underground Infrastructure Under Moving Wheel Load. *Geotech Geol Eng*, 2017; 35: 2269-2275. <https://doi.org/10.1007/s10706-017-0242-8>
- [8] Swanson Analysis System. ANSYS, USA, 2017.
- [9] Timoshenko, S, Goodier, J. N. *Theory of Elasticity*, McGraw-Hill, New York, USA, 1969.

Appendices

Appendix 1

The Fortran code is given below.

```

IMPLICIT REAL*8 (A-H,O-Z)
CHARACTER*20 DAT,out1
CHARACTER*1 DA(20)
parameter(imax=80000,nmax=2600000)
double precision dp(nmax)
dimension fslp(3)
integer in(imax),nslope
WRITE(*,*)'Name of The Data File'
READ(*,550) DA
OPEN(4,FILE='DNAME')
K=0
DO 1 I=1,20
IF(DA(I).EQ.' ')GO TO 2
1  K=K+1
2  WRITE(4,*)''',(DA(I),I=1,K),''''
   WRITE(4,*)''',(DA(I),I=1,K),'.OUT'''
   REWIND 4
   READ(4,*)DAT
   READ(4,*)out1
   CLOSE(4,STATUS='DELETE')
550 FORMAT(20A1)
   OPEN(5,FILE=DAT)
   OPEN(10,FILE=out1)
C*****
   read(5,*) numdata ! number of data at the curve

c      data1=dp(1)
      i1=1+numdata*2

      call data_read(numdata,dp(1))

c      slope_x=dp(i1)
      i2=i1+3
c slope_x=dp(i2)
      i3=i2+3
c islope_p=in(1)
      n1=1+3

      call max_min(numdata,dp(1),dp(i1),dp(i2),in(1))

      nslope=1
      call slope_cal(numdata,dp(1),dp(i1),dp(i2),in(1),fslp(1))

      call calc_a_b(numdata,dp(1),dp(i1),dp(i2),in(1),fslp(1))
      aa=1.

stop
end

```

```

subroutine calc_a_b(numdata,data1,slope_x,slope_y,islope_p,fslp)
IMPLICIT REAL*8 (A-H,O-Z)
Dimension data1(numdata,2),slope_x(3),slope_y(3),fslp(3)
Integer islope_p(3)

w=slope_y(1)
a=w/atan(fslp(1))
aA=slope_x(1)-a
  aB=slope_x(1)+a

  x=slope_y(2)
b=w/atan(fslp(2))
bA=slope_x(2)+b
  bB=slope_x(2)-b

  e1=bA-aB
  e2=bB-aA
  f=slope_y(3)

  write(*,*) "e1=",e1
  write(*,*) "e2=",e2
  write(*,*) "f=",f

  write(10,*) "e1=",e1
  write(10,*) "e2=",e2
  write(10,*) "f=",f

return
end

subroutine slope_cal(numdata,data1,slope_x,slope_y,islope_p,fslp)
IMPLICIT REAL*8 (A-H,O-Z)
Dimension data1(numdata,2),slope_x(3),slope_y(3),fslp(3)
Integer islope_p(3),htype

htype=2    ! "1" for h, "2" for 2h

if (htype.EQ.1) then

  do j=1,3

    i=islope_p(j)
    h=data1(i,1)-data1(i-1,1)
    fx_ip2=data1(i+2,2)
    fx_ip1=data1(i+1,2)
    fx_im1=data1(i-1,2)
    fx_im2=data1(i-2,2)
    fslp(j)=(-fx_ip2+8*fx_ip1-8*fx_im1+fx_im2)/(12*h)

  enddo

else

```

```

do j=1,3

    i=islope_p(j)
    h=2*(data1(i,1)-data1(i-1,1))
    fx_ip2=data1(i+4,2)
    fx_ip1=data1(i+2,2)
    fx_im1=data1(i-2,2)
    fx_im2=data1(i-4,2)
    fslp(j)=(-fx_ip2+8*fx_ip1-8*fx_im1+fx_im2)/(12*h)

enddo

endif

return
end

subroutine data_read(numdata,data1)
IMPLICIT REAL*8 (A-H,O-Z)
Dimension data1(numdata,2)

do i=1,numdata
    read(5,*) (data1(i,j), j=1,2)
    data1(i,2)=data1(i,2)*(-1)
enddo

return
end

subroutine max_min(numdata,data1,slope_x,slope_y,islope_p)
IMPLICIT REAL*8 (A-H,O-Z)
Dimension data1(numdata,2),slope_x(3),slope_y(3)
Integer islope_p(3)
amax=0.0
amin=0.0

do i=1,numdata
    if(data1(i,2).GE.amax) then
        amax=data1(i,2)
    endif

    if(data1(i,2).LE.amin) then
        amin=data1(i,2)
    endif

enddo

slope_point=(amax+amin)/2.
error=abs(amax-slope_point)

slope_x1=0.0
slope_y1=slope_point

```

```
do i=1,numdata/2
  adiff=abs(data1(i,2)-slope_point)
  if(adiff.lt.error) then
    error=adiff
slope_x(1)=data1(i,1)
    slope_y(1)=data1(i,2)
    islope_p(1)=i
  endif
enddo

error=abs(amax-slope_point)
do i=numdata/2,numdata
  adiff=abs(data1(i,2)-slope_point)
  if(adiff.lt.error) then
    error=adiff
slope_x(2)=data1(i,1)
    slope_y(2)=data1(i,2)
    islope_p(2)=i
  endif
enddo

slope_x(3)=data1(numdata/2,1)
slope_y(3)=data1(numdata/2,2)
islope_p(3)=numdata/2

!      write(10,*) "slope_point=",slope_point

write(10,*) "slope_x1=",slope_x(1)," slope_y1=",slope_y(1)
write(10,*) "slope_x2=",slope_x(2)," slope_y2=",slope_y(2)
write(10,*) "slope_x3=",slope_x(3)," slope_y3=",slope_y(3)

!      write(*,*) "slope_point=",slope_point

write(*,*) "slope_x1=",slope_x(1)," slope_y1=",slope_y(1)
write(*,*) "slope_x2=",slope_x(2)," slope_y2=",slope_y(2)
write(*,*) "slope_x3=",slope_x(3)," slope_y3=",slope_y(3)

return
end
```

Appendix 2

Data tables for Figs. 16, 17 and 18 are provided below respectively.

Table 3. Data Table (f values) for Fig. 16.

T_p (mm)	$wB=100$ mm	$wB=150$ mm	$wB=200$ mm	$wB=220$ mm	$wB=250$ mm	$wB=270$ mm	$wB=300$ mm	$wB=320$ mm	$wB=440$ mm	$wB=540$ mm
10	0.009996	0.006666	0.005000	0.004545	0.004000	0.003704	0.003333	0.003125	0.002273	0.001852
50	0.009446	0.006637	0.004993	0.004537	0.003990	0.003695	0.003326	0.003119	0.002271	0.001851
100	0.006803	0.005707	0.004720	0.004379	0.003927	0.003664	0.003318	0.003117	0.002268	0.001847
200	0.003870	0.003656	0.003399	0.003290	0.003124	0.003014	0.002852	0.002747	0.002189	0.001831
300	0.002649	0.002579	0.002488	0.002447	0.002382	0.002336	0.002265	0.002217	0.001924	0.001697
500	0.001610	0.001594	0.001573	0.001563	0.001546	0.001534	0.001515	0.001501	0.001409	0.001323
750	0.001081	0.001076	0.001070	0.001067	0.001061	0.001058	0.001051	0.001047	0.001015	0.000984
1000	0.000815	0.000813	0.000810	0.000809	0.000806	0.000805	0.000802	0.000800	0.000786	0.000772

Table 4. Data Table (e_t values) for Fig. 17.

T_p (mm)	$W_B=100$ mm	$wB=150$ mm	$wB=200$ mm	$wB=220$ mm	$wB=250$ mm	$wB=270$ mm	$wB=300$ mm	$wB=320$ mm	$wB=440$ mm	$wB=540$ mm
10	81.8	131.8	181.8	201.8	231.8	251.8	281.8	301.8	421.8	521.8
50	38.6	88.5	138.5	158.4	188.4	208.5	238.4	258.4	378.4	478.4
100	45.1	65.3	94.8	97.5	127.4	147.4	177.0	197.2	317.2	417.1
200	63.4	62.3	71.1	93.6	99.0	97.5	129.6	131.8	208.6	294.6
300	88.0	93.5	91.8	101.6	106.0	112.3	116.4	120.4	181.2	230.8
500	13.0	12.1	134.6	130.2	138.8	149.0	155.0	148.9	180.9	212.6
750	196.1	206.7	198.4	195.4	208.2	202.7	215.5	209.6	227.8	241.9
1000	265.5	253.9	253.5	262.8	262.2	256.6	264.7	258.7	268.9	261.7

Table 5. Data Table (e_2 values) for Fig. 18.

T_p (mm)	$w_B=100$ mm	$w_B=150$ mm	$w_B=200$ mm	$w_B=220$ mm	$w_B=250$ mm	$w_B=270$ mm	$w_B=300$ mm	$w_B=320$ mm	$w_B=440$ mm	$w_B=540$ mm
10	118.2	16,2	218.2	238.2	268.2	288.2	318.2	338.2	458.2	558.2
50	161.4	211.5	261.5	281.6	311.6	331.5	361.6	381.6	501.6	601.6
100	234.9	274.7	325.2	342.5	372.6	392.6	423.0	442.8	562.8	662.9
200	416.6	437.7	468.9	486.4	501.0	522.5	550.4	568.2	691.4	785.4
300	612.0	626.5	648.2	658.4	674.0	687.7	703.6	719.6	818.8	909.2
500	100.0	1011.9	1025.4	1029.8	104.2	1051.0	106.0	1071.1	1139.1	1207.4
750	1483.9	1493.3	1501.6	1504.6	151.8	1517.3	1524.5	1530.4	1572.2	1618.1
1000	1954.5	1966.1	1966.5	1977.2	1977.8	1983.4	1995.3	2001.3	2051.1	2098.3

Blank Page



Research Article

Wind performance for a stadium geometry

Elton Hala^a

Department of Architecture, Polytechnic University of Tirana, Albania

Article Info

Article history:

Received 13 Feb 2020

Revised 02 April 2020

Accepted 30 April 2020

Keywords:

Wind engineering;

High-Rise building;

Stadium;

CFD simulation;

Abstract

High - rise buildings strongly influence the wind flow causing discomfort at the pedestrian level because of the down-draught effect on the building's facades. This is the case of the new stadium built in Tirana equipped with a tall building. Tall buildings influence the wind flow causing discomfort to the players level because of the down-draught effect on the building's facades. A CAD software integrated with the RANS CFD simulation method were used as an integrated package to better understand and test the wind flow in this complex building design. This paper tries to predict the aerodynamic performance in the prescribed geometry and address a problem for the new stadium design in Tirana. The current stadium generates bigger and stronger vortexes compared to the hypothetical model suggested by us. This study provides some design recommendations to avoid players and spectator discomfort. The approach used in the study can be applied in various buildings typologies.

© 2020 MIM Research Group. All rights reserved.

1. Introduction

Inconsistent winds flow between buildings hence, they are considered fluids that unexpectedly change their directions [1]. The way the air flows across the urban context is a complex fluid flow phenomenon [2]. Winds are three-dimensional and multidirectional with combinations of horizontal and vertical elements even though the vertical component is much smaller in the boundary level and often not considered. The impossibility of visualizing the airflow turns into a complex challenge for engineers testing the environmental performance of their planning choices [3]. Wind speed inside cities is affected mainly by the topography and the urban context [4]. Near the surface, wind parameters can differ from the dominant wind flow by cause of artificial and natural obstacles [5]. Because of friction, wind speed nearly disappears at the bottom of the boundary layer. If wind speed suddenly increases, some variations can become unexpected and to greater amplitude similar to "wind gusts" [6].

The issue is important particularly in playing fields where competitors are influenced by instantaneous wind gusts of high accelerations and unpredictable vortexes. Open - air environments offer fans the exceptional experience of enjoying games while yet experiencing the natural climate. Wind conditions in the playing field have a significant impact on the quality and performance of the game [7]. The open space performance is determined by architectural design in interaction with environmental conditions [7]. The existence of strong winds in running fields appears to be interesting, especially while establishing world records. The advantage of tailwind assistance is known for running sports [8]. Therefore, limitations are established into how much wind can assist outdoor athletes if they set a world record. When establishing a world record, the tailwind limit is set to 2m/s. If stronger than that, the record cannot be validated [9]. This practice is not

*Corresponding author: tonihala@gmail.com

^a orcid.org/0000-0001-8959-624X

DOI: <http://dx.doi.org/10.17515/resm2020.181st0213>

Res. Eng. Struct. Mat. Vol. 6 Iss. 4 (2020) 411-423

applied in football fields where no running records are registered. Anyway, in most cases, the football players adopt their abilities and skills also to wind speed and its direction. High-velocity wind can cause a change in ball acceleration. Also, unexpected wind gusts may influence the way they direct the ball in the air.

This is the case of the new central stadium built in Tirana. After different attempts to find financial aid, finally, in May 2016 the very last game at the outdated old stadium took place. The construction lasted for two years and in 2019 the newly designed stadium was presented. Inside the new structure, there is no room for a running track giving space to over 22,000 spectators, all covered by cantilever structures. The stadium was built as a public-private partnership agreement with a construction company that also built a multifunctional area. Quite unique was the presentation of a high-rise building included in the stadium perimeter.

Tall buildings often show captivating elegant profiles, but the higher they are, the stronger the wind blows on their top [6]. The air in high altitude moves much faster compared to that on the ground [10]. Many studies emphasize that tall buildings are strongly influencing the wind flow causing discomfort at the pedestrian level because of the down-draught effect on the building's facades [11]. The design team also proposed a tall building of 100meters, attached to the new stadium, with different functions in particular, hotels, shops, parking spaces, as indicated in (Fig. 1).



Fig. 1 Views outside the stadium. Photo by Elton Hala

The mass of air down-draught from tall buildings can cause unpleasant effects, most times leading to pedestrians' discomfort and where the wind is at high velocity, it may direct even safety issues. A tall building similar to the one attached in this stadium, can be disadvantageous to football players in the playing field. With the presence of the tall building, the new stadium might have an area in the playing field exposed to high-velocity winds and vortexes.

This paper tries to predict the aerodynamic performance in the inner geometry and discuss a problem related with the stadium design. To direct a possible problem with the stadium design requires considering different elements, in particular external geometry, obstacles, orientation, and so on. The prediction is made using computational techniques, repeatedly been used to assess the wind into the urban environment [12]. Relying solely upon the designer's judgement regarding the wind flow has led often to misinterpretation and confusion of this phenomenon. The urban wind is difficult to be predicted, since every individual city has distinctive layouts therefore, engineers should control in advance the wind effect in their planning choices throughout various methods. Computational fluid dynamics (CFD) mathematical method is frequently applied for wind flow analysis [13]. The CFD simulations help engineers to assess the effects of their planning choices. Much

research is done to visualize and factor the wind flow, even though it remains a complex fluid flow phenomenon. The CFD simulation presents many advantages toward the in-field measurements or the wind tunnel [14]. The CFD is used for the last 50 years as a tool to study many aspects of the urban environment [12].

The Reynolds-averaged Navier–Stokes (RANS) mathematical model is highlighted by several researchers, as a reasonable accuracy method for many circumstances [15]. A 3D steady RANS CFD simulations in cooperation with local criteria, is used to assess pedestrians' wind comfort around a huge football stadium in Amsterdam. The RANS model was also used to determine the wind flow patterns of a stadium architecture [16]. The steady-state RANS CFD mathematical model can also be used to assess the wind flow nearby and inside a stadium [17].

2. Method

It was created a 3D model in real scale maintaining the exact stadium geometry using the CAD software package. In the 3D model, small architectural details were considered incapable to influence the wind flow, therefore, they were not presented in this model. Also, the stadium surroundings were not included in the model since the main purpose of the paper is to investigate what happens inside the playing field and not outside the specified geometry. The CAD model was exported as a stereolithography (STL) file, ready to merge in the CFD package.

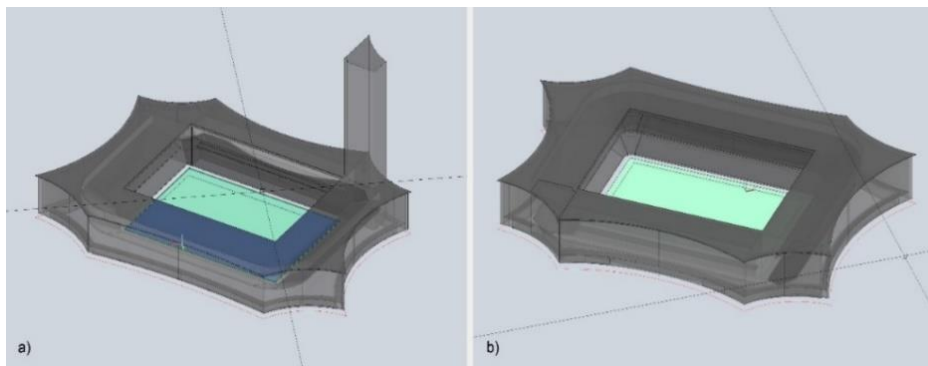


Fig. 2. Three-dimensional models built in CAD; a) model-A with tall building; b) hypothetical model-B

The import wasn't executed directly from the CAD file since they use meshes made by triangles that repeatedly intersect with triangles of other objects, consequently, they are considered as topologically incorrect. The CFD software adopts a special "shrink-wrapping" mesh topologically correct and can be therefore used as a model boundary for the generation of the Stadium Model. The RANS CFD simulations have always been used for the evaluation of pedestrian wind comfort and safety in urban areas [18]. Hence, it was considered useful also for this evaluation. The 3D model is shown in the (Fig. 2).

2.1 Wind speed and direction

The area where the stadium was built, and its microclimate were both essential for design values. The wind climate was provided from the Albanian Geo-Science Institute AGS database and the Weather Spark. They represent average values for a specific period when the wind takes effect. Over the course of the year, the mean wind speed for the stadium area varies from 0 km/h to 20km/h, while the maximum hardly exceeds 35km/h (10m/s) starting from November to February. The wind speed at this level (10m/s) was chosen as

the worst-case scenario hence, this parameter was applied in the CFD simulation. It was chosen a second scenario with the wind speed at a yearly coincidence of 20%. The wind speed at 4m/s matched our criteria for this simulation. Wind speed lower than 3m/s was considered acceptable and insignificant.

The northwest wind direction was the only one chosen for the simulation since the tall building in the stadium perimeter coincided also with this orientation. According to AGS, the wind is most often from the northwest for 2.8 months, from May 27 to August 22, with a peak percentage of 36% on June 28.

2.2 The criteria

The criteria to be used for assessment of pedestrian wind conditions have been developed through analysis and experience. Most of these criteria try to set a boundary wind speed over a possibility to occur [19]. The wind speed 4-5m/s for more than 5% of the time is considered a nuisance for most activities according to many studies, [20], [21], [22], and more recent studies [23], [24], [25], and wind mitigation strategies are typically recommended for these open areas. Thus, the wind speed at 4-5m/s seems to be the comfort limit also for individuals engaged in sports activities in particular soccer games.

2.3 Simulation

The first simulation tests the exact stadium geometry two wind speed (10m/s as the worst-case scenario and 4m/s typically windy day). This model was labeled "Model-A" and the simulations was named A10 and A04. The second simulation addresses a possible problem with the stadium design. This model was also evaluated in two wind speeds (10m/s and 4m/s). This hypothetical model was labeled "Model-B". The analysis was taken in three horizontal plans 5-10-20m, altogether covering the effective playing field area. Hence, it was observed the wind performance in vertical plans only for Model-A.

2.4 Flow parameters

The result of the calculation is a three-dimensional field of velocity and pressure covering the entire computational domain. The simulation domain dimensions are automatically set to fit the model size but can be modified if needed. The simulation parameters were as follows:

Parameters for Model-A and Model-B running at 10m/s:

- CFD Domain dimension: X=1,700m; Y=1,000m; Z=450m;
- Detailed mesh information: 773,597 cells;
- Used nodes: 874,985;
- Original model drag force sum: Fx=595.087kN, Fy=46.668kN, Fz=593.101kN;
- Simplified model drag force sum: Fx=584.305kN, Fy=54.106kN, Fz=631.64kN;
- Wind boundary profile :150m;
- Wind tested:10m/s.

Parameters for Model-A and Model-B running at 4m/s:

- CFD Domain dimension: X=1700m; Y=1000m; Z=150m;
- Detailed mesh information: 782,385 cells;
- Used nodes: 886,952;
- Original model drag force sum: Fx=60.533kN, Fy=14.925kN, Fz=93.097kN;
- Simplified model drag force sum: Fx=59.125kN, Fy=54.066kN, Fz=96.25kN;
- Wind boundary profile: 150m;

- Wind tested: 4m/s.

Wind parameters were as follows:

- Viscosity: $0.000015\text{m}^2/\text{s}$; This is considered the typical wind viscosity in open domains. The viscosity however depends on
- Air density: $1.250\text{kg}/\text{m}^3$; The density in general is directly related to many factors such as: air temperatures, atmospheric pressure, and humidity. This value explains the resistance of the air against the deformation. This density value is equal to the air at around 15°C .
- Convergence Criterion: (P-Residual) =0.001 This parameter indicates the accuracy of the model from the idealized model in percentage.

Turbulence Model Properties: To predict the turbulence flow so called (DNS) Direct Numerical Simulation need to have powerful computational availability. The CFD software used for these simulations uses a diverse method where wind parameters are averaged in mean and fluctuating components. It uses a modified set of air flow equations referred as RANS equations, mentioned also above.

- Flow model: The turbulence properties are included as required. The $k-\varepsilon$ turbulence model present two equations in RANS for turbulent flow conditions: the first one represents the transport equation of the turbulence kinetic energy k , and the second equation manage the transport of the dissipation rate ε of k . In these simulations no analytic calculation was provided. This model is popular among users since it engages less computational amounts to solve the equations. In our CFD software the equations values are automatically set based in the initial and the boundary conditions and this is considered to be the simplest turbulence model. The $k-\omega$ model probably would have given different outcome around the edges, but the used $k-\varepsilon$ model has also a credible result for a wide range of turbulence flows.
The software defines automatically the turbulent kinetic energy k and turbulent dissipation rate ε . The users sets the intensity of the turbulent flow.
- Turbulence kinetic energy k : $0.015\text{ J}/\text{kg}$
- Dissipation rate: ε : $4.6842\text{E}-06$
- Turbulence intensity i : 10% The typical turbulence air motion ranges between 5% to 20%. This value was set in between these values.

3. Results

3.1 Simulation domain parameters

The first simulation was considered the worst-case scenario running a wind velocity of 10m/s. The wind evaluation in different highs is presented in the (Fig. 3 a, b, c, the current stadium "Model-A" with the presence of the tall building and d, e, f, the stadium without the tall building presence, "Model-B").

Model-A simulation domain parameters: Dimensions: $X=1700\text{m}$; $Y=1000\text{m}$; $Z=450\text{m}$. Detailed mesh information for this model: 773,597 cells, 874,985 nodes. Original model drag force sum: $F_x=595.087\text{kN}$, $F_y=46.668\text{kN}$, $F_z=593.101\text{kN}$.

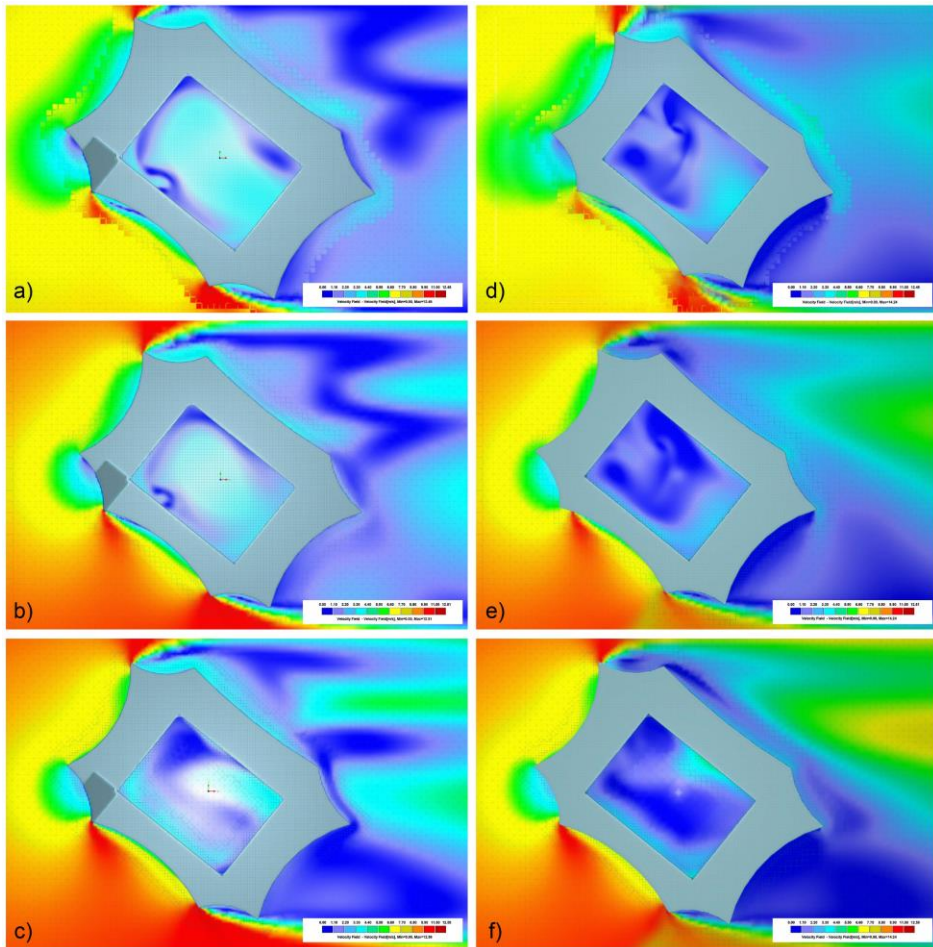


Fig. 3. Velocity field - simulation 10 m/s; a), b), c) current stadium model; d), e), f) hypothetical model - no tall building presence

The second simulation tests a lower wind speed of 4m/s and it corresponds to a typical windy day. Model-B simulation domain parameters: Dimensions: X=1700m; Y=1000m; Z=150m. Detailed mesh information for this model: 782,385 cells, 886,952 nodes. Original model drag force sum: $F_x=60.533\text{kN}$, $F_y=14.925\text{kN}$, $F_z=93.097\text{kN}$.

3.2 Velocity field plans

Results obtained in 5, 10, 20 meters high show the maximum wind velocity of 4.23m/s in the model-A and 73% of the playing area is affected by wind speed at 3-4m/s. Although Model-B generates a maximum registered velocity of 3.52m/s and 24% of the playing area is prevailed by wind speed over 3m/s.

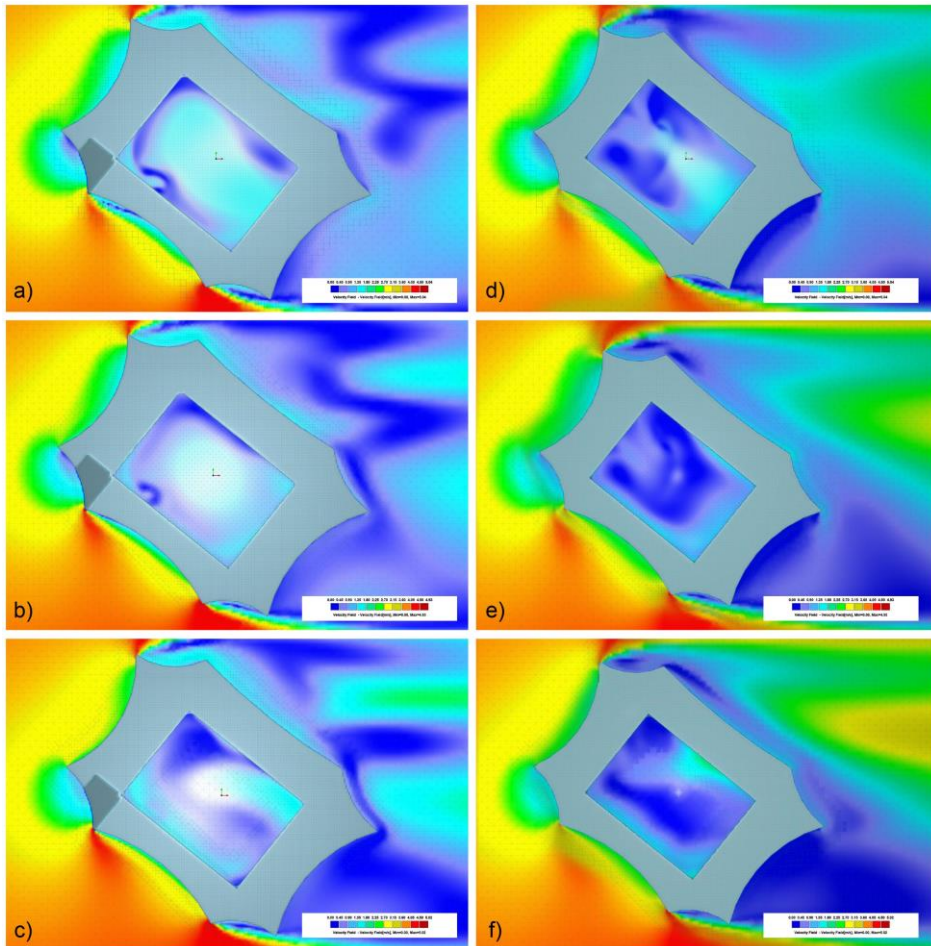


Fig. 4. Velocity field - simulation 4 m/s; a), b), c) current stadium model; d), e), f) hypothetical model - no tall building presence

Results obtained in the second simulation in 5, 10, 20 meters high show the maximum registered velocity of 1.67m/s in the model-A and 72% of the playing area is affected by wind speed at 1-2m/s. Model-B generates a maximum wind velocity of 1.35m/s and 25% of the playing area is prevailed by wind speed over 1.5m/s. These results were also confirmed from the streamlines graphs both in plan views and sections (Fig. 4).

There were changes in the wind speed at different altitudes. The area affected mostly from high-velocity wind was discovered at a high 0-5 meters referring to the playing ground. This area is loaded on high velocities winds, vortices, and turbulence air. The higher the altitude inside the stadium, the more likely the wind reduce its speed.

3.3 Vertical Section

The vertical plans were set to observe particularly the worst-case scenario, primarily across the tall building. Vertical planes were not set in the second testing speed, since these results can be used to assert the results discovered in horizontal plans. The results in (Fig. 5) approve that the current stadium can create more vortices to greater wind speed,

especially in the playing ground. Winds affected an extensive area, over 80% at 0-5m above the playing ground at 3-4m/s for the test running at 10m/s.

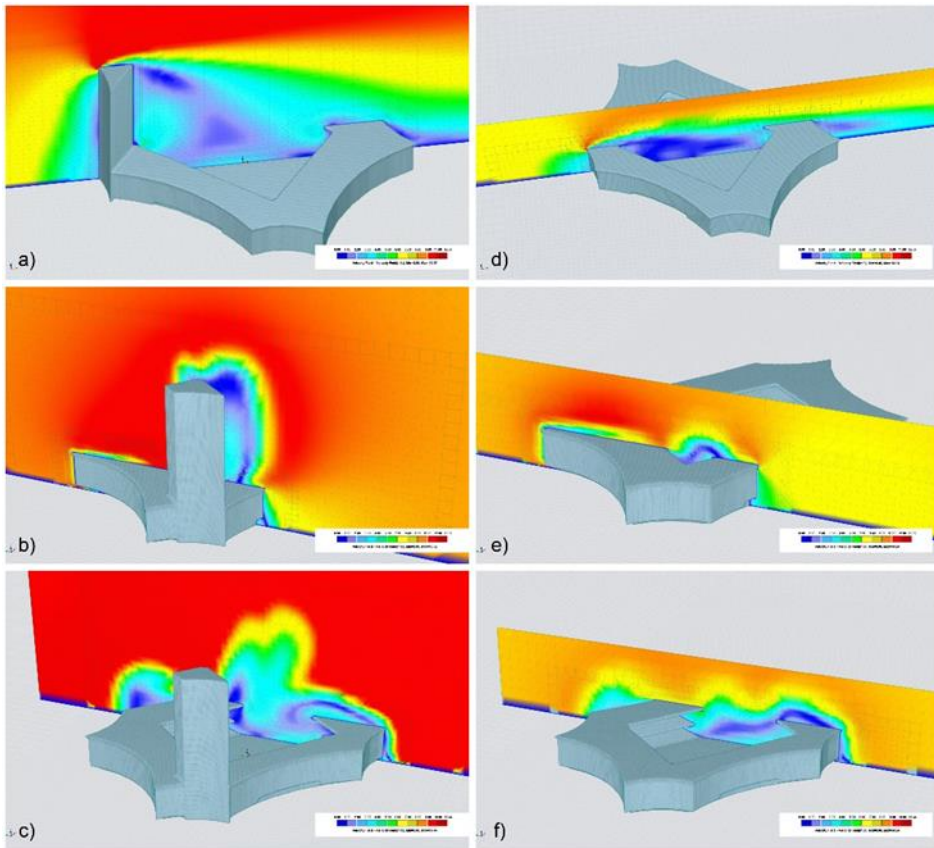


Fig. 5. Velocity field, axonometric views - first simulation 10 m/s; a), b), c) current stadium model; d), e), f) hypothetical model - no tall building presence

3.4 Tall building

The tall building connected with the stadium in the Model-A is capable of creating vortices more than 100 meters high. By observing the streamlines, (Fig. 6a), the tall building can generate turbulence for a wide area of more than 400x100x40m. Several vortices are generated especially below the tall building in the north-eastern direction at a speed of 1.0m/s - 1.4m/s especially in a worst-case scenario Model-B (Fig. 6b). The vortices are also present in the Model-B even though at a lower speed. These vortices are not generated in a typically windy day scenario (Fig. 6b).

3.5 Pressure field

In the pressure field graphs, the playing area is substantially less charged at Model-B. For tests running at 10m/s, results show the maximum dynamic pressure of 63.0Pa to 32.8Pa between our models. Hence, the Model-B is emerging in the system a lower number of

interacting particles, thus a dropped pressure is registered in the graphs (Fig. 7). The surface pressure in the building facades does not reveal any useful information to be used for assessing the wind flow inside the stadium.

Model-A is capable of producing more vortices in the playing field to greater wind speed in both scenarios.

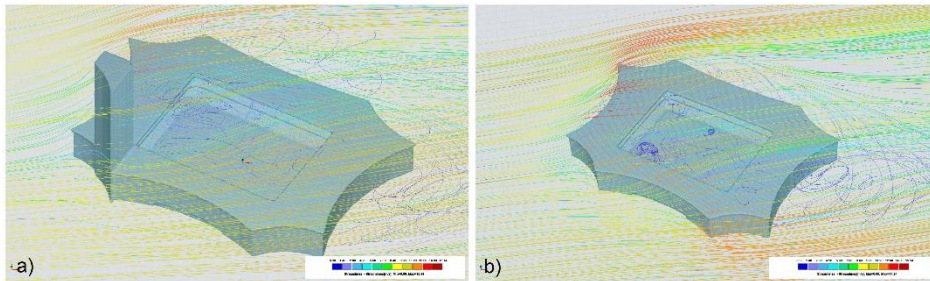


Fig. 6. Streamlines in the first simulation 10 m/s; a) current stadium; b) hypothetical model

4. Discussions

By comparing these two geometrical models in various wind conditions, important findings were discovered. Referring to wind engineering, our hypothetical model (unequipped with a tall building in the stadium proximity) was able to get better results by offering more comfort in the playing field in contrast with the current stadium geometry.

Compared to the current stadium design, the hypothetical Model-B, have smaller areas exposed to high-velocity air. This result was detected in every testing wind speed. For us, this was a perception of a problem with the current stadium design.

In a windy day blowing from the northeast, not unusual for the area, the current stadium will generate bigger and stronger vortexes comparing to the hypothetical model offered from us. Particularly these effects happen 0-5 meters above the playing ground, which is considered an intense playing area. It was also detected an area in which the vortexes are generated easily. This area was detected near the tall building base.

Model-B was also responsible for creating a lighter vortexes, particularly around the playing ground. Vortexes were displayed also in the hypothetical model. These effects probably are found in all open fields which are surrounded by high barriers in particular stadium stairs. Our hypothetical model has offered tolerated wind speeds also in the stairs and the surrounding area outside the stadium. The wind circulation in both scenarios was to a lower speed comparing to the current stadium design.

Based on a general understanding of aerodynamics, the following explanation were found for the model's contrasts. The present stadium is equipped with a 100 meters tall building with a direct connection with the playing field (Fig. 8). The presence of the tall building in the stadium perimeter was unusual among stadium designs. The tall building can serve also as a wind catcher hence, it directs more wind at high velocities mostly as a result of

the down-draught effect [11]. The wind gains a lot of speed because of tall buildings and opened corridors it passes through [27].

The first simulation tested a scenario running at a velocity of 10m/s and the high-rise building represented in the Model-A was able to increase the wind speed in the playing field to a maximum of at 4.23m/s. The wind speed 4-5m/s is considered a nuisance for most activities, including outdoor sports, according to many studies, [20], [21], [22], and recent studies like [23], [24], [25]. Thus, the wind speed at 4-5m/s seems to be the limit also for people involved in sports activities in this stadium. Hence, if the wind coincides with the tower direction at 10m/s unpleasant effects can be seen with the players and the soccer ball trajectories. The phenomena mainly emphasize the wind gusts, which is defined as a short-duration or a maximum of the predominant wind speed [28].

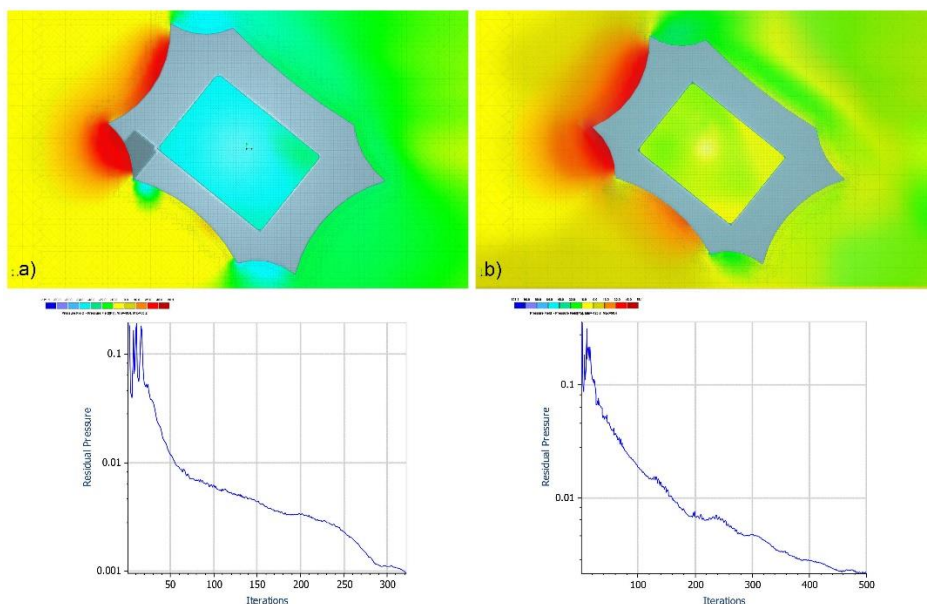


Fig. 7. Pressure field and residual pressure in the first simulation 10 m/s;
a) current stadium; b) hypothetical model

The stairs geometry can also contribute to intensifying the circular air motion. A uniform flow around a circular shape creates a nonlinear system used to generate vortexes [29]. Particularly this effect is amplified from the gigantic cantilever canopies provided in the stadium to serve as rain shelters for spectators enjoying outdoor sports activities. Van [16], pointed out that architects often design stadium shelters with only vertical rainfall in mind, neglecting the wind effect that can also sweep the rain onto the seats.

5. Conclusions

- Computer-Aided Design is yet a valuable approach to design the building shape and the wind-flow patterns can be determined efficiently by Reynolds-averaged Navier-Stokes, Computational Fluid Dynamics (CFD) simulation. CAD software integrated with the RANS CFD simulation method can be used as an integrated package to better understand and evaluate the wind flow in this complex building design. Since the air

molecules are invisible, the CFD is yet a valuable tool to visualize the wind flow in every environmental domain.

- The major concern of the present stadium design was related to the tall building attached to the stadium geometry. Most of the unpleasant effects on the playing field are addressed to the presence of the tall building and its close distance with the playing field. This result was shown by simply proposing the same model geometry unequipped with this 100-meter-tall building. The situation changed efficaciously by reducing the wind speed up to 2.9m/s in the playing field.
- Vortexes were present in both models due to the closed shaped stadium. The air is obstructed and moves in a circular motion around the stairs and with nowhere to go, it injects in the playing field. Simulation results suggest that there will be a bigger area of high velocity turbulence. In a strong windy day, the wind speed (4.23m/s) generated in the playing field will not be acceptable. The close shapes stadium probably needs mitigation strategies, for instance openings.



Fig. 8. Stadium Interior. Photo by Elton Hala

Further studies

Tall buildings often present fascinating elegant silhouettes, but the higher they are, the stronger the wind is conveyed in their base. Hence, their effect on the playing ground might be bigger. The authorities should pay attention to tall buildings co-existence close to the playing fields. Further studies also can be done to better understand how the vortexes are generated and how the surroundings can generate or prevent their creations. Future research might focus on understanding the way the ball bypasses the player's expected trajectory on a windy day and how it affects their reactions.

6. References

- [1] Wohland J., Wohland J., Omrani NE., Witthaut D., Witthaut D., Keenlyside N. Inconsistent Wind Speed Trends in Current Twentieth Century Reanalyses. *Journal of Geophysical Research*, 2019;124(4):1931-1940. <https://doi.org/10.1029/2018JD030083>
- [2] Orlandi P. *Fluid flow Phenomena: A Numerical Toolkit*, Dordrecht, Kluwer. 2000. <https://doi.org/10.1007/978-94-011-4281-6>

- [3] Max N., Crawfis R., Williams DN. Visualizing wind velocities by advecting cloud textures. 1992.
- [4] Hitchcock PA., Kwok KC., Wong K., Shum KM. The effects of topography on local wind-induced pressures of a medium-rise building. *Wind and Structures*, 2010;13(5): 433-449. <https://doi.org/10.12989/was.2010.13.5.433>
- [5] Zhang H., Pu Z., Zhang X. Examination of Errors in Near-Surface Temperature and Wind from WRF Numerical Simulations in Regions of Complex Terrain. *Weather and Forecasting*, 2013;28(3):893-914. <https://doi.org/10.1175/WAF-D-12-00109.1>
- [6] Crosbie J, Perry D, Smith Th. Buildings at risk: Wind design basics for practicing architects. Manual prepared by the American Institute of Architects (AIA) 2008.
- [7] Goliger AM. Wind-tunnel testing of sports stadia to optimize their use and safety. *J. S. Afr. Inst. Civ. Eng., Midrand*, Apr. 2010; 52, (1).
- [8] Dapena J., Feltner ME. Effects of Wind and Altitude on the Times of 100-Meter Sprint Races. *International journal of sport biomechanics*, 1987;3(1):6-39. Retrieved 4 2, 2020. <https://doi.org/10.1123/ijsb.3.1.6>
- [9] IAAF - International Association of Athletics Federations. Competition Rules. 2017; 269-281.
- [10] Simiu E, Scanlan SH. Wind Effects on Structures. John Wiley and Sons, Canada. 1996.
- [11] Hala E, Nepravishta F, Panariti A. The wind flow effects and high-rise buildings in urban spatial morphology. *Cities in Transitions, Proceedings of the 1st International Forum on Architecture and Urbanism*, 14-16 December 2017 Tirana Albania. Publisher: La scuola di Pitagora Editrice. 2019. pp 52-56, ISBN 978-88-6542-679-1, ISBN 978-88-6542-695-1.
- [12] Qingyan Y. Chen. Using computational tools to factor wind into architectural environment design. *Energy and Buildings*, 2004; 36: 1197-1209. <https://doi.org/10.1016/j.enbuild.2003.10.013>
- [13] Reiter S. Assessing wind comfort in urban planning. *Environment and Planning B: Planning and Design*, 2010;37(5): 857-873. <https://doi.org/10.1068/b35154>
- [14] Blocken B, Janssen WD, Van Hooff J. CFD simulation for pedestrian wind comfort and wind safety in urban areas: General decision framework and case study for the Eindhoven University campus. *Environmental Modelling & Software*, 2012;30: 15-34. <https://doi.org/10.1016/j.envsoft.2011.11.009>
- [15] Blocken B, Persoon J. Pedestrian wind comfort around a large football stadium in an urban environment: CFD simulation, validation and application of the new Dutch wind nuisance standard. *Journal of Wind Engineering and Industrial Aerodynamics* 2009;97(5-6), 255-270. <https://doi.org/10.1016/j.jweia.2009.06.007>
- [16] Van Hooff T, Blocken B, Van Harten M. 3D CFD simulations of wind flow and wind-driven rain shelter in sports stadia: Influence of stadium geometry. *Building and Environment*, 2011;46(1): 22-37. <https://doi.org/10.1016/j.buildenv.2010.06.013>
- [17] Mei W, Qu M. Evaluation and Analysis of wind flow for a football stadium. *Science Direct*. 2016;145: 774-781. <https://doi.org/10.1016/j.proeng.2016.04.101>
- [18] Wu H, Kriksic F. Designing for pedestrian comfort in response to local climate. *Journal of Wind Engineering and Industrial Aerodynamics*, 2012;104-106: 397-407. <https://doi.org/10.1016/j.jweia.2012.02.027>
- [19] Janssen WD, Blocken B, Van Hooff T. Pedestrian wind comfort around buildings: comparison of wind comfort criteria based on whole-flow field data for a complex case study. *Building and Environment*. 2012; 1-27. <https://doi.org/10.1016/j.buildenv.2012.10.012>
- [20] American Society of Civil Engineering - ASCE. Task Committee on Outdoor Human Comfort of the Aerodynamics Committee of ASCE, *Outdoor Human Comfort and its Assessment*, American Society of Civil Engineers, Reston, VA. 1979. 978-0-7844-0684-7 (ISBN-13) | 0-7844-0684-7 (ISBN-10).

- [21] Melbourne WH. Criteria for environmental wind condition. Journal of Wind engineering & Industrial Aerodynamics 1978; 3: 241-24. [https://doi.org/10.1016/0167-6105\(78\)90013-2](https://doi.org/10.1016/0167-6105(78)90013-2)
- [22] Murakami S, Iwasa, Morikawa Y. Study on acceptable criteria for assessing wind environment on ground level based on residents' diaries. Journal of Wind Engineering and Industrial Aerodynamics. 1986;24: 1-18. [https://doi.org/10.1016/0167-6105\(86\)90069-3](https://doi.org/10.1016/0167-6105(86)90069-3)
- [23] Bottema M. A method for optimization of wind discomfort criteria. Build Environmental 2000;35(1): 1-18. [https://doi.org/10.1016/S0360-1323\(98\)00065-1](https://doi.org/10.1016/S0360-1323(98)00065-1)
- [24] NEN 8100. Wind comfort and wind danger in the built environment. NEN 8100 Nederlands Normalisatie Instituut Publications. 2006.
- [25] Koss HH. On differences and similarities of applied wind comfort criteria. Journal of Wind Engineering and Industrial Aerodynamics 2006; 94: 781-797. <https://doi.org/10.1016/j.jweia.2006.06.005>
- [26] Blocken B. 50 years of computational wind engineering: past, present and future. Journal of wind engineering and industrial 2014; 129: 69-102. <https://doi.org/10.1016/j.jweia.2014.03.008>
- [27] Hala E. Turning the effect of urban wind into an asset: its impact in climate-sensitive urban design. Proceedings of the International Conference for Civil Engineering, In English, ICCE2017, 12-14 October 2017 Tirana Albania, 2017;2:196. ISBN 978-9928-4429-2-5.
- [28] Suomi I, Vihma T. Wind Gust Measurement Techniques-From Traditional Anemometry to New Possibilities. Sensors. 2018; 18(4): 1300. <https://doi.org/10.3390/s18041300>
- [29] Vasconcelos GL, Moura MN, Schakel AMJ. Vortex motion around a circular cylinder. Physics of Fluids. 2012; 23(12). <https://doi.org/10.1063/1.3667269>

Blank Page



Research Article

Influence of material properties on the seismic response of masonry buildings

Marjo Hysenlliu^{1,a}, Altin Bidaj^{1,b}, Huseyin Bilgin^{*2,c}

¹Department of Civil Engineering, Polytechnic University of Tirana, Albania

²Department of Civil Engineering, EPOKA University, Tirana, Albania

Article Info

Article history:

Received 20 Jan 2020

Revised 9 March 2020

Accepted 13 April 2020

Keywords:

URM buildings;

Pushover methods;

Macro modelling;

Limit states.

Abstract

Recent earthquakes occurred in many parts of the world have shown that unreinforced masonry [URM] buildings constructed according to older codes may constitute an important source of risk. It is known that the mechanical response of the masonry structures depends on several factors including the compressive and shear strength of its constituents, bricks shape as well as the volumetric ratio between the wall texture and components. In this study, the effects of the material choices of a particular type of masonry buildings were studied. The typology chosen in this study represents a typified masonry building of the current Albanian building stock; these buildings were mostly built between 1977-78 and thus were designed without considering the seismic requirements proposed in today's modern codes. This template building has been constructed in different regions of the country with the same architectural and structural configuration in two versions; red clay bricks and silicate bricks. The aim of this study is to investigate the influence of these two different materials on the seismic response of the selected masonry building. The evaluation is based on the use of nonlinear static analyses, performed by using TREMURI software. In order to estimate the reliable seismic response for this typology, extensive research in terms of historical information, structural characterization and the definition of the inherent material parameters has been executed. Upon the evaluation of the obtained results, in contrast to the type of buildings constructed by clay masonry, calcium silicate one showed a stiffer and slightly stronger response. However, at similar values of in-plane, lateral drift they exhibited more brittle response yielding unforeseen damage during seismic excitations.

© 2020 MIM Research Group. All rights reserved.

1. Introduction

Recent damaging earthquakes in eastern Mediterranean countries including Italy (Umbria-Marche; 1997, Abruzzo, 2009), Greece (Grevena-Kozani, 1995, Aigio, 1995, Athens 1999), Cyprus (Paphos, 1995, Lemesos, 1996), Turkey (Izmit, 1999, Van 2011, Elazığ 2020) and Albania (Durrës, 2019) resulted in great losses of building stock in historical centers. As a Balkan country in this region, Albania has a building stock dominated by low and mid-rise unreinforced masonry. Particularly, Bilgin and Huta 2018, [1] have shown that the URM is the dominant building typology of the country for both public and private buildings during the socialist era (1944-1990). Most of these current masonry buildings were designed considering merely gravity loads without any consideration of earthquake resistant design rules [2]. Furthermore, previous studies [3-11] and earthquake inspection reports have shown that masonry structures are very susceptible to seismic movements. Consequently, this typology has high seismic vulnerability over the region. This means that a moderate

*Corresponding author: hbilgin@epoka.edu.al

^a orcid.org/0000-0002-0863-2112; ^b orcid.org/0000-0002-1101-6310; ^c orcid.org/0000-0002-5261-3939

DOI: <https://dx.doi.org/10.17515/resm2020.177st0120>

Res. Eng. Struct. Mat. Vol. 6 Iss. 4 (2020) 425-437

or big earthquake might produce a catastrophic result associated with the masonry structures in the region.

Recently, masonry structures have been the subject of interest and research with respect to identifying the seismic capacity of these buildings. It is estimated that more than 75% of the building stock in Albania is made of masonry material [12-14]. Thus, they form an important percentage and a typical typology for the country. There are typified buildings all over the country for residential purposes. Most of these masonry structures were constructed according to the earlier codes [15-16] by red clay bricks or calcium silicate bricks. Although this region is generally characterized by low-moderate seismicity hazard, the problem of the induced seismicity is becoming more and more relevant [7]. Therefore, the evaluation of the seismic vulnerability of these types of red clay brick and calcium silicate brick masonry structures is crucial in order to assess the risk generated by the induced seismicity. Since the region was hit recently by a moderate earthquake (November 26, Durrës), the common construction practice showed a lack of earthquake proof details.

This study aims at assessing the seismic response of an existing masonry residential building constructed by clay and silicate bricks. For this purpose, based on a survey done on masonry buildings in the capital city of Tirana, a five-story typified masonry building was selected and modelled by using TREMURI software [17]. Mechanical properties of the case study building have been determined experimentally and adopted for the nonlinear analysis. The macroscale structural response of two buildings were then comparatively evaluated through nonlinear-static analyses. Although nonlinear dynamic analysis is capable of giving a deep insight on the inelastic response of the buildings, their application requires more refined and complete approach. Hence, in spite of some inevitable approximations of structural response, macro-element methodology provides an effective means of validating the safety of masonry structure and its vulnerability to extensive damage and collapse. The results of the nonlinear-static analyses performed on two buildings are discussed. Particular attention is paid to the use of nonlinear static procedures as a tool of verification.

2. Development of Structural Models

Typical masonry building stock in Albania are template designs of low to moderate rise buildings. The structure is principally comprised of two parts, namely the load bearing walls and floor and roof diaphragms. The walls are stiff with several openings and the diaphragms are usually constructed of RC slabs. For the scope of the study, a typified URM mid-rise building is selected as a representative in the region. The masonry building, which has been analyzed, has five stories, brick walls of 38 cm for the load bearing walls in the first two stories and reduced to 25 cm in the remaining ones with a 12 cm thickness for other partition walls. It has 1920 cm x 1440 cm dimensions in plan with a story height of 280 cm (Fig. 1). Utilizing this template, two types of structures designed using red clay brick and calcium silicate brick are analyzed. These two types of buildings were chosen to have two fundamentally different scenarios in terms of the material characteristics and lateral deformation mechanisms. For the construction of the mathematical models, solid red clay (Scenario - A) and calcium silicate bricks (Scenario - B) connected with cement mortar are used to build the masonry walls for both buildings, respectively. The floors are in-situ concrete ones with a height of 15 cm and a flat roof. In order to guarantee a better distribution of horizontal and vertical loads, ring beams were constructed to create a continuous connection between load bearing walls and slabs.

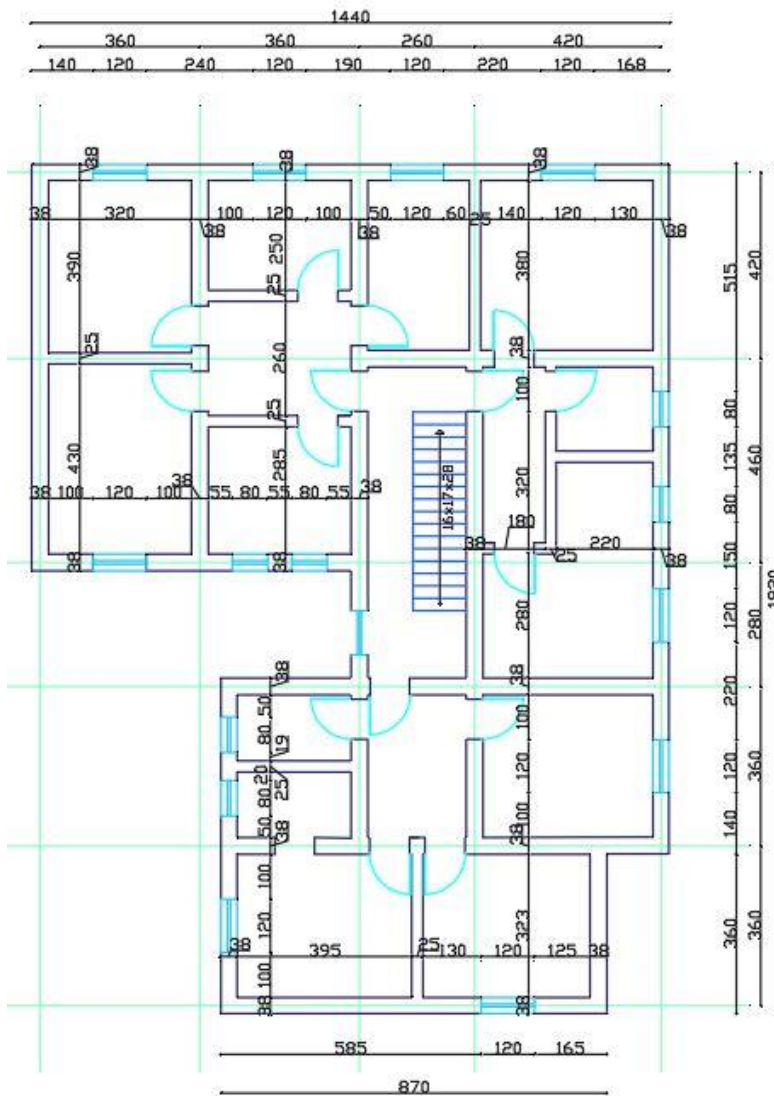


Fig. 1 Typical plan view of the selected masonry building, (units in cm)

In order to accurately characterize the strength and structural integrity of the structure, inherent mechanical characteristics of the masonry material are evaluated from the experimental tests performed on two buildings constructed by red clay brick and calcium silicate brick masonry. It consists of strength tests on brick units and mortar samples, as well as tests on small masonry assemblages, such as compression and shear tests on triplets. The clay and silicate bricks were tested in compression according to EN 772-1 (2000) [18]. The flexural and compressive strength of the mortar were defined according to the prescriptions of EN 1015-11 [19]. These tests allowed the determination of the compressive strength of masonry (f_m), as well as the secant modulus of masonry (E_m) (Fig. 2).

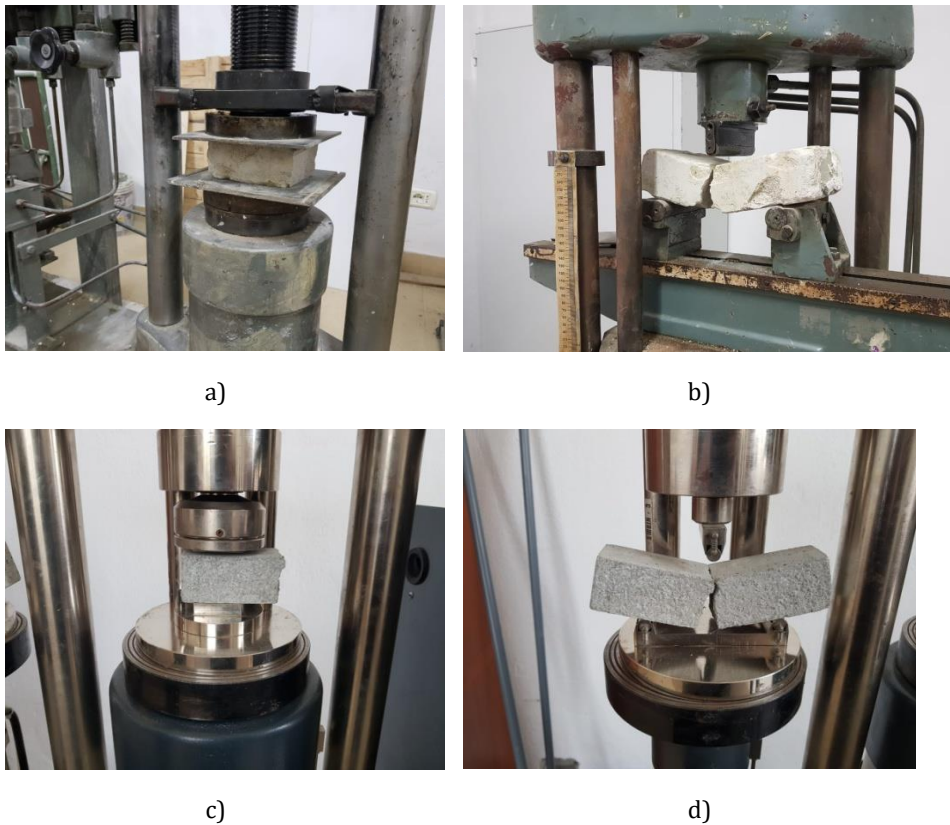


Fig. 2 Brick compression and tensile flexural test (a-b); Mortar samples compression and tensile flexural test (c-d)

Table 1. Clacy and silicate brick properties

Building	Brick properties			Mortar properties		
	Type	f_b [MPa]	f_{bt} [MPa]	Type	f_m [MPa]	f_{mt} [MPa]
5- Story	Clay	7.5	1.7	Lime	4.8	1.1
5- Story	Silicate	10.0	2.6	Cement	5.0	1.0

Six masonry prisms produced by silicate and clay bricks were tested (Fig 3.) in compression in the direction perpendicular to the horizontal bed-joints, according to EN 1052-1 [20]. Specimens of both types of masonry were also subjected to the shear test for the determination of the initial shear strength (f_{v0}) and the friction coefficient (μ), according to the guidelines given by EN 1052-3 [20].

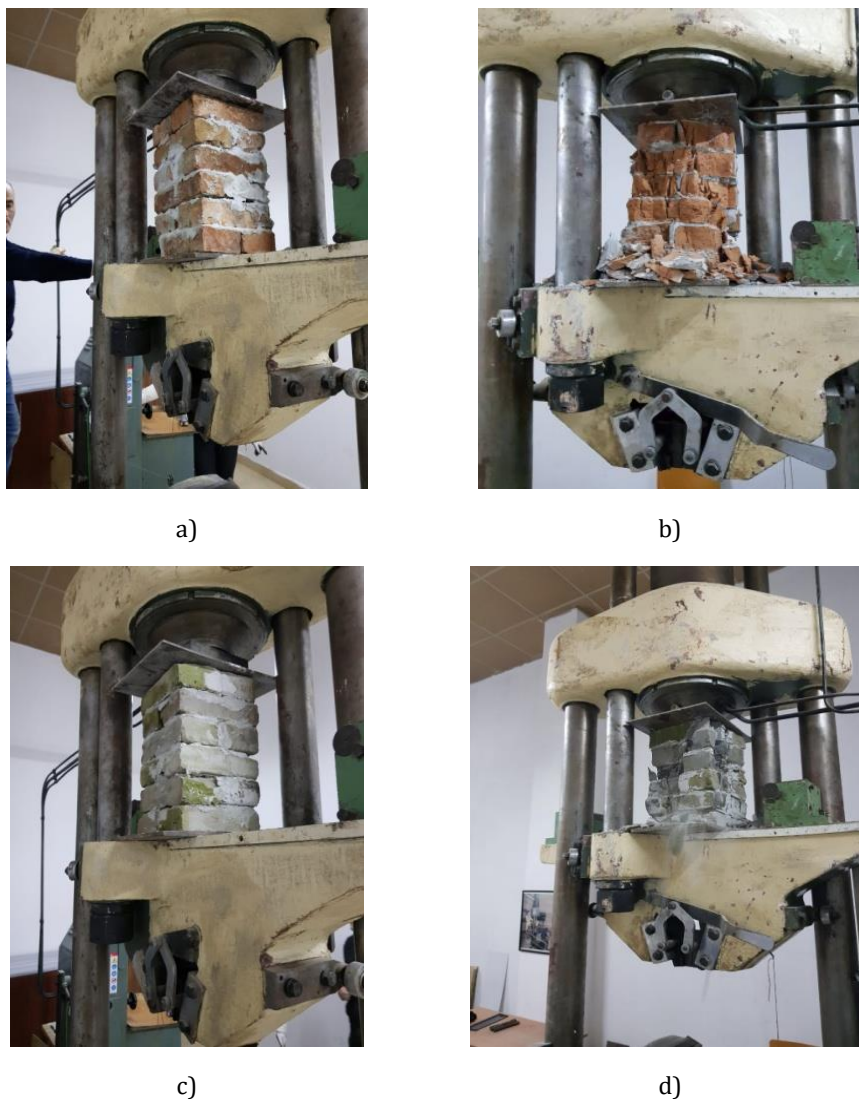


Fig. 3 Masonry prism tests (a-b); Red clay brick samples under compression and silicate brick test (c-d)

According to the test results, clay bricks and the mortar inherent characteristics are tabulated (Table 1-2).

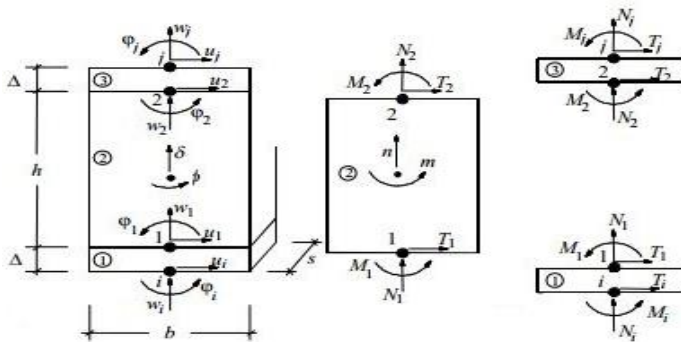
Table 2. masonry wall properties for analysed buildings

Material Type	f_k [MPa]	f_{vk} [MPa]	f_{vk0} [MPa]	f_t [MPa]	E [MPa]	G [MPa]	ν
Clay	2.42	0.36	0.2	0.121	2420	605	0.2
Silicate	2.97	0.4	0.22	0.149	2970	742	0.2

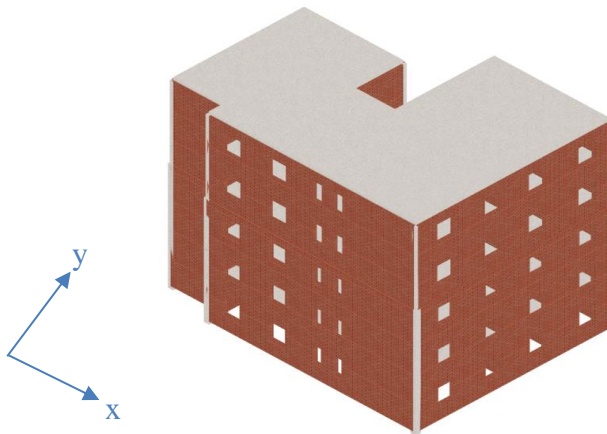
3. Modeling Approach

Masonry is a heterogenous material constituted of two components: the masonry bricks and the mortar. Its mechanical features depend on the inherent properties of its components. Its behavior can be very complicated under simple static loadings. In order to simulate the response of URM structures, numerous assumptions are made, and numerical models are suggested in the literature [21]. The adopted model in this paper is macro-modelling technique. According to this approach, each wall is represented by discretized elements that have equivalent properties. TREMURI [17] software is deployed to conduct the numerical analysis. This is based on a finite element methodology for modelling masonry structures. The nonlinear macro-element approach, representative of a whole masonry panel, proposed by Gambarotta and Lagomarsino [22], permits with a limited number of degrees of freedom, to represent the two main in-plane masonry failure modes, shear-sliding mechanism and bending-rocking, on the basis of the assumptions.

The conventional macro-element used for pushover analyses is schematized with the kinematic model described in Fig 4a. The 3D model of the examined masonry building, where it is apparent that masonry walls are modelled through a mesh of masonry spandrels and piers, is depicted in Fig 4b.



(a)



(b)

Fig. 4 a) The macro-element kinematic model; b) the 3D building model with macro-elements setup through the TREMURI software.

Seismic capacity of the URM buildings is obtained by pushover analyses. Member sizes were used to model the selected building without making any simplifications.

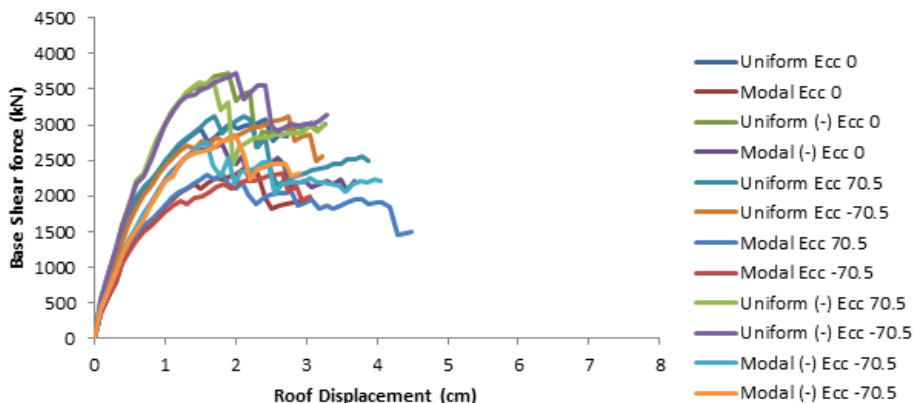
5. Analysis Results

5.1 Capacity Evaluation

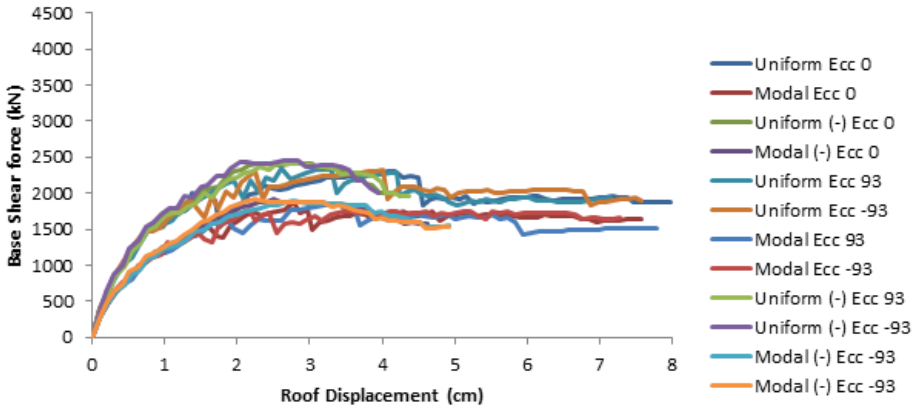
The nonlinear static analysis is an analysis method which permits defining the structural behavior under the seismic and gravity loads exerted on the structures. The behavior of the structure is represented through the pushover curve which typically gives the relation between the base shear force and roof displacement. It could be also mapped in ADRS format together with the demand curve and estimate the top displacement under the design earthquake to find the performance point of the structure. The scales of the seismic forces are increased in a stepwise manner in order to monitor the yielding cycles and the development of the overall capacity curve. A pushover analysis is performed at each step till the structure loses its stability.

In TREMURI approach are two load patterns applied: first mode shape distribution (static), based on the fundamental mode shape of the structure, and a uniform load distribution to all stories. The two are performed in two directions X- and Y- and with positive and negative values. So, in total eight analysis: +x MF1, +x uniform, -x MF1, -x uniform, +y MF1, +y uniform, -y MF1, -y uniform. These analyses were done for each combination. Without eccentricity of gravity load and with eccentricity of two different levels. For both simulations representing the red clay and silicate brick designed buildings, are computed 24 analyses, for all load combinations, earthquake direction, with and without eccentricity. The worst cases were chosen as representing the pushover curves for both x- and y-direction of buildings.

Upon completing the analytical modeling process, the pushover curves of the clay and silicate brick buildings were determined by carrying out nonlinear static analysis in TREMURI (Fig 5-6.). For the scope of the analyses, lateral load distribution proportional with the mode shapes were applied to the mass center of each storey considering the seismic weight. Seismic weight of the masonry buildings was calculated by considering the combination of Dead (G) and Live (Q) loads ($G + 0.3 Q$).

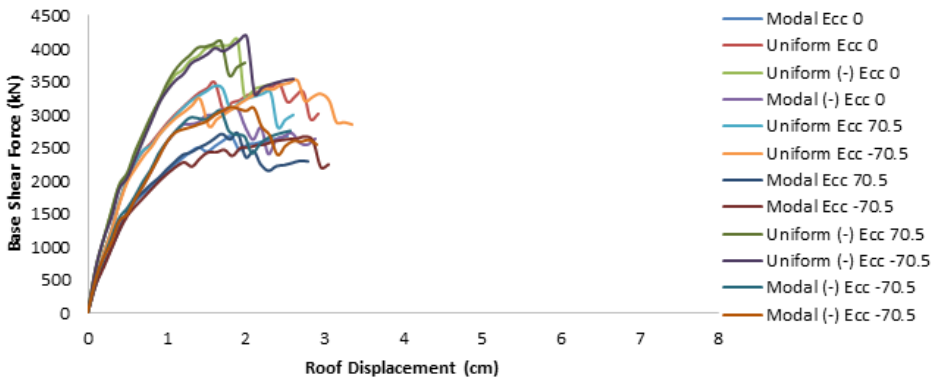


a) x- direction

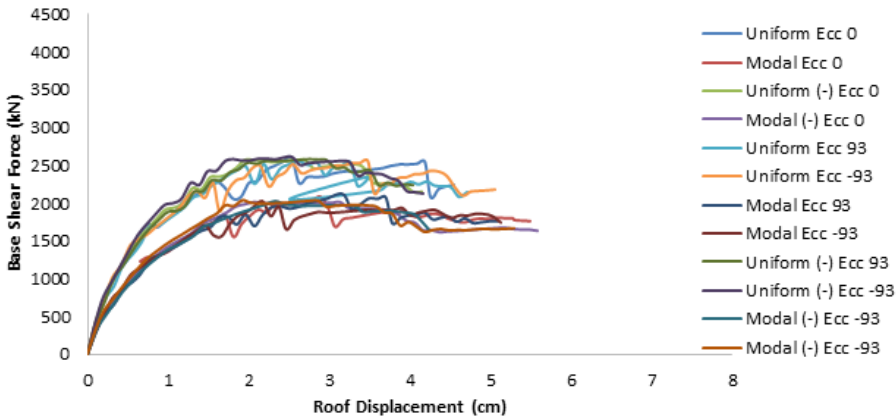


b) y- direction

Fig 5. Capacity curves for clay brick masonry buildings



a) x- direction



b) y- direction

Fig 6. Capacity curves for silicate masonry building

Subsequently, following the outlined criteria in Eurocode 8, Part 3 damage limit states of the studied buildings were calculated, and seismic capacities were determined. The capacity evaluation of the investigated buildings was performed using Part 3 of Eurocode 8 [23]. Three limits states levels, i.e., “Damage Limitation (DL)”, “Significant Damage (SD)” and “Near Collapse (NC)” are defined for performance evaluation (Fig 7).

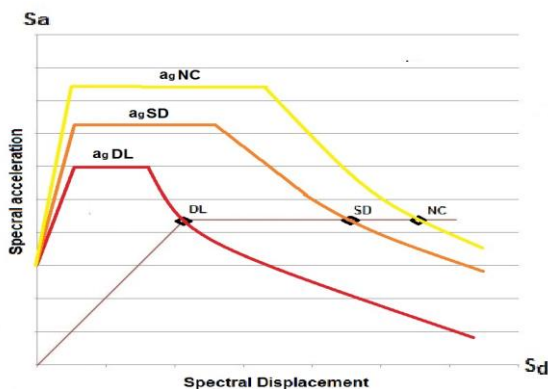


Fig 7. Schematized Calculation of “a_g” for different damage limit states levels (simplified figure)

In the present study, the seismic demand estimations for the seismic performance evaluation of the considered buildings are done considering the soil Type C with a moderate seismicity (0.20g) according to Eurocode 8 [23] and its corresponding spectra considering Soil category II and medium seismicity (0.22g) in KTP-N2-89 [16]. For both buildings, these limit states were calculated, and maximum “a_g” values were compared for each limit states. Pushover analysis data and criteria of suggested in EC 8 were used to determine the damage limit states of each building in both directions.

Table 3. Drift capacities and seismic spectral acceleration capacities of the template masonry buildings obtained from pushover analyses for the considered performance levels

Building	Direction	Global Drift (cm)			Seismic Spectral acceleration “a _g ” (m/s ²)		
		DL	SD	NC	DL	SD	NC
Clay Brick	x	0.82	2.26	3.01	1.382	2.235	2.818
	y	0.95	2.45	3.27	1.404	2.219	2.814
Silicate Brick	x	0.78	1.9	2.53	1.367	2.001	2.499
	y	1.04	3.18	4.24	1.267	2.281	2.908

The two structures made of clay brick and silicate brick in this study show different levels of seismic response. As can be seen from Table 3-4, building constructed by clay bricks has a superior seismic capacity than silicate one. The peak ground acceleration (a_g) that can be sustained for the NC state for the clay building is near 0.24g meanwhile for the silicate building is near 0.2g. Even though silicate bricks have higher compressive strength than

clay bricks, bonding between clay brick and mortar is stronger than silicate bricks and mortar.

Table 4. Performance levels their corresponding PGAs for the studied buildings

Building	0.14g	0.16g	0.18g	0.2g	0.22g	0.24g
Clay Brick	DL	SD				NC
Silicate Brick	SD				NC	

5.2 Discussion of the results

Building constructed with silicate bricks has better material characteristics including f_b , f_m and f_k however, the bonding connection is stronger in clay bricked specimens compared to silicate one. Due to the higher density of the silicate bricks, this building has 10% more weight (Table 5). Compared with each other, the silicate building has higher strength capacities in both directions whereas, the displacement capacity of the clay brick structure is better. Both buildings have higher displacement capacities in y - direction due to the distribution of the load bearing walls in this orientation.

Table 5. Comparative assesment of the clay and silicate brick masonry parameters obtained from experimental tests and pushover analyses

	Building Scenario - A (Clay Bricked)	Building Scenario - B (Silicate Bricked)
Brick compressive strength, (f_b)	7.5 MPa	10 MPa
Mortar compressive strength, (f_m)	4.8 MPa	5 MPa
Masonry compressive strength, (f_k)	2.42 MPa	2.97 MPa
Shear strength of masonry, (f_{vk})	0.36 MPa	0.4 MPa
Total weight, (W)	13202 kN	14175 kN
Max. Force (x - direction), (F_y^*)	2184.6 kN	2624 kN
Max. Displacement (x -direction), (d_m^*)	3.05 cm	2.53 cm
Max. Force (y -direction), (F_x^*)	1857 kN	1961 kN
Max. Displacement (y -direction), (d_m^*)	4.62 cm	4.24 cm
Displacement/Height (x -direction), (d_m^*/H)	0.22%	0.18%
Displacement/Height (y -direction), (d_m^*/H)	0.33%	0.30%

A comparison between the two buildings' failure mechanism from pushover analysis is shown below (Fig. 8). From the failure scheme of the two buildings in x - direction, can be noted that the perimeter walls fail in both buildings in the upper floors from bending failure.

The clay bricked building shows a more ductile behavior than the silicate one. Failure is reached when all the right part of the perimeter wall fails in bending and also the wall in the back part of upper levels, whereas in the silicate model, the failure mechanism is reached before. The perimeter wall was taken in consideration, since it has the failure mechanism of both buildings. From the progression of the damage mechanisms, it was observed that the silicate building reached its ultimate capacity when some parts of the same wall was undamaged. This shows a brittle failure mode compared with the clay brick building.

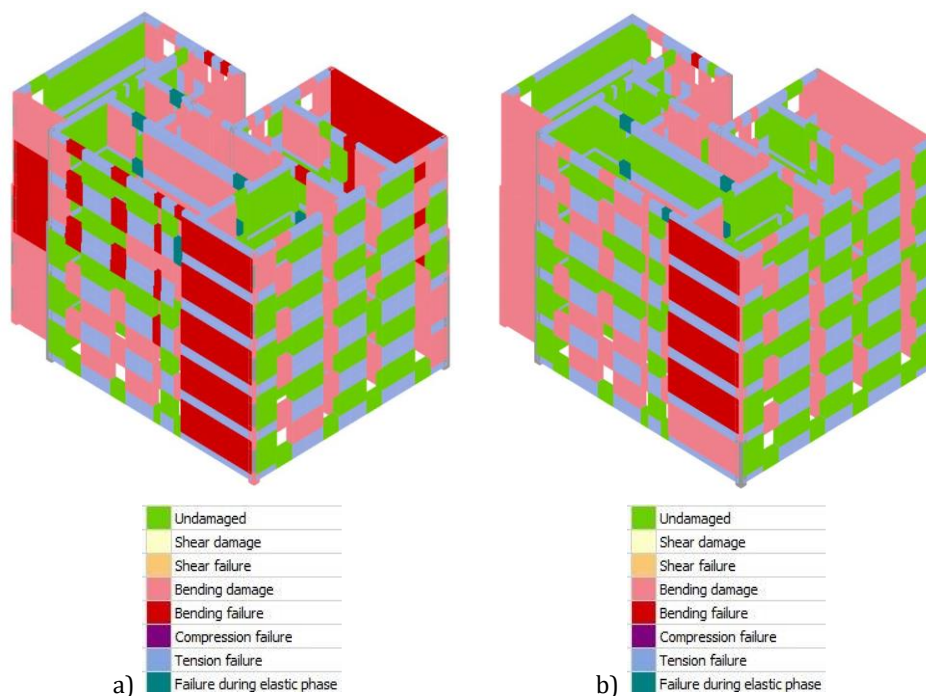


Fig 8. Comparison of the failure mechanism of both buildings; a) Clay brick; b) Silicate brick

6. Conclusion

This paper aims at presenting and discussing the results of an analytical study on two URM structures constructed by calcium silicate bricks and clay bricks. These types of materials are common in Balkans like in many European countries characterized by low-moderate seismic hazard. As a result of the recent earthquakes hit the region, the evaluation of the seismic vulnerability of masonry buildings including clay and calcium silicate bricks became necessary.

In this research, the influence of the material characteristics on a typical URM building response has been investigated. The models are investigated using non-linear static analyses. The seismic capacity of the building was evaluated by a structural model that uses macro elements for masonry panels. The results of these analyses, expressed in terms of shear distributions and displacements, are compared with each other. The seismic demand has been defined by the response spectra proposed by the EC 8 and the corresponding Albanian seismic codes of practice. The mechanical properties of the materials used are obtained from experimental tests. Based on the laboratory test results done on the clay and silicate clay bricks, analytical models of the URM structures were developed by TREMURI software.

Damage thresholds were determined according to EC 8. The performance points were obtained and comparatively assessed. According to the analysis results; capacity curves obtained by non-linear static analysis demonstrate that URM building constructed by the clay bricks performed better than the silicate bricked one. It does also show a greater ductile response. This could be expressed by the better bonding between the clay and mortars.

Based on the capacity evaluation; in contrast to the type of building constructed by clay masonry, calcium-silicate one showed a stiffer and slightly stronger response. Yet, at similar values of in-plane, lateral drift, they exhibited more damage based on the analytical simulations. This observation was also monitored during the recent earthquake which hit Albania on November 26, 2019. Since the material is stiffer, the increased damage was not unforeseen, but the building also displayed a more brittle response during this earthquake. This appears to suggest that buildings built of calcium-silicate brick are more vulnerable to damage. Such observations were observed on wall specimens tested in northern Europe, as well [24].

Acknowledgement

The authors acknowledge that this study is supported by the Albanian General Directorate of the Institute for Construction (<http://www.institutindertimit.al/>).

References

- [1] Bilgin, H., Huta, E. Earthquake performance assessment of low and mid-rise buildings: Emphasis on URM buildings in Albania. *Earthquakes and Structures*. 2018;14(6):599-614.
- [2] Bilgin, H., Korini, O. Seismic capacity evaluation of unreinforced masonry residential buildings in Albania. *Natural Hazards and Earth System Sciences* 2012,12(12): 3753-3764. <https://doi.org/10.5194/nhess-12-3753-2012>
- [3] Penna, A., Morandi, P., Rota, M. et al. Performance of masonry buildings during the Emilia 2012 earthquake. *Bull Earthquake Engineering*. 2014;(12):2255-2273. <https://doi.org/10.1007/s10518-013-9496-6>
- [4] Yilmaz, S., Tama, Y. S., & Bilgin, H. Seismic performance evaluation of unreinforced masonry school buildings in Turkey. *Journal of Vibration and Control*. 2013;19(16):2421-2433. <https://doi.org/10.1177/1077546312453190>
- [5] Ozmen HB, Inel M. Strength reduction factors for existing mid-rise RC buildings for different performance levels. *Res. Eng. Struct. Mat.* 2018; 4(4): 241-255. <https://doi.org/10.17515/resm2018.60ea3107>
- [6] Clementi, F., Gazzani, V., Poiani, M., Lenci, S. Assessment of seismic behaviour of heritage masonry buildings using numerical modelling. *Journal of Building Engineering*. 2016(8):29-47. <https://doi.org/10.1016/j.jobbe.2016.09.005>
- [7] Bilgin, H. and Hysenlliu, M. Comparison of near and far-fault ground motion effects on low and mid-rise masonry buildings. *Journal of Building Engineering*. 2020;(30):101248. <https://doi.org/10.1016/j.jobbe.2020.101248>
- [8] Isik, E. and Kutanis, M. Performance based assessment for existing residential buildings in Lake Van basin and seismicity of the region. *Earthq. Struct.*, 2015,9(4):893-91. <https://doi.org/10.12989/eas.2015.9.4.893>
- [9] Hadzima-Nyarko, M., Pavić, G., & Lešić, M. Seismic vulnerability of old confined masonry buildings in Osijek, Croatia. *Earthquakes and Structures*. 2016,11(4):629-648. <https://doi.org/10.12989/eas.2016.11.4.629>
- [10] Crowley, H., Pinho, R., van Elk, J. et al. Probabilistic damage assessment of buildings due to induced seismicity. *Bull Earthquake Eng.* 2019(17):4495-4516. <https://doi.org/10.1007/s10518-018-0462-1>
- [11] Ademovic, N., Hrasnica, M. and Oliveira, D.V. Pushover analysis and failure pattern of a typical masonry residential building in Bosnia and Herzegovina. *Eng. Struct.* 2013(50):13-29. <https://doi.org/10.1016/j.engstruct.2012.11.031>
- [12] Bilgin, H., & Frangu, I. Predicting the seismic performance of typical R/C healthcare facilities: emphasis on hospitals. *International Journal of Advanced Structural Engineering*. 2017,9(3):277-292. <https://doi.org/10.1007/s40091-017-0164-y>

- [13] Bilgin, H. Typological Classification of Churches Constructed During Post-Byzantine Period in Albania. *Gazi University Journal of Science Part B*. 2015,3(1):1-15.
- [14] Graziotti, F., Rossi, A., Mandirola, M., Penna, A., & Magenes, G. Experimental characterization of calcium-silicate brick masonry for seismic assessment: Proceedings of the 16th International Brick and Block Masonry Conference, Padova, Italy, 26-30 June 2016. <https://doi.org/10.1201/b21889-201>
- [15] KTP-9-78, Albanian masonry design code. (1978), (In Albanian).
- [16] KTP-N2-89, Albanian seismic design code. (1989), (In Albanian).
- [17] Lagomarsino, S., Penna A., Galasco A., Cattari, S. TREMURI program: an equivalent frame model for the nonlinear seismic analysis of masonry buildings. *Eng Struct*. 2013(56):1787-99. <https://doi.org/10.1016/j.engstruct.2013.08.002>
- [18] EN 772-1. European Standard: Methods of test for masonry units - Part 1: Determination of compressive strength, CEN, Brussels, 2000.
- [19] EN 1015-11. European Standard: Methods of test for mortar for masonry - Part 11: Determination of flexural and compressive strength of hardened mortar, CEN, Brussels, 1999.
- [20] EN 1052-1, -3, -5. European Standard: Methods of test for masonry, CEN, Brussels, 1998.
- [21] Lourenço, PB. Computations on historic masonry structures. *Progress in Structural Engineering and Materials*. 2002,4(3):301-319. <https://doi.org/10.1002/pse.120>
- [22] Gambarotta, L., & Lagomarsino, S. On dynamic response of masonry panels. Proceedings of the national conference on 'Masonry mechanics between theory and practice', Messina, Italy, 1996.
- [23] EN 1998-1. European seismic design code. (2004). "Design of structures for earthquake resistance. Part 1: General rules, seismic actions and rules for buildings".
- [24] Korswagen, P.A., Longo, M. & Rots, J.G. Calcium silicate against clay brick masonry: an experimental comparison of the in-plane behaviour during light damage. *Bull Earthquake Eng*. 2020(18): 2759-2781. <https://doi.org/10.1007/s10518-020-00803-5>



Research on Engineering Structures & Materials

In This Issue

Research Article

- 293 **Ahmet Meram, Betül Sözen**
Investigation on the manufacturing variants influential on the strength of 3D printed products

Research Article

- 315 **Halil Murat Enginsoy**
Investigation of recycled aluminum matrix composites reinforced with copper and γ -alumina manufactured by sinter and sinter + forging methods

Review Article

- 327 **Aykut Elmas, Güliz Akyüz, Ayhan Bergal, Müberra Andaç, Ömer Andaç**
Mathematical Modelling of Drug Release

Research Article

- 351 **M. Govindaraju, M. Selvaraj**
Boundary layer flow of gold -thorium water based nanofluids over a moving semi-infinite plat

Research Article

- 363 **Canan Kandilli, Mert Uzel**
Evaluation of annual performance of a photovoltaic thermal system integrated with natural zeolites

Research Article

- 375 **Büşranur Duman, Berker Fıçıcılar**
Acid modified graphite felt cathode electrode for low temperature H_2/Br_2 redox flow battery

Research Article

- 385 **Abdullah Fettahoglu, Mehmet Cemal Genes**
Design charts for linear elastic pavements

Research Article

- 411 **Elton Hala**
Wind performance for a stadium geometry

Research Article

- 425 **Marjo Hysenliu, Altin Bidaj, Huseyin Bilgin**
Influence of material properties on the seismic response of masonry buildings

C
O
N
T
E
N
T



Research on
Engineering
Structures & Materials

